

CHARGE CURRENT QUASI-ELASTIC
MUON NEUTRINO INTERACTIONS IN THE
BABY MIND DETECTOR

SVEN-PATRIK HALLSJÖ

SUBMITTED IN FULFILMENT OF THE REQUIREMENTS FOR THE DEGREE OF
Doctor of Philosophy

SCHOOL OF PHYSICS AND ASTRONOMY
COLLEGE OF SCIENCE AND ENGINEERING
UNIVERSITY OF GLASGOW



University | School of Physics
of Glasgow | & Astronomy

Abstract

This is a dissertation outline using the style guidelines defined by the University of Glasgow.

"We are just an advanced breed of monkeys on a minor planet of a very average star. But we can understand the Universe. That makes us something very special." – Stephen W. Hawking

Acknowledgements

It-guys, friends, family, etc...

Thank you IT-guys for handing the great ScotGRID bakeoff!

Formalia? Needed here?

The CERN Neutrino Platform provided extensive support for the design, construction and testing of the Baby MIND. We acknowledge the large contribution made by CERN through the Neutrino Platform to Baby MIND. This research provided within was fully funded through WP08 under AIDA2020.



This project has received funding from the European Union's Horizon 2020 research and innovation programme under grant agreement No 654168

Declaration

The research results presented in this thesis are the product of my own work. Appropriate references are provided when results of third parties are mentioned. The research presented here was not submitted for another degree in any other department or university.

Sven-Patrik Philip George Hallsjö

Table of Contents

1	Introduction to Neutrino Physics	1
1.1	Research Goals	1
1.2	Neutrino discovery	1
1.3	Standard Model neutrino	5
1.4	Neutrino interactions	9
1.4.1	Neutrino-electron interactions	9
1.4.2	Neutrino-quark scattering	11
1.4.2.1	Quasi-elastic interactions	11
1.4.2.2	Deep inelastic scattering	12
1.4.2.3	Resonant interactions	12
1.4.3	Comparing neutrino interactions to QED	12
1.5	Missing neutrinos	13
1.6	Neutrino mass and oscillation in vacuum	15
1.7	CP-violation, baryogenesis and leptogenesis	18
1.7.1	Current theory of leptogenesis	18
1.8	Introduction to explaining neutrino masses	20
1.8.1	Dirac neutrinos	20
1.8.2	Majorana neutrinos	21
1.9	Summary	21
2	Neutrino experiments	22
2.1	Introduction	22
2.2	Atmospheric	23

2.2.1	Historical experiments	24
2.2.2	NUSEX	24
2.2.3	KamiokaNDE	24
2.2.4	IMB	26
2.2.5	Super-Kamiokande	26
2.2.6	MACRO	26
2.3	Solar	28
2.3.1	Super-Kamiokande	28
2.3.2	SNO	28
2.3.3	Borexino	30
2.4	Accelerator	31
2.4.1	Historical experiments	31
2.4.2	NOMAD	32
2.4.3	K2K	33
2.4.4	MINOS	33
2.4.5	T2K	34
2.5	Reactor	36
2.5.1	KamLAND	37
2.5.2	Double Chooz	38
2.5.3	RENO	38
2.5.4	Daya Bay	40
2.5.5	JUNO	41
2.6	Future neutrino oscillation experiments	42
2.6.1	DUNE	42
2.6.2	Hyper-K	42
2.7	Neutrino Factory	43
2.7.1	NuSTORM	44
2.8	Magnetized Iron Neutrino Detectors	46
2.9	Summary	46

3 Baby MIND + WAGASCI	47
3.1 Baby MIND/NP05	47
3.1.1 Motivation	47
3.1.2 Magnet modules	48
3.1.3 Scintillator modules	49
3.1.4 Layout	49
3.1.5 Electronics	51
3.1.6 Construction and test beam	54
3.2 WAGASCI/T59	55
3.2.1 Motivation	55
3.2.2 Layout	56
3.2.3 Electronics	57
3.2.4 MRD and Baby MIND	61
3.3 Summary	61
4 SaRoMaN	62
4.1 Introduction	62
4.2 General structure	62
4.3 Wrapper	63
4.4 Simulation	64
4.5 Digitisation	66
4.5.1 Simulated data	67
4.5.2 DAQ	67
4.6 Reconstruction	69
4.6.1 Structure	69
4.6.2 Pattern recognition	70
4.6.3 Fitting	71
4.6.4 Low momentum algorithms	72
4.6.5 Performance	75
4.6.6 DAQ/Unpacking	76
4.6.7 Particle identification	77

4.7	Future development	78
4.7.1	Containers	79
4.7.1.1	Container vs Virtual machine	79
4.7.1.2	Container for particle physics simulations	79
4.7.2	Machine learning in particle physics	80
4.7.3	Other good practises	80
4.7.3.1	Versioning	80
4.7.3.2	Continuous integration	80
4.7.3.3	Documenting	80
4.8	Summary	80
5	Test beam	81
5.1	TASD-test beam	81
5.1.1	Setup	81
5.1.2	DAQ	83
5.1.3	Data preprocessing	83
5.1.4	Results	84
5.2	MIND-test beam	85
5.2.1	Setup	85
5.2.2	Data preprocessing	86
5.2.3	Analysis	87
5.2.4	Results	87
5.2.4.1	Electronics results	88
5.2.4.2	Magnet results	88
5.2.4.3	Hits in SaRoMaN	89
5.2.4.4	Tracks in SaRoMaN	89
5.2.4.5	Charge identification efficiency	90
5.2.4.6	Particle identification	94
5.2.4.7	Updated charge identification efficiency	98
5.3	Summary	98

6 Neutrino interaction studies	100
6.1 Muon charge current quasi-elastic	100
6.1.1 Interactions in TASD + Baby MIND (NuSTORM)	102
6.1.2 Neutrino interactions in Iron in Baby MIND	108
6.1.2.1 Simulations vs data	110
6.2 Future studies	112
6.2.1 Neutrino interactions in WAGASCI + Baby MIND	112
6.2.1.1 Interactions in the full WAGASCI	112
6.3 Summary	112
7 Conclusions and Outlook	113
7.1 Baby MIND	113
7.2 WAGASCI	113
7.3 Software	113
7.4 Machine learning in physics	113
7.5 Neutrino physics	113
Bibliography	114

List of Tables

1.1	Neutrino interactions with electrons	10
1.2	Current upper neutrino mass limits [12]	17

List of Figures

1.1	The kinetic energy spectrum of the emitted electron from beta decay from a Radium-E source [3]. If no anti-neutrino were emitted a single electron volt(s) value would be expected.	2
1.2	Feynman diagrams showing beta decay.	2
1.3	The standard model of particle physics where the three first columns represent the so called generations, starting with the first. [15]	9
1.4	Charge interaction between neutrinos and electrons	10
1.5	Neutral interaction between neutrinos and electrons	11
1.6	Neutrino pair production	11
1.7	The QED and the weak contributions to the scattering electron-positron to any quark or lepton pair. ¹	13
1.8	Feynman diagrams, CC(Left) and NC(Right) with the same initial states. . .	13
2.1	A sketch of the NUSEX detector with various parts highlighted [38]. . . .	24
2.2	Data compared to Monte Carlo for 50 neutrino events in the NUSEX and showing consistency within errors [39].	25
2.3	Schematic image of the KamiokaNDE detector. [40].	25
2.4	A sample event showing Cherenkov rings produced by a muon event [40]. .	25
2.5	Comparing ring multiplicity distributions between data and simulations [41].	26
2.6	Comparison of the ration of data vs Monte Carlo vs length over neutrino energy for fully contained atmospheric electron-like and muon-like events [23].	27
2.7	Left) A schematic of the Super-K detector., Right) Event recorded in Super-K.	27
2.8	Schematic of the MACRO [45].	28
2.9	Left) A schematic drawing of the SNO detector [21], Right) Cherenkov light recorded from a muon created by interaction of an atmospheric neutrino in the heavy water.	29

2.10	The flux of solar neutrinos of μ or τ flavour vs flux of electron neutrinos measured in SNO from the three reactions, CC in red, ES in purple and NC in blue. The diagonal dashed lines show the prediction from the Standard Solar Model. The coloured bands intersect at the fit values for all fluxes indicating that they are consisted with neutrino flavour transformation with no distortion in the solar neutrino energy spectrum. [21].	29
2.11	(Left) Schematic of the Borexino experiment [48]. (Right) Electron neutrino survival probability as a function of neutrino energy according representing different neutrino solar production channels both from the Solar standard model and measurements from the Borexino experiment [48].	30
2.12	A sideview of the NOMAD detector [53].	32
2.13	A schematic view of the K2K experiment Super-K [55].	33
2.14	Simulated unoscillated expected neutrino fluxes for various flavours with expected systematic before applying near detector data plotted as bands. at Super-K [61].	35
2.15	A schematic view of the T2K experiment, including the near detector site ND280 and Super-K.	35
2.16	Posterior probability density on δ_{CP} , where the cross represent the best-fit [62].	36
2.17	The 90% and 68% confidence levels in the $\sin^2 \theta_{23}, \Delta m_{32}^2$ space from T2K compared to other experiments, assuming normal ordering of neutrino masses [62].	36
2.18	Energy spectrum of $\bar{\nu}_e$, the inverse beta decay cross section and interaction spectrum of detected inverse beta decay events [64].	37
2.19	Schematic diagram of the KamLAND detector [65].	38
2.20	Top panel: Expected reactor $\bar{\nu}_e$ energy spectrum. Lower panel: Energy spectrum of the observed events along with the no oscillation spectrum and best fit spectrum.	38
2.21	Overview of the Double Chooz experimental site [66].	39
2.22	Top panel: Measured energy spectrum with data on best fit and no oscillation models. Lower panel: Ratio of data over no-oscillation prediction [68]. . . .	39
2.23	Layout of the RENO detectors, yellow and reactors in red. The six reactors are equally spaced in a 1280 m span [69].	39
2.24	Top panel: Measured energy spectrum with data on best fit and no oscillation models. Lower panel: Ratio of data over no-oscillation prediction [69]. . . .	39
2.25	Layout of the Daya Bay experiment [70].	40

2.26	Near site layout of the Daya Bay detector with surrounding structure [71].	40
2.27	Comparison of $\sin^2 2\theta_{13}$ measurements from various experiments, taken from [71].	40
2.28	Comparison of $ \Delta m_{32}^2 $ measurements from various experiments, taken from [71].	40
2.29	Location of the JUNO site with distances to the near by reactors, Yangjiang and Taishan at both 53km as well as Daya Bay at 215km away. [72].	41
2.30	Schematic view of the JUNO detector [72].	41
2.31	Estimated significance of the mass hierarchy discrimination metric as a function of values for δ_{CP} [73].	42
2.32	Schematic view of the DUNE detectors [73].	42
2.33	Cross section view of the Hyper-Kamiokande detector [75].	43
2.34	A map showing the proposed candidate site [75].	43
2.35	Schematic diagram of the Neutrino Factory [76].	44
2.36	Expected precision for a measurement of the δ_{cp} at a Neutrino Factory compared to alternate neutrino oscillation facilities [76].	45
2.37	A schematic of a NuSTORM facility [76].	45
3.1	(Top) Schematic view of the magnet module. (Bottom) A contour plot of the magnet module, with the fiducial areas of interest showing magnetic field uniformity.	50
3.2	Schematic view of the horizontal bar and light yield curves.	51
3.3	Schematic view of the vertical bar and light yield curves performed for hits at the near and far end of the bar.	52
3.4	The test beam Baby MIND design, in yellow the magnet modules and in blue the scintillator modules.	52
3.5	(Left) Schematic view of FEB layout. (Right) An image of the FEB in one of the racks.	53
3.6	(Left) Front end electronics mini-crate installed on the detector. (Right) Block diagram representing the backplane. Figures from [90]	53
3.7	Readout block for the Baby MIND. Figure from [90]	54
3.8	The basic structure of the WAGASCI detector including one of the possible designs for the MIND plates. The MIND detector is denoted as Downstream MRD [91].	56
3.9	The structure of the WAGASCI detector with scintillator bars either horizontally or vertically with a structure to support each the boxes.	57

3.10	An illustration of the full WAGASCI module	58
3.11	An illustration of the INGRID proton module.	59
3.12	An illustration of the INGRID module.	59
3.13	An photo of the fully installed WAGASCI module with the INGRID and INGRID proton modules at the B2 floor at J-PARC.	60
3.14	An image showing the B2 environment with (From left) INGRID proton module, WAGASCI, INGRID module and Baby MIND. The side MRDs are in gray.	61
3.15	B2 environment seen slightly from the side.	61
4.1	Code flow of the SaRoMaN software suite all controlled and handled through a wrapper.	63
4.2	Code structure of the SaRoMaN software suite all controlled and handled through a wrapper.	64
4.3	Example of how to run a default simulation.	64
4.4	Program flow for the digitisation.	66
4.5	Illustration of the difficulty in combining hits in vertical and horizontal bars.	67
4.6	Figure of one bending in first plane in mind.	73
4.7	Illustration of the angular distributions and criteria for selecting charge. . .	74
4.8	(Left) Image of the initial Baby MIND layout. (Right) The current Baby MIND layout. The main differences consists of removing the first scintilla- tor plane, some different layout in the middle blocks and removed the final scintillator plane.	75
4.9	Metric plots of the initial Baby MIND layout with all algorithms adjusted to utilize this layout.	76
4.10	Metric plots of the CERN test beam Baby MIND layout.	76
4.11	TDM, GTRIG, SPILL and DATA structure for the FEB readout communica- tion.	77
5.1	The TASD with the instrumented bars visualised	82
5.2	The TASD at the PS with the readout PC.	83
5.3	(Left) An XY-beam profile as measured by the TASD. (Right) An YZ-beam profile as measured by the TASD	84

5.4	(Left) 3D-Beam profile measured by the TASD. (Right) Single muon track passing through the detector.	84
5.5	MIND in testbeam.	85
5.6	MIND in testbeam photo.	86
5.7	Gain for 576 channels (left) and noise spectrum finger plots with 5 viable peaks. for one channel (right).	88
5.8	Baby MIND magnet measured (at CERN) field values for 33 modules (left), current at J-PARC (middle) and corresponding voltage (right).	88
5.9	All recorded hits for a run with the 5 GeV beam settings.	89
5.10	A sample track, taking a time cut for the hits for a run with the 5 GeV beam settings.	90
5.11	Sample events of test beam interactions at a set energy value of $5GeV/c$	91
5.12	Initial charge id results	92
5.13	Simulated charge id for different particles vs data points	93
5.14	Input variables for both signal and background using simulated data	94
5.15	ROC curve for various machine learning algorithms.	95
5.16	ROC curve for the chosen machine learning algorithms.	96
5.17	Response with and without over-training check	96
5.18	Cut efficiency plots.	97
5.19	After TMVA charge id results	99
6.1	Neutrino cross sections, showing the quasi-elastic, deep inelastic and single pion cross sections in the GeV range. Taken from [105] modified from original made by G.P. Zeller [12] containing data points from various experiments.	101
6.2	Energy spectrum of muon and anti-electron neutrinos produced at NuSTORM and recorded at 50 m from the storage ring.	102
6.3	An illustrative sketch of the detector setup with the TASD detector in front of Baby MIND.	103
6.4	Input variables for both signal and background using simulated data	104
6.5	ROC curve for various machine learning algorithms.	104
6.6	Response with and without over-training check	105
6.7	Cut efficiency plots.	105

6.8	The energy spectrum for muon neutrinos and muon anti-neutrinos in the T2K near detector RHC beam.	106
6.9	The efficiency plot of how well the algorithm can reconstruct neutrino tracks vs muon momenta for simulated tracks interacting in the TASD.	106
6.10	The efficiency plot of how well the algorithm can reconstruct muon charge vs muon momenta for tracks fitted in the algorithm.	107
6.11	The efficiency plot of how well the algorithm can reconstruct muon charge vs muon momenta for simulated tracks. Combination of the previous two figures.	107
6.12	The efficiency plot of how well the algorithm can reconstruct muon charge vs muon momenta for simulated tracks zoombed in at the low momentum range.	108
6.13	The layout of the MIND for the commissioning neutrino run.	109
6.14	Details of the fiducial volume for the neutrino events to compare simulations with data.	109
6.15	The efficiency plot of how well the algorithm can reconstruct neutrino tracks vs muon momenta for simulated tracks interacting in the Iron.	110
6.16	The efficiency plot of how well the algorithm can reconstruct muon charge vs muon momenta for tracks fitted in the algorithm.	110
6.17	Energy spectrum of the reconstructed events with simulation in contour and data as error bars for $\bar{\nu}_\mu$ events.	111
6.18	Energy spectrum of the reconstructed events with simulation in contour and data as error bars for ν_μ events.	111

Chapter 1

Introduction to Neutrino Physics

1.1 Research Goals

The research in this thesis describes the construction of a prototype Magnetized Iron Neutrino Detector (Baby MIND) at the European Organization for Nuclear Research (CERN) and determine the performance of the detector to reconstruct charged particle tracks at a test beam at CERN and neutrino interactions with our collaborators in the WAGASCI collaboration at a neutrino beam line at the Japan Proton Accelerator Research Complex (J-PARC).

1.2 Neutrino discovery

While measuring radioactive beta decay, from bombarding beryllium with alpha particles from polonium in the first two decades of the 20th century, physicists discovered what was then an anomaly. At the time it was thought that beta decay occurred as a two body process in which a neutron (n) decays to a proton (p) and electron (e^-). If this were the case, the energy of the proton and electron should be discrete and add up to the energy of the neutron. However experiments showed that the electron had a continuous spectrum of energy values, violating the energy conservation law, as seen in figure 1.1. In order to solve this anomaly, a third particle, the neutrino (ν), was postulated by Wolfgang Pauli [1] and then incorporated into the beta decay by Enrico Fermi [2]. The neutrino was postulated as a neutral particle with mass of less than 1% of the proton mass and a spin of 1/2. For consistency, the particle produced in the beta decay is relabelled as the electron antineutrino, $\bar{\nu}_e$, in order to conserve lepton number. The addition of another particle changed the decay to $n \rightarrow p + e^- + \bar{\nu}_e$ and introduced the weak interaction model, as seen in figure 1.2.

It would take another twenty years until the neutrino was experimentally discovered by the Savannah river reactor experiment in 1956 [4] where neutrinos from a nuclear reactor were

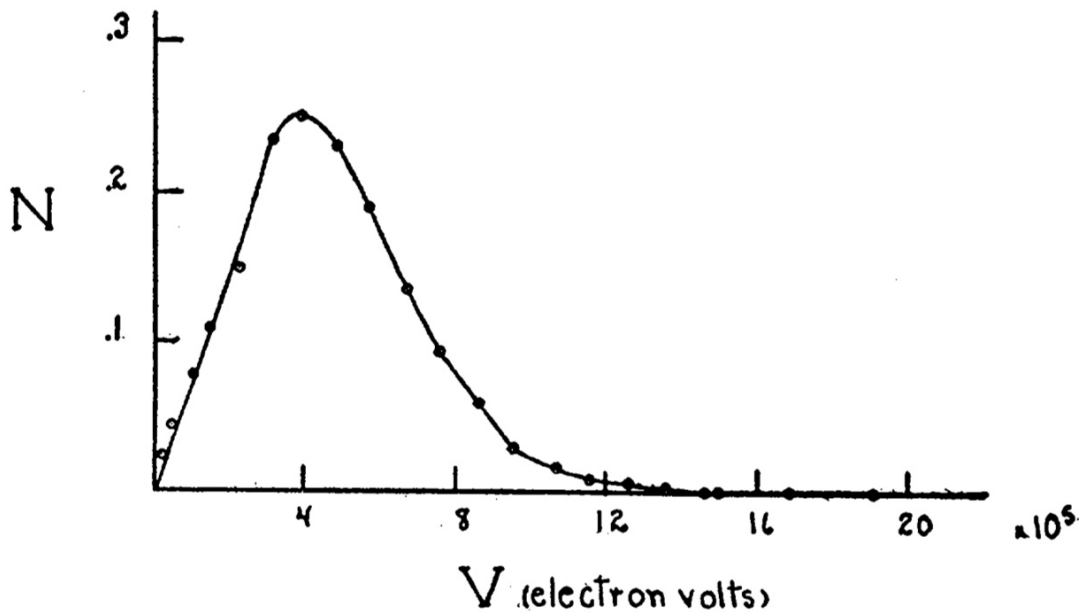


Figure 1.1: The kinetic energy spectrum of the emitted electron from beta decay from a Radium-E source [3]. If no anti-neutrino were emitted a single electron volt(s) value would be expected.

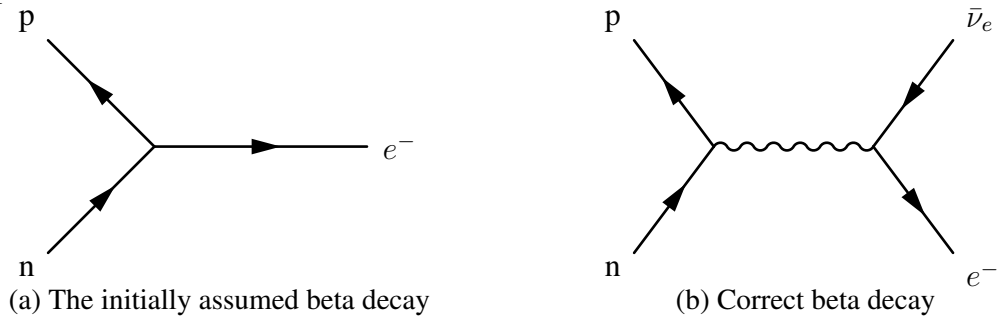


Figure 1.2: Feynman diagrams showing beta decay.

detected in 300 litres of liquid scintillator and cadmium. The experiment was awarded the Nobel prize in 1995.

After the discovery of the electron neutrino (ν_e), several neutrino experiments were performed and led to the discovery of two other neutrino types/flavours, the muon neutrino (ν_μ) and the tau neutrino (ν_τ) [5, 6, 7].

To describe the neutrino interactions it is worth building a theory to try to describe the interactions. Starting with the generalized and relativistic version of the Schrödinger equation, the Dirac equation:

$$\sum_{\mu} (i\gamma^{\mu} \partial_{\mu} - m) \psi(x) = 0 \quad (1.1)$$

where γ are the so called Dirac matrices and the sum over μ is often removed using the Einstein notation requiring any free index to be summed over.

As with all quantum mechanical equations this allows us to define $\psi(x)$ as a quantum field or state.

After taking Lorentz-invariance into account the Dirac Lagrangian of can be written as:

$$\mathcal{L} = \bar{\psi}(i\gamma^\mu \partial_\mu - m)\psi \quad (1.2)$$

where the Euler-Lagrange equation for $\bar{\psi}$ reproduces the Dirac equation.

The Lagrangian is so far correct, however from a physical point of view the equation also needs to be invariant under a phase shift, so called gauge transformation $\psi \rightarrow e^{i\theta(x)}\psi$. This requires the addition of an extra term to remove the terms which prevent gauge invariance providing the full Dirac Lagrangian as:

$$\mathcal{L} = \bar{\psi}(i\gamma^\mu \partial_\mu - m)\psi - q\bar{\psi}\gamma^\mu\psi\epsilon_\mu \equiv \mathcal{L}_{Dirac} \quad (1.3)$$

with ϵ_μ being a new field which must be gauge invariant and q a conserved quantity, a numerical constant.

There is now a mathematical framework to describe quantum states or particles in a vacuum. It is now possible to create a framework for a particle interacting with a electromagnetic field by combining \mathcal{L}_{Dirac} with the classical $\mathcal{L}_{Maxwell} = -\frac{1}{4}F_{\mu\nu}F^{\mu\nu}$ with $F^{\mu\nu} = \partial^\mu A^\nu - \partial^\nu A^\mu$ where A_μ is the electromagnetic vector potential, a 4-vector combined of the electric potential and magnetic potential.

This produces the following Lagrangian:

$$\mathcal{L} = \mathcal{L}_{Dirac} + \mathcal{L}_{Maxwell} = \bar{\psi}(i\gamma^\mu \partial_\mu - m)\psi - q\bar{\psi}\gamma^\mu\psi\epsilon_\mu - \frac{1}{4}F_{\mu\nu}F^{\mu\nu} \quad (1.4)$$

There is nothing preventing us from choosing our previous field ϵ as the electromagnetic vector potential A and choosing q as the electron charge e to produce the experimentally verified Lagrangian for quantum and electromagnetic interactions or Quantum ElectroDynamics (QED):

$$\mathcal{L}_{QED} \equiv \bar{\psi}(i\gamma^\mu \partial_\mu - m)\psi - e\bar{\psi}\gamma^\mu\psi A_\mu - \frac{1}{4}F_{\mu\nu}F^{\mu\nu} \quad (1.5)$$

This can be simplified by introducing the gauge covariant derivative $D_\mu \equiv \partial_\mu + ieA_\mu$ and the slash notation as $\not{D} = \gamma^\mu D_\mu$. This produces the simplified QED Lagrangian as:

$$\mathcal{L}_{QED} = \bar{\psi}(i\gamma^\mu \not{D}_\mu - m)\psi - \frac{1}{4}F_{\mu\nu}F^{\mu\nu} \quad (1.6)$$

Based on the experiments relating to β -decay, Fermi hypothesised that the Lagrangian for

weak interactions should be similar to the QED Lagrangian. To handle the observed differences, a constant is added G_F to replace the electron charge, and mass removed. In this the assumption was made that the neutrinos were massless. QED contains γ^μ meaning that it transforms as a vector which was confirmed by experiments. For weak interactions anything could be mathematically possible. The absence of Fierz interference terms, parity violation and the Goldhaber helicity experiment made it clear that the interactions had to transform as vectors and axial vectors giving the term $\gamma^\mu - \gamma^\mu \gamma^5 = \gamma^\mu(1 - \gamma^5)$ and also providing the theory with its name: V-A theory.

This produced a Lagrangian in the form of

$$\mathcal{L} = \frac{G_F}{\sqrt{2}} J_L \cdot J_H \quad (1.7)$$

with J_L as the current describing interactions with leptons and J_H describing interactions with hadrons (up and down quarks instead of protons and neutrinos). The Fermi constant G_F was also added to substitute the electron charge. The currents were initially of the form:

$$J_L = \bar{\psi}_e(x) \gamma^\mu (1 - \gamma_5) \psi_\nu(x) \quad (1.8)$$

containing only the electron, and then expanded by adding more terms containing future particles. For the hadrons it could either be written for quarks as:

$$J_H = \bar{\psi}_u(x) \gamma^\mu (1 - \gamma_5) \psi_d(x) \quad (1.9)$$

or for protons and neutrons as:

$$J_H = \bar{\psi}_p(x) \gamma^\mu (g_\nu - g_A \gamma_5) \psi_n(x) \quad (1.10)$$

where g_ν and g_A are constants relating to strong interactions and have to be determined experimentally along with G_F .

1.3 Standard Model neutrino

V-A theory works well in practice but does not create a Gauge theory connecting to an underlying field, such as QED does. It is also based on the interacting particles not having mass which does not explain the observed masses of the weak interaction particles, W bosons. There is also no explanation for any neutral interactions which were observed and introduced a massive Z boson. Group theory describes that any unitary group U(N) has $N^2 - 1$ generators. This is also the case for groups with the determinant 1 denoted special S. Based on the SU(1) group from QED, the easiest group to handle the other bosons becomes SU(2).

Glashow-Weinberg-Salam (GWS) took the success of the V-A theory and modified it to make a Gauge theory out of it, Quantum Flavour Dynamics (QFD) with massive W:s and Z basing it on the SU(2) group. It was also easy to see that QFD and QED could be unified as an SU(2) group can be made invariant under U(1) by adding extra term. By choosing this constant term correctly QFD and QED were unified into the Electro-weak theory.

The experiment by Goldhaber, Grodzins, and Sunyar concluded that neutrinos only exist in a left handed chiral state, meaning that momentum and spin are oppositely aligned [8]. They also concluded that anti-neutrinos only exist in the right handed state. In the initial or unexpanded SM, [9], only fermions which have both chiral states have mass through the Brout-Englert-Higgs mechanism [10]. At the time this led to the definition of the neutrino as a massless particle, however in subsection 1.6 it will be shown that neutrino oscillations require at least one of the neutrinos to have mass. This indicates that the SM needs to be extended to account for this new physics.

The work by GWS will now be briefly detailed. Since experiments require 3 bosons and interaction modes, one can start with a simple field and make it SU(2). Initially the Lagrangian can naively be taken as that of a complex scalar field coupled to the electromagnetic field (and itself) as:

$$\mathcal{L} = -\frac{1}{4}F_{\mu\nu}F^{\mu\nu} + |D_\mu\phi|^2 - V(\phi) \quad (1.11)$$

where D_μ is the covariant derivative from QED, $D_\mu = \partial_\mu + ieA_\mu$ and a potential V will be discussed shortly as a way of adding mass to the theory.

Following the procedure done to produce QED and requiring gauge invariance requires the covariant derivative to be changed, requiring a field for each of the so called generators or each of the Bosons. This requires 3 new fields aside from the QED/photon field. This changes the covariant derivative in the following way.

$$D_\mu = \partial_\mu - igS_\mu^a \frac{\sigma^a}{2} - \frac{1}{2}g'A_\mu \quad (1.12)$$

where g' is now the new coupling to the photon field and g is the coupling to our new fields

S, a takes the values 1, 2, 3 and σ are the Pauli matrices.

At this stage there are enough fields to produce the Bosons required, however there needs to be a way of making all but the photon field massive.

V is chosen in a way such that it produces a massive Goldstone Boson [11] and so that it is also gauge invariant. This gives V as:

$$V(\phi) = -\mu^2 \phi^* \phi + \frac{\lambda}{2} (\phi^* \phi)^2 \quad (1.13)$$

where μ is a parameter. If $\mu^2 < 0$ it will produce a massive Boson, this is also a way of producing a massive photon in QED, however if $\mu^2 > 0$ then we produce a spontaneously symmetry breaking and ϕ can be split into a real and complex part where the real part will have mass but the complex will not. Essentially this breaks down the $SU(2) \times U(1)$ to a $U(1)$ theory. Therefore it produces 1 massless vector boson (the photon field A) and three massive vectors bosons fields (the S fields) and one physical Higgs scalar v .

The potential can be chosen, within the symmetry breaking as the Higgs potential [10]:

$$\langle \phi \rangle = \frac{1}{\sqrt{2}} \begin{pmatrix} 0 \\ v \end{pmatrix} \quad (1.14)$$

The mass related to each of these fields arrives from the $|D_\mu \phi|^2$ term in the Lagrangian. This can be explicitly seen, using the Higgs potential and $\phi^* |D_\mu \phi|^2 \phi$. Using the fact that the potential is a constant and cancelling signs produces:

$$\begin{pmatrix} 0 & v \end{pmatrix} \left(g S_\mu^a \frac{\sigma^a}{2} + \frac{1}{2} g' A_\mu \right) \left(g S^{b\mu} \frac{\sigma^b}{2} + \frac{1}{2} g' A^\mu \right) \begin{pmatrix} 0 \\ v \end{pmatrix} \quad (1.15)$$

Using the properties of Pauli matrices this can be rewritten as:

$$\frac{1}{2} \frac{v^2}{4} \{ g^2 (S_\mu^1)^2 + g^2 (S_\mu^2)^2 + (-g S_\mu^3 + g' A_\mu)^2 \} \quad (1.16)$$

These results can be modified to show how mass is added to fermions as well.

Using this note how the factors g and g' will produce different mass terms. To create a massless contribution combinations of these fields can be used to produce 4 different fields

required for the bosons with 3 massive and one massless as follows:

$$W^\pm = \frac{1}{\sqrt{2}}(S_\mu^1 \mp S_\mu^2) \quad (1.17)$$

$$Z_\mu = \frac{1}{\sqrt{g^2 + g'^2}}(gS_\mu^3 - g'A_\mu) \quad (1.18)$$

$$\gamma_\mu = \frac{1}{\sqrt{g^2 + g'^2}}(g'S_\mu^3 + gA_\mu) \quad (1.19)$$

with different masses, $m_W = g\frac{v}{2}$, $m_Z = \sqrt{g^2 + g'^2}\frac{v}{2}$ and $m_\gamma = 0$. By defining a weak mixing angle, the Weinberg angle a relationship between these fields can be defined as:

$$\begin{pmatrix} Z \\ \gamma \end{pmatrix} = \begin{pmatrix} \cos(\theta_W) & -\sin(\theta_W) \\ \sin(\theta_W) & \cos(\theta_W) \end{pmatrix} \begin{pmatrix} S^3 \\ A \end{pmatrix} \quad (1.20)$$

where $\cos(\theta_W) = \frac{g}{\sqrt{g^2 + g'^2}}$ and $\sin(\theta_W) = \frac{g'}{\sqrt{g^2 + g'^2}}$. This also provides a relationship using the above masses for W and Z as $m_W = m_Z \cos(\theta_W)$. To also ensure that QED is properly included in this theory the terms in front of the γ -field must be equal to the electron charge providing the following relationship: $e = g \sin(\theta_W) = g' \cos(\theta_W)$

This allows the final interaction Lagrangian to be written as:

$$\begin{aligned} \mathcal{L}_{int} = & i \frac{g}{\sqrt{2}} [j_\mu^{(+)} W^{\mu-} + j_\mu^{(-)} W^{\mu+}] \\ & + i[g \cos \theta_W j_\mu^{(3)} - g' \sin \theta_W j_\mu^{(Y/2)}] Z^\mu \\ & + i[g \sin \theta_W j_\mu^{(3)} + g' \cos \theta_W j_\mu^{(Y/2)}] \gamma^\mu \end{aligned} \quad (1.21)$$

or simplified as

$$\begin{aligned} \mathcal{L}_{int} = & i \frac{g}{\sqrt{2}} [j_\mu^{(+)} W^{\mu-} + j_\mu^{(-)} W^{\mu+}] \\ & + i[g \cos \theta_W j_\mu^{(3)} - g' \sin \theta_W j_\mu^{(Y/2)}] Z^\mu \\ & + ie[j_\mu^{(3)} + j_\mu^{(Y/2)}] \gamma^\mu \end{aligned} \quad (1.22)$$

where j are the different currents for each of the interactions. As an example, for the interaction between an electron and a neutrino, an interaction without any electromagnetic

interaction, the currents are written as:

$$j_\mu^{(W+)} = \frac{1}{2} \bar{\nu}_e \gamma_\mu (1 - \gamma_5) e \quad (1.23)$$

$$j_\mu^{(W-)} = \frac{1}{2} \bar{e} \gamma_\mu (1 - \gamma_5) \nu_e \quad (1.24)$$

$$j_\mu^{(Z)} = \frac{1}{2} \bar{\nu}_e \gamma_\mu (1 - \gamma_5) \nu_e - \frac{1}{2} \bar{e} \gamma_\mu (1 - \gamma_5) e + 2 \sin^2 \theta_W \bar{e} \gamma_\mu e \quad (1.25)$$

$$j_\mu^{(3)} = 0 \quad (1.26)$$

$$j_\mu^{(Y/2)} = 0 \quad (1.27)$$

Comparing the formula for $j_\mu^{(Z)}$ from the electroweak theory above, and from V-A theory, $j_\mu^{(Z)} = \frac{1}{2} \bar{\nu}_e \gamma_\mu (1 - \gamma_5) \nu_e + \bar{e} \gamma_\mu (g_\nu - g_A \gamma_5) e$, provides a relation between the g_ν and g_A and the Weinberg angles as $g_\nu = -\frac{1}{2} + 2 \sin^2 \theta_W$ and $g_A = -\frac{1}{2}$. Given that both the currents for both W and Z are non-zero means that electrons and neutrinos should have interaction through all three bosons. Looking in detail it can be seen that both of the W currents couple (anti-)neutrino to electron or vice-versa but the Z current only couples the particles to themselves. This means that the W currents carry charge and thus are named charge-current interactions compared to the Z current where this is not the case and have been named neutral-current interaction.

Finally to produce the full standard model requires the strong interaction QCD which will not be described in this thesis, and details can be found in [12] among others.

The Standard Model of particle physics (SM) categorizes all the fundamental particles that have been discovered experimentally and the mathematics of their properties and how they interact [13, 14].

The particles in SM, seen in figure 1.3, can be split into two different types, fermions and gauge bosons, characterised by their half-integer and integer spin. Fermions can be further split depending on their charge, quarks with fractional charge and leptons with integer charge. Gauge bosons are the force mediators for the particle interactions containing the Higgs boson, the only scalar, spin 0, particle in the SM [10].

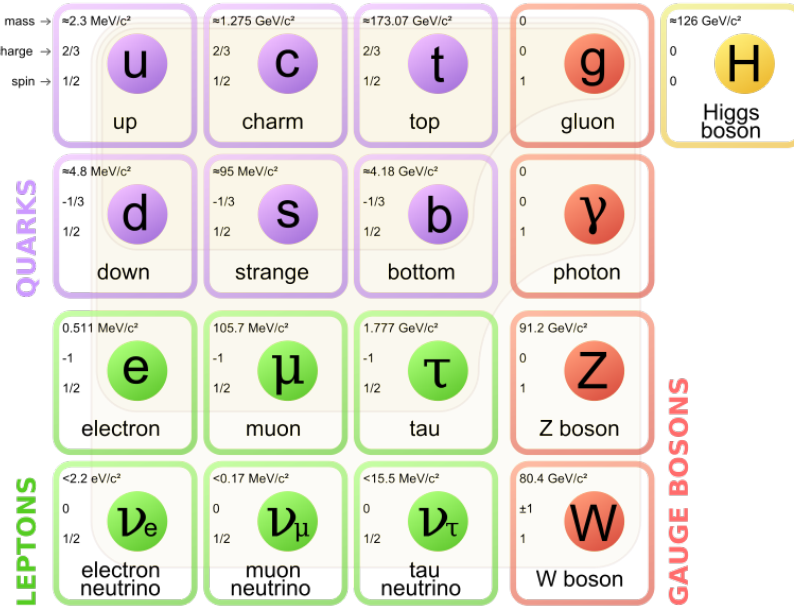


Figure 1.3: The standard model of particle physics where the three first columns represent the so called generations, starting with the first. [15]

1.4 Neutrino interactions

The described theory can be used to describe how neutrinos interact and with what.

Neutrino interactions are split into two different types depending on which boson mediates the interaction. Charge Current (CC) interactions change the final state quarks or leptons by one unit of electric charge and are mediated by the W^+ and W^- bosons while Neutral Current (NC) interactions do not change the charge and are mediated by a Z^0 boson. To look at possible interactions of neutrinos described in the Standard Model of particle physics, one needs to look at the quantum field theory description of the interactions[16, 17]. The further subsections have been split depending on what interaction particle is involved.

1.4.1 Neutrino-electron interactions

Through the theory it is clear that neutrinos should interact with electrons. Electrons are a fundamental particle meaning that the interaction can be seen as pointlike interactions.

When it comes to neutrino and electron interactions, experimentally only the following have been observed:

Lagrangian for NC scattering, $\nu_x y \rightarrow \nu_x y$:

$$\mathcal{L} = -\frac{G_F}{\sqrt{2}} [\bar{\nu}_x \gamma_\alpha (1 - \gamma_5) \nu_x] [\bar{y} \gamma_\alpha (g_V - g_A \gamma_5) y] \quad (1.28)$$

with the constants as defined previously. The Fermi constant G_F , the Wienberg angle θ_W and where g_ν and g_A are constants relating to strong interactions from v-a theory.

Lagrangian for CC scattering, $\nu_x y \rightarrow \nu_y x$:

$$\mathcal{L} = -\frac{G_F}{\sqrt{2}} [\bar{\nu}_x \gamma_\alpha (1 - \gamma_5) x] [\bar{\nu}_y \gamma_\alpha (1 - \gamma_5) y] \quad (1.29)$$

From the Lagrangian the cross-sections are calculated by first calculating the interaction amplitude by using the initial and final states to evaluate the Lagrangian. This amplitude can then be related to a derivative of the cross-section with can be integrated to provide the final cross-section. The details can be found in [16].

The various processes involving an electron as an initial state with their calculated cross-sections can be seen in table 1.1 where the variable s is the mandelstam variable, $s = (p_{\nu_\mu} + p_e)^2 = 2m_e E_{\nu_\mu}$

Table 1.1: Neutrino interactions with electrons

Type	Process	Cross-section
CC interaction	$\nu_\mu + e^- \rightarrow \mu^- + \nu_e$	$\frac{G_F^2 s}{4\pi}$
CC+NC Scattering	$\nu_e + e^- \rightarrow \nu_e + e^-$	$\frac{G_F^2 s}{4\pi} [(2 \sin^2 \theta_W - 1)^2 + \frac{4}{3} \sin^2 \theta_W]$
CC+NC Scattering	$\bar{\nu}_e + e^- \rightarrow \bar{\nu}_e + e^-$	$\frac{G_F^2 s}{4\pi} [\frac{1}{3}(2 \sin^2 \theta_W + 1)^2 + 4 \sin^2 \theta_W]$
NC Scattering	$\nu_\mu + e^- \rightarrow \nu_\mu + e^-$	$\frac{G_F^2 s}{4\pi} [(2 \sin^2 \theta_W - 1)^2 + \frac{4}{3} \sin^2 \theta_W]$
NC Scattering	$\bar{\nu}_\mu + e^- \rightarrow \bar{\nu}_\mu + e^-$	$\frac{G_F^2 s}{4\pi} [\frac{1}{3}(2 \sin^2 \theta_W - 1)^2 + 4 \sin^2 \theta_W]$
Neutrino pair production	$e^+ + e^- \rightarrow \nu_e + \bar{\nu}_e$	$\frac{G_F^2 s}{12\pi} [\frac{1}{2} + 2 \sin^2 \theta_W + 4 \sin^4 \theta_W]$
Neutrino pair production	$e^+ + e^- \rightarrow \nu_\mu + \bar{\nu}_\mu$	$\frac{G_F^2 s}{12\pi} [\frac{1}{2} - 2 \sin^2 \theta_W + 4 \sin^4 \theta_W]$

To make it simpler for calculations and visualization these interactions have been plotted as Feynman diagrams in figure 1.4, figure 1.5 and figure 1.6.

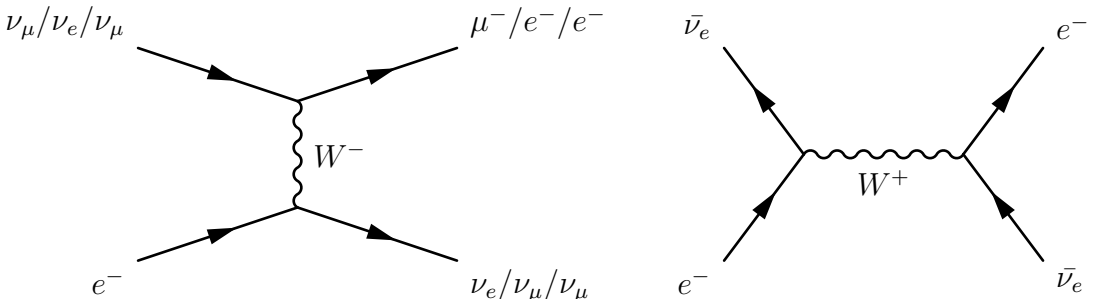


Figure 1.4: Charge interaction between neutrinos and electrons

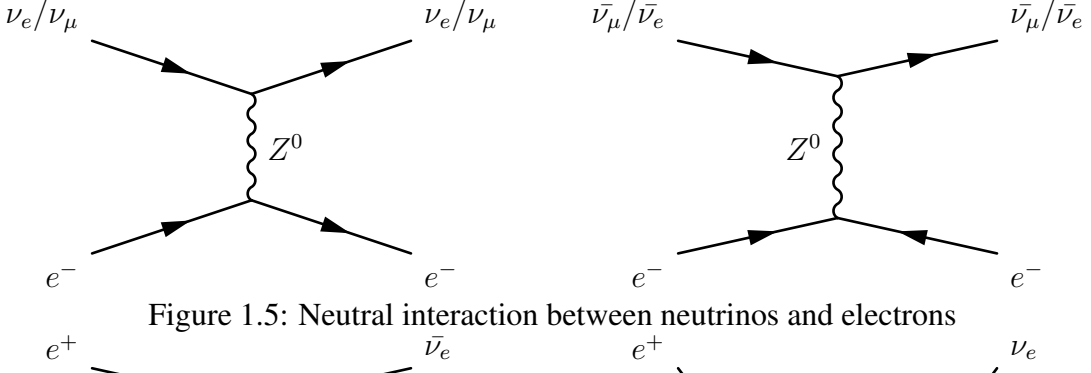


Figure 1.5: Neutral interaction between neutrinos and electrons

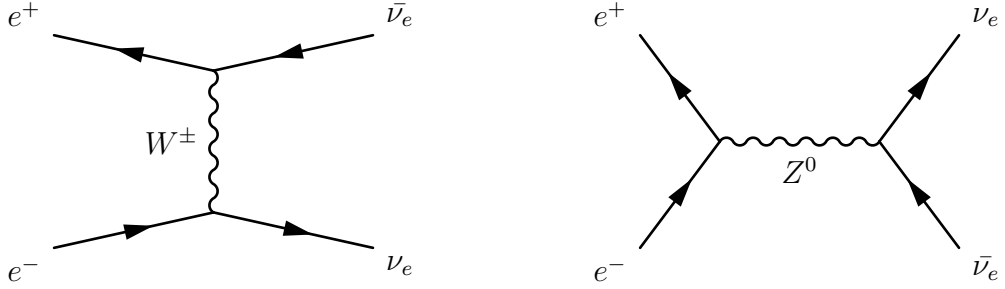


Figure 1.6: Neutrino pair production

1.4.2 Neutrino-quark scattering

Moving away from electrons into quarks one has to take into account that quarks are always bound in a hadron, and thus do not exist in a free state.

Neutrino-quark interactions can be understood in two different ways. Starting with inverse beta-decay where a proton interacts with an anti-neutrino producing a positron and neutrino, $\bar{\nu}_e + p \rightarrow e^+ + n$, can be seen as an interaction where the full hadron interacts and only changes its weak charge instead of seeing each quark interact separately. The interacting particle, the proton, changes into another baryon the neutron. However at higher energies it is possible for the quark to become ejected from the proton and the interaction changing the proton from a baryon into a meson.

1.4.2.1 Quasi-elastic interactions

Quasi-elastic relates to when the neutrino interacts with the proton as a whole. This however requires some factors for modelling the nucleus as a whole, compared to the electron which was seen as point-like. The cross section is given as:

$$\sigma(\bar{\nu}_e + p \rightarrow e^+ + n) = \frac{G_{FS}}{\pi} \times \cos^2 \theta_C \times \xi_{mass} \times (g_v^2 + 3g_A^2) \quad (1.30)$$

with corrections for charge-current quark mixing transition from u to d quark ($\cos^2 \theta_C$), a mass suppression factor ξ_{mass} and proton form factors $g_v^2 + 3g_A^2$ [18].

It is also interesting to note that apart from inverse beta-decay which is a CC interaction, an Quasi-elastic NC interaction can also happen $\nu_\mu + p \rightarrow \nu_\mu + p$ which knocks on the proton

but does not change it.

1.4.2.2 Deep inelastic scattering

If the neutrino has an energy of around or above 1 GeV there is enough energy that the neutrino can break up the nucleon and interact with the quarks as if they were free particles. It becomes quite difficult to calculate the cross-section for these interactions as it depends on the final particle(s) as well as understanding the so called form factors relating the quarks to the proton. DIS comes with both a charge current and neutral current modes as $\nu_\mu + p \rightarrow \mu^- + X$ or $\nu_\mu + p \rightarrow \nu_\mu + X$.

More details can be found in [18].

1.4.2.3 Resonant interactions

Between the elastic and inelastic region is an area associated with pion production through the excitation of baryon resonances, $\nu_i + N \rightarrow l + N^*$ where the nucleus further decays $N^* \rightarrow \pi + N'$. Two examples with delta particles can be seen below.

$$\nu_\mu + N \rightarrow \mu^- + \Delta^{++} \rightarrow \mu^- + p + \pi^+ \quad (1.31)$$

$$\nu_\mu + N \rightarrow \mu^- + \Delta^+ \rightarrow \mu^- + n + \pi^+ \quad (1.32)$$

1.4.3 Comparing neutrino interactions to QED

It is interesting to compare the probability for Charge Current and Neutral Current interactions with the equivalent QED or electromagnetic interactions. In figure 1.7 a comparison is made between QED and a weak interaction with the same initial and final states. Calculating the cross-sections when $E \ll M_Z$ the following quotient is produced: $\frac{\sigma_{Weak}}{\sigma_{QED}} \approx (\frac{s}{M_Z^2})^2$ where s is the square of the center of mass energy, M_Z is the mass of the Z-boson. Currently the Z-boson mass is 91.1876GeV [12] but since s varies it is hard to give a value to the quotient. For the energy range where $E \ll M_Z$ this quotient varies from $0.01 \rightarrow 0.1225$. With the current values QED is approximately 100 times more likely to occur than a weak interaction..

The CC and NC examples in figure 1.8, with electrons and muon neutrinos, so that the final states can be distinguished, the cross sections of both can be written as $\sigma_{CC}(\nu_\mu e^-) \approx \frac{G_F^2 s}{\pi}$ and $\sigma_{NC}(\nu_\mu e^-) \approx \frac{G_F^2 s}{\pi} [(-\frac{1}{2} + \sin^2 \theta_W)^2 + \frac{1}{3} \sin^4 \theta_W]$ where G_F and θ_W are defined above. This gives a relation CC and NC as $\frac{\sigma_{CC}}{\sigma_{NC}} = 1 / [(-\frac{1}{2} + \sin^2 \theta_W)^2 + \frac{1}{3} \sin^4 \theta_W] \approx 11$. With the current values CC is approximately 11 times more likely to occur than NC.

¹If $f = e^-$ a T-channel diagram has to be added as well

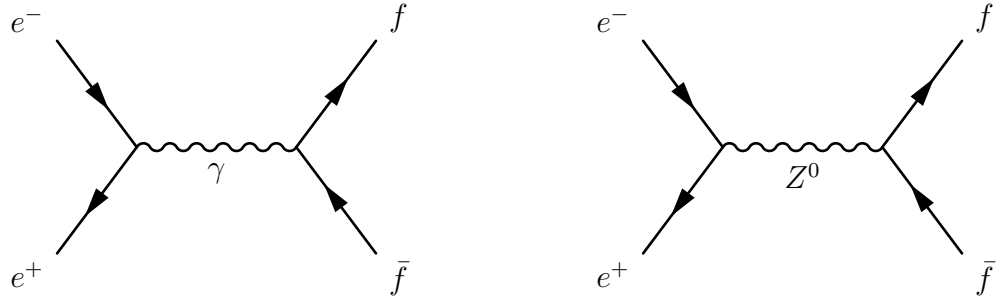


Figure 1.7: The QED and the weak contributions to the scattering electron-positron to any quark or lepton pair.¹

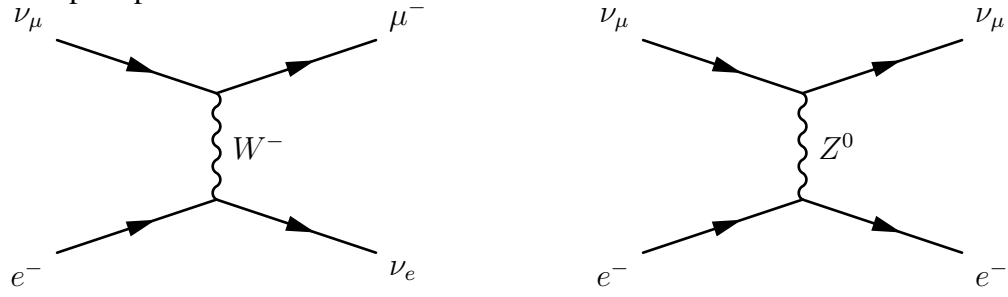
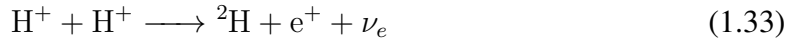


Figure 1.8: Feynman diagrams, CC(Left) and NC(Right) with the same initial states.

1.5 Missing neutrinos

The sun generates energy principally through the proton-proton chain reaction [19]. In this chain electron neutrino are produced through proton-proton interactions and beta decay processes.



The proton-proton interaction has the highest flux, $6.1 \times 10^{10} \text{ cm}^{-2} \text{ sec}^{-1}$ but produces neutrinos at very low energies ($< 0.4 \text{ MeV}$) making them difficult to detect. Further on in this chain a Boron decay,



produces electron neutrinos with energies up to 18 MeV, however the fluxes are much lower than proton-proton interactions, $3.2 \times 10^6 \text{ cm}^{-2} \text{ sec}^{-1}$. Neutrinos in this energy can be used in inverse-beta decay transforming chlorine into argon.



The amount of argon can then be counted by measuring x-rays comming from the decaying argon isotope and related to the neutrino flux. The Homestake experiment used this technique and ran from 1970 until 1994 with a goal to measure the flux of electron neutrinos. They measured the flux of electron neutrinos and found only around 1/3, (1.75/4.7), of the expected value from the theoretical model of the nuclear reactions in the core of the sun [20].

This results shock the whole neutrino field by suggesting something fundamentally wrong in the understanding of the neutrino, either in the interactions or in the solar model. There

were various solar experiments which confirmed the solar neutrino model [19] implying something wrong in the interaction model. At the same time measurements were performed at several other detectors, Sudbury Neutrino Observatory (SNO) [21], Kamiokande [22] and Super-Kamiokande [23] all in agreement with a lesser flux. Further information from the measurement at SNO hinted at the fact that additional neutrino flavours may be produced, contradicting the verified solar neutrino model. One of the possible explanations for the deficit was neutrino oscillations proposed by Bruno Pontecorvo [24].

The oscillation model is in good agreement with experimental values and was verified at SNO and Super-Kamiokande awarding the neutrino flavour oscillation measurements with Nobel prizes in 2015 and paved the way for physics beyond the Standard Model.

1.6 Neutrino mass and oscillation in vacuum

While looking at an analog of neutral kaon mixing for neutrinos Bruno Pontecorvo, in 1957, developed the concept of neutrino-antineutrino transitions [24]. Even though to date no matter-antimatter oscillation had been observed, the concept formed the foundation of lepton mixing, which was developed by Maki, Nakagawa, and Sakata [25] and refined into a neutrino flavour oscillation model by Bruno Pontecorvo. They managed to show that neutrino mixing is a natural outcome of adding neutrino mass to a gauge theory [24]

The relation between the flavour and mass eigenstates can be expressed as,

$$|\nu_\alpha\rangle = \sum_i U_{\alpha i}^* |\nu_i\rangle, |\bar{\nu}_\alpha\rangle = \sum_i U_{\alpha i} |\bar{\nu}_i\rangle \quad (1.36)$$

where $|\nu_\alpha\rangle$ is a neutrino with a fixed flavour, α is one of $\{e, \mu, \tau\}$ and $|\nu_i\rangle$ is a neutrino with a fixed mass. U is the Pontecorvo-Maki-Nagawa-Sakata (PMNS) matrix in (1.37),

$$U = \begin{pmatrix} c_{12} & s_{12} & 0 \\ -s_{12} & c_{12} & 0 \\ 0 & 0 & 1 \end{pmatrix} \begin{pmatrix} 1 & 0 & 0 \\ 0 & c_{23} & s_{23} \\ 0 & -s_{23} & c_{23} \end{pmatrix} \begin{pmatrix} c_{13} & 0 & s_{13} e^{i\delta_{CP}} \\ 0 & 1 & 0 \\ -s_{13} e^{-i\delta_{CP}} & 0 & c_{13} \end{pmatrix} \times \begin{pmatrix} 1 & 0 & 0 \\ 0 & e^{i\phi_2} & 0 \\ 0 & 0 & e^{i\phi_3} \end{pmatrix} \quad (1.37)$$

where $s_{ij} = \sin \theta_{ij}$ and $c_{ij} = \cos \theta_{ij}$ with θ_{ij} the three mixing angles and δ_{CP} , ϕ_2 and ϕ_3 are complex phases. The parameters ϕ_2 and ϕ_3 are only non-zero if neutrinos are their own antiparticles, denoted as Majorana, which is still unknown at the time of writing this [12]. This would be an interesting result as it would imply a splitting with the relation to the Higgs field. The three first matrices are denoted the Dirac part of the PMNS matrix and the final forth matrix is the Majorana term which is non-identity only if neutrinos are Majorana.

The probability of finding a neutrino in a specific time-dependent state is related to the mass states through the PMNS matrix elements and the time-evolution operator. The PMNS introduces a rotation in the space of mass eigenstates. The derivations of the oscillation probability for two-neutrino and three-neutrino oscillations can be found in the literature [9]. The three neutrino flavour state shown in equation 1.36 evolves as a function of time as:

$$|\nu_\alpha(t)\rangle = \sum_i e^{-iE_i t} U_{\alpha i} |\nu_i\rangle \quad (1.38)$$

which gives the probability of flavour evolution as

$$P_{\nu_\alpha \rightarrow \nu_\beta}(t) = |\langle \nu_\beta | \nu_\alpha \rangle|^2 = \sum_{i,j} |U_{\alpha i} U_{\beta i}^* U_{\alpha j} U_{\beta j}^*| \cos[(E_i - E_j)t - \arg(U_{\alpha i} U_{\beta i}^* U_{\alpha j} U_{\beta j}^*)] \quad (1.39)$$

$$E_\alpha = \sqrt{\vec{p}^2 + m_i^2} \approx |\vec{p}| + \frac{m_i^2}{2|\vec{p}|} \quad (1.40)$$

If one has a beam of neutrinos in an initial flavour state $|\nu_\alpha\rangle$, the probability to find the neutrinos changing to flavour state $|\nu_\beta\rangle$, after a distance x , is given by

$$P_{\nu_\alpha \rightarrow \nu_\beta}(x) = |\langle \nu_\beta | \nu_\alpha \rangle|^2 = \sum_{i,j} |U_{\alpha i} U_{\beta i}^* U_{\alpha j} U_{\beta j}^*| \cos \left[\frac{2\pi x}{L_{ij}} - \arg(U_{\alpha i} U_{\beta i}^* U_{\alpha j} U_{\beta j}^*) \right], \quad (1.41)$$

where the approximate energy-momentum relationship of equation 1.40 has been taken into account, where the oscillation length is given by $L_{ij} = \frac{4\pi|\vec{p}|}{|m_i^2 - m_j^2|} = \frac{4\pi|\vec{p}|}{|\Delta m_{ij}^2|}$ and \vec{p} is the 3-momentum of the neutrinos in the initial beam.

If is worth noting that the equation can be simplified assuming only oscillation into one flavour:

$$P_{\nu_\mu \rightarrow \nu_y}(x) = \sin^2(2\theta_{\mu y}) \sin^2 \left(\frac{1.27 \Delta m_{\mu y}^2 x}{E_\nu} \right) \quad (1.42)$$

where 1.27 is a unit constant which comes when Δm^2 is given in units of eV^2 , x in meters and E_ν is MeV .

The mass-squared difference between neutrino mass states $|m_i^2 - m_j^2|$ has to be different from zero for there to be neutrino oscillations, so at least one of the neutrinos must have non-zero mass which currently is not explained through the Standard Model. Furthermore, if the elements of the PMNS matrix $U_{\alpha i}$ are all real then $\arg(U_{\alpha i} U_{\beta i}^* U_{\alpha j} U_{\beta j}^*) = 0$ and the CP-violating phase $\delta_{CP} = 0$. The current experimental focus lies with trying to measure values for all these parameters. Current values of the neutrino masses can be found in table 1.2

Looking at the oscillation probability (1.41) two main classes of experiments for neutrino oscillations can be devised. Finding a distance x to the source where $P_{\nu_\alpha \rightarrow \nu_\alpha}(x) < 1$, it is possible to look at so called disappearance of the beam by comparing the expected neutrino flux to the observed. For the disappearing flavour there must be a probability, $P_{\nu_\alpha \rightarrow \nu_\beta}(x) > 0, \alpha = \beta$ for another flavour to appear. The second kind of experiment, denoted as appearance, is based on looking for interaction products which are impossible without oscillations. An example of this would be to see a positron from a muon neutrino beam. More on this can be found well described in [9] and examples of different detectors

will be discussed in chapter 2. As a rule of thumb this L has to be on the order of km for energy ranges between MeV to GeV. This means that oscillations will have a small effect on short scale neutrino interactions measured close to the source.

Charge conjugation and parity (C and P, CP) symmetry states that physics should be the same for particles and anti-particles while the spatial coordinates are inverted. If δ_{CP} is non-zero it would imply CP symmetry is violated it would imply a difference between the rate of neutrino and anti-neutrino oscillations and could be responsible for the matter-antimatter asymmetry of the early universe. Current best-fit values (at 90% confidence limit) have $\delta_{CP} = -1.79 \pm 1.42$ for normal mass ordering and $\delta_{CP} = -1.41 \pm 0.68$ for inverted mass ordering both rejecting the null hypothesis for δ_{CP} at around 3σ [26].

Table 1.2 provides the current mass limits for neutrinos, note that currently there is no lower limit since it is only known that at least two of the neutrinos must have mass.

Particle	95% CL Mass limit (MeV)	95% CL Anti-particle mass limit (MeV)
ν_e	< 0.225	$< 2 \cdot 10^{-3}$
ν_μ	< 0.19	No Data
ν_τ	< 18.2	No Data

Table 1.2: Current upper neutrino mass limits [12]

1.7 CP-violation, baryogenesis and leptogenesis

According to the Big Bang theory, matter and anti-matter were created in equal amounts[27]. Through observations of the universe, much more matter has been found compared to anti-matter. This constitutes one of the major unsolved problems in physics, where is all the anti-matter? There has currently not been any sign of an annihilation horizon, where matter and anti-matter interact nor has there been any sign of this in the cosmic background radiation[27]. One direct measurement was AMS-01, (Alpha Magnetic Spectrometer), which measured the ratio of anti-helium to helium in the universe to be of the order of 10^{-6} [28].

The follow-up experiment, AMS-02, which is operational in the International Space Station, confirmed these results and measured the antibaryon component of the universe to be $\sim 10^{-9}$ less than that of baryons [29]. As of now our current models account this difference to be $O(1)$ thus a factor of 10^9 too small[30]. This implies that there must be a yet unknown process to account for the difference.

There exist two approaches to explain the matter asymmetry of the universe. The first is baryogenesis which studies possible mechanisms to enhance the baryon-antibaryon asymmetry, and the second is leptogenesis, in which CP violation in leptons translates into a baryon asymmetry. Leptogenesis will be covered in this thesis as it relates to neutrinos also it should be added that there are theories which explain baryogenesis through leptogenesis.

If neutrinos violate CP by their oscillations being different for neutrinos and anti-neutrinos, this could explain the matter anti-matter imbalance that has been observed. CP-violation exists in the Standard Model but it cannot explain the observed difference [16], and measurements of the CP-violation in neutrino oscillations have not yet been able to show any conclusive results [31].

1.7.1 Current theory of leptogenesis

Andrei Sakharov proposed three necessary conditions that any baryon-generating interaction, which would produce matter antimatter imbalance, must satisfy [32]. These conditions are:

- Baryon number violation.
- C-and CP-violation.
- Deviation from thermal equilibrium.

The first condition is very important in that it related cosmological models with models in particle physics. It also gives us a way to produce an excess of baryons over anti-baryons,

as long as there is no reverse interaction, hence requiring the C violation. CP-violation is needed to counteract the balancing as well and finally out of thermal equilibrium to get around CPT-symmetry. As briefly mentioned previously the second condition is fulfilled in the SM, but not enough, and the third can always be satisfied.

In [33] a number of viable scenarios for baryogenesis are briefly discussed, for instance Grand Unified theories, heavy Majorana neutrinos and supersymmetry.

1.8 Introduction to explaining neutrino masses

The problem with neutrino masses is that we only see left-handed neutrinos. The standard way for fermions to obtain a mass through interaction with the Higgs field is through a three point interaction involving a left-handed fermion, a right-handed fermion, and the Higgs field. With no right handed neutrinos, there is no way to form such interactions, which lead to a mass term after symmetry breaking. This leaves the exact mechanism by which neutrinos acquire mass a mystery. When SM was created neutrinos were assumed to be massless since they were only left-handed. There are three main reasons to why the neutrino mass must be zero in the SM:

- There is no renormalizable operator which allows for a neutrino mass without introducing either an additional Higgs particle or by introducing right-handed neutrinos, neither of which have currently been observed.
- The current Higgs is an $SU(2)_L$ doublet, thus it requires fermions to have both chiral states to provide mass. It could be possible to introduce further Higgs particles which do not require this.
- There are no right-handed neutrinos. Right-handed neutrinos could be introduced which would allow the current Higgs or any other current mechanism to provide mass. This is because the right-handed neutrino will be modeled as a singlet state in the extended-SM.

There are different ongoing searches to find all categories of solutions, higher-order operators (non-renormalizable), other Higgs particles (Non $SU(2)_L$ doublets) and right-handed neutrinos.

In this thesis the focus will be on introducing right-handed neutrinos. There are two main mass terms both related to the Higgs mechanism, the so called Dirac term and the Majorana term.

1.8.1 Dirac neutrinos

Naively introducing right-handed neutrinos makes an assumption that neutrinos and anti-neutrinos are distinct particles, however since the neutrino is electrically neutral, this does not have to be the case.

Introducing right-handed neutrinos introduces particles which will not interact in the SM since the electroweak interaction model only couples to left handed neutrinos. Thus right-handed neutrinos are often denoted sterile neutrinos and only interact through gravity. This introduces sterile neutrinos as a possible candidate as dark matter [34, 35].

The main problems with this description is both that no right-handed neutrinos have been detected and that the observed neutrino mass measurement requires a weaker coupling for neutrinos compared to the other leptons.

Dirac neutrinos could be experimentally verified by finding neutrino being different to anti-neutrinos or by finding both right-handed neutrinos and left-handed neutrinos as different particles.

1.8.2 Majorana neutrinos

Removing the assumption that neutrinos and anti-neutrinos are distinct allows for a simplified model. Right handed neutrinos have to be produced to conserve lepton number conservation but not to introduce a mass mechanism. Majorana mass also has no equivalent for other leptons and could explain the the neutrino mass is so small. Majorana neutrinos would allow neutrinoless double beta decay[36] as an experimental verification.

1.9 Summary

In this chapter the theory of neutrino interactions as well as the history of neutrinos have been introduced. The current issues with neutrinos in the SM and open questions have been presented.

Chapter 2

Neutrino experiments

2.1 Introduction

Since the discovery of the neutrino in 1956 by Reines and Cowan [4] a multitude of neutrino experiments have tried to measure the properties of the different neutrino flavours. Since the Homestake experiment many other experiments have been run to measure neutrino oscillations and the mass of the neutrinos. A detailed description of these experiments is outside of the scope of this thesis, however in this section a description into the main types of experiments and milestones will be presented.

Neutrino experiments are split into three different categories based on their primary neutrino source. Each type features its own advantages and issues. The detector types are:

- Atmospheric
- Solar
- Accelerator
- Reactor

Each will be described briefly before examples are given.

2.2 Atmospheric

As mentioned in section 1.5 neutrinos at low energy ranges ($< 18\text{MeV}$) are produced through nuclear interactions in stars. There are other cosmological phenomena which produce neutrinos, and some searches are looking for signs of new physics in these signals.

The Earth is constantly bombarded by cosmic-ray particles from space. When they hit the atmosphere, these high-energy protons interact with air molecules to produce showers of pions, which subsequently decay to muons and muon-neutrinos. This process is similar to that used to produce neutrino beams from particle accelerators. Early observations of atmospheric neutrinos were contradictory, with some experiments observing approximately the expected ratio while others saw significantly fewer muon-neutrinos than expected, similar to the missing solar neutrinos, the Atmospheric Neutrino Anomaly. This was a measurement done by Super-Kamiokande and confirmed, together with the Homestake experiment, the existence of neutrino oscillations.

The atmospheric neutrinos are produced from cosmic-rays interacting through nuclear interactions producing pions which decay into muons and producing neutrons through the following interactions:

$$\pi^\pm \rightarrow \mu^\pm \nu_\mu (\bar{\nu}_\mu) \quad (2.1)$$

$$\mu^\pm \rightarrow e^\pm \bar{\nu}_e \nu_\mu (\nu_e \bar{\nu}_\mu) \quad (2.2)$$

producing neutrinos with energy that can be in the GeV to PeV range. However, it is impossible to control the source and difficult to get many events due to the low fluxes expected from cosmic rays.

Looking at the two flavour oscillation formula:

$$P_{\nu_\mu \rightarrow \nu_y}(x) = \sin^2(2\theta_{\mu y}) \sin^2 \frac{1.27\Delta m_{\mu y}^2 x}{E_\nu} \quad (2.3)$$

these experiments are looking for a specific θ for a given Δm^2 in the two oscillation formula. Starting with ν_μ going to τ or e as $P_{\nu_\mu \rightarrow \nu_x} = \sin^2(2\theta) \sin^2 \frac{1.27\Delta m^2 D}{E_\nu}$ with θ the mixing angle between states, δm^2 the difference of the neutrino masses squared, D is the distance from the creation point (km) and E_ν the energy of the neutrino in GeV. Given the current experimental values, these experiments are best suited to look for θ_{23} and $|\Delta m_{32}^2|$.

2.2.1 Historical experiments

In the beginning of the 1960s the Kolar Gold Fields (KGF) experiment, in a mine in the Kolar rock, was the first experiment to record an atmospheric neutrino by detecting an inelastic neutrino event in the large amount of rock covering the experiment producing two distinct muon track through charge current interaction and muon decay through $\nu + N \rightarrow N' + \mu_W$ with $W \rightarrow \mu + \nu$ [37]. This lead to estimating the neutrino induced muon interaction flux. It was also the first usage of a Cherenkov detector. Cerenkov light is emitted when a particle travels faster than the speed of light inside a medium. This creates a shock wave similar to the sonic boom that is visible in nuclear reactors as a bluish light.

At the same time a similar experiment in the E.R.P. Mines in South Africa reproduced the results and improved some of the measurements [37].

2.2.2 NUSEX

The NUSEX detector, installed in the Mont Blanc tunnel, collected data between June 1982 and 1988 and was a cube 3.5m^3 consisting of 134 iron plates with plastic streamer tubes interlaced between the different iron plates providing 150 tons of instrumented mass figure 2.1. One of the main results from NUSEX was that they could not measure any difference between electron and muon neutrino interaction probabilities, figure 2.2, as then expected from the Kamiokande experiment [38, 39].

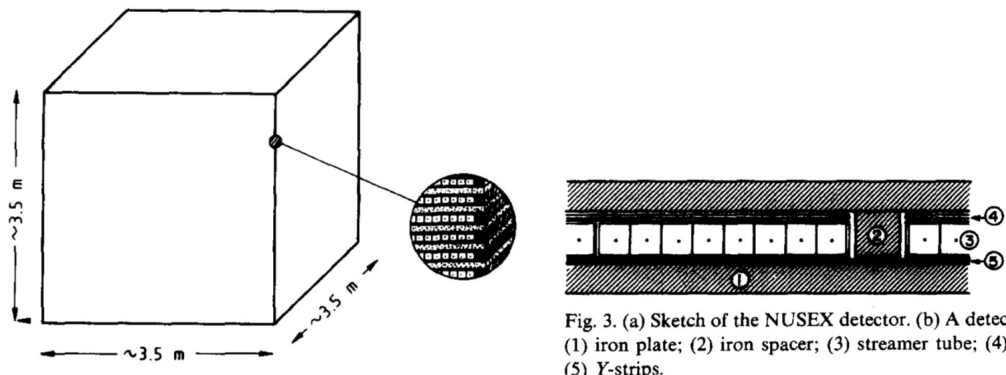


Fig. 3. (a) Sketch of the NUSEX detector. (b) A detector plane:
 (1) iron plate; (2) iron spacer; (3) streamer tube; (4) X-strips;
 (5) Y-strips.

Figure 2.1: A sketch of the NUSEX detector with various parts highlighted [38].

2.2.3 KamiokaNDE

The Kamioka Nucleon Decay Experiment (KamiokaNDE) is a 3000 ton water Cherenkov detector installed in the Kamioka mine 1000 m under the top of a mountain. The detector

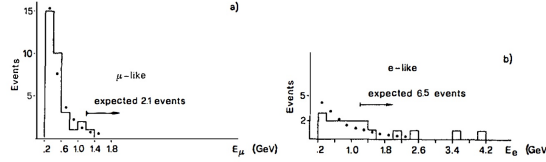


Fig. 2. Observed (continuous line) and expected (dots) energy spectra for the lepton candidate:
a) muon, b) electron. The expected spectra are normalized to the observed number of events.

Figure 2.2: Data compared to Monte Carlo for 50 neutrino events in the NUSEX and showing consistency within errors [39].

has the aim to study and search for nucleon decay which began operation in 1983. The Cherenkov light is detected using 1000 large PhotoMultiplier Tubes (PMTs) [40].

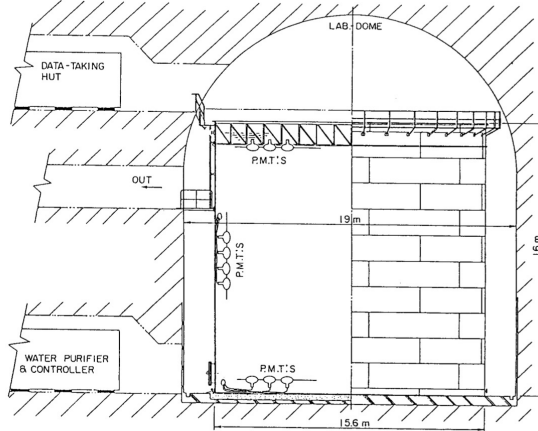


Fig. 2. Schematic picture of the $3,000 \text{ m}^3$ water tank and phototube support system.

Figure 2.3: Schematic image of the KamiokaNDE detector. [40].

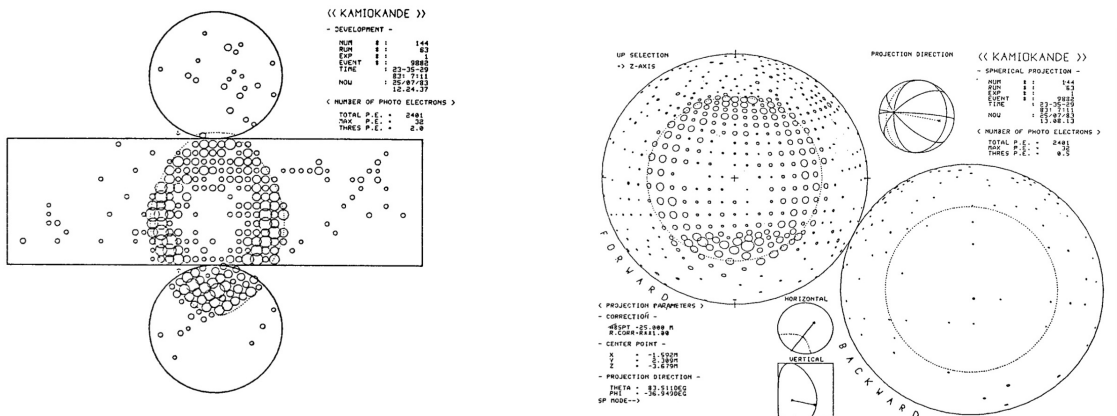


Fig. 10. An example of one Cherenkov ring pattern observed for a neutrino-induced muon event. (a) A normal picture

Fig. 10 (b) in 3-dimentional way.

Figure 2.4: A sample event showing Cherenkov rings produced by a muon event [40].

The main result was finding a slight discrepancy between data and simulations, seen in figure 2.5, hinting at a possibility that atmospheric neutrinos were oscillating.

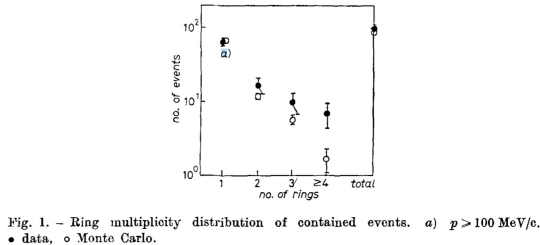


Figure 2.5: Comparing ring multiplicity distributions between data and simulations [41].

2.2.4 IMB

The Irvine- Michigan-Brookhaven (IMB) groups build a 8 kiloton water Cherenkov detector 600 m under the Morton Salt Mine in Cleveland which began data taking in 1986. The design was similar to KamiokaNDE and managed to improve several results including improving the parameter space of neutrino oscillation [42].

2.2.5 Super-Kamiokande

Super-Kamiokande[43], a water Cherenkov detector is located 1 km underground and consists of a cylindrical stainless steel tank holding 50 ktons of ultra-pure water, performed the first experimental observation that the neutrino has non-zero mass [23] and also managed to detect strong evidence of muon neutrino oscillation to tau neutrinos from the analysis of atmospheric neutrinos interacting in the water target figure 2.6. The deviation from 1 shows the discovery of neutrino oscillations and the lines show the expected shape for oscillation from muon neutrinos to tau neutrinos [23]. It also shows that electron-like events have no significant variation in length over neutrino energy where at large length over neutrino energy muon-like events have come to close to half of the initial rate.

2.2.6 MACRO

The Monopole, Astrophysics and Cosmic Ray Observatory (MACRO) was combined of liquid scintillation counters, limited streamer tubes and nuclear track detectors allowing it to searching for signs of magnetic monopoles, as well as being able to operate as a neutrino detector as well as search for other phenomena. Data was taken between 1995 until 2000

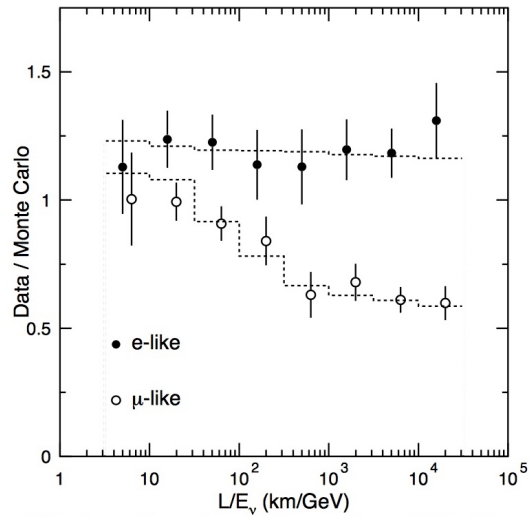


Figure 2.6: Comparison of the ratio of data vs Monte Carlo vs length over neutrino energy for fully contained atmospheric electron-like and muon-like events [23].

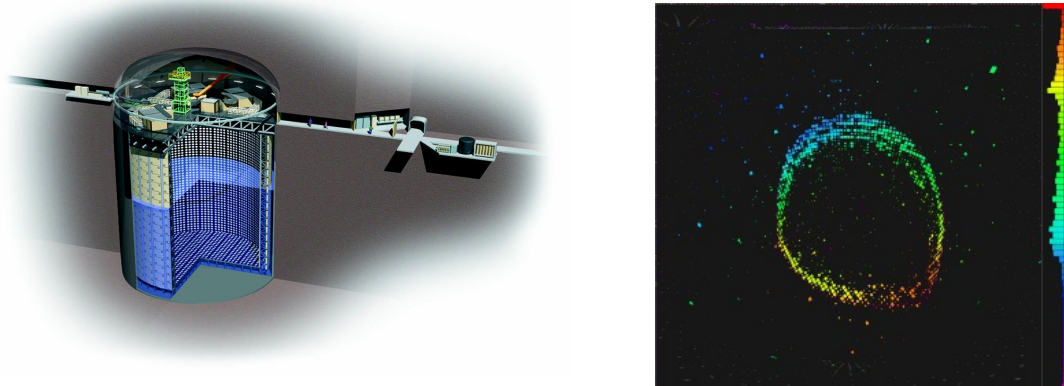


Figure 2.7: Left) A schematic of the Super-K detector., Right) Event recorded in Super-K.

and by measuring neutrino induced muons, the MACRO managed to aid in the discovery of atmospheric neutrino oscillation [44]

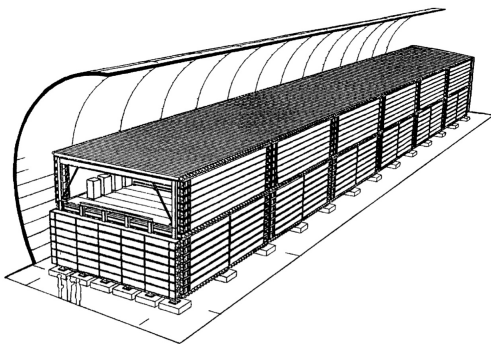


Figure 2.8: Schematic of the MACRO [45].

2.3 Solar

The mechanism for neutrino generation in the sun was briefly discussed in subsection 1.5. Solar neutrinos are interested for both allowing a unique way of probing the internal solar reactions as well as providing a very baseline combined with energies of around $1\text{MeV}/c$ allowing probing of mass differences in the range of $\Delta m^2 \approx 10^{-10}\text{eV}^2$ through neutrino oscillation, see equation 1.42. Based on current experimental values these experiments are sensitive for θ_{12} and Δm^2_{12}

2.3.1 Super-Kamiokande

Super-Kamiokande, as described above, could thanks to its design, also be used for solar neutrino studies and extended the neutrino oscillation analysis to lower mass difference values as well as performed solar interaction measurements [46].

2.3.2 SNO

The Sudbury Neutrino Observatory (SNO) [21] was build to make a definite measurement of solar neutrinos following the measurements taken by the Homestake experiment [20]. It utilized PMT (Photo Multiplier Tubes) to measure Cherenkov radiation produced by neutrino interactions in the detectors 1000 ton ultra-pure heavy water volume. The whole detector is placed 2 km underground to minimize background interactions. It expanded on looking for a specific energy range for cosmic rays, from boron decay, to becoming a generic neutrino detector meaning that other atmospheric and cosmic neutrinos became background events for measuring solar neutrinos. The experiment has a unique ability to separate the reactions between electron neutrino charge current (CC), neutral current interactions (NC) with all flavours of neutrinos and with electron scattering (ES). With this observed neutrino flux

observed through CC reactions could be compared to that of the ES and NC to provide evidence for a neutrino flavour change regardless of the predictions of solar modes.

The experiment clearly showed a significant difference in flux between CC interactions, only available with electron neutrinos compared to expected and compared to the NC and ES interactions. The result can be seen in figure 2.10.

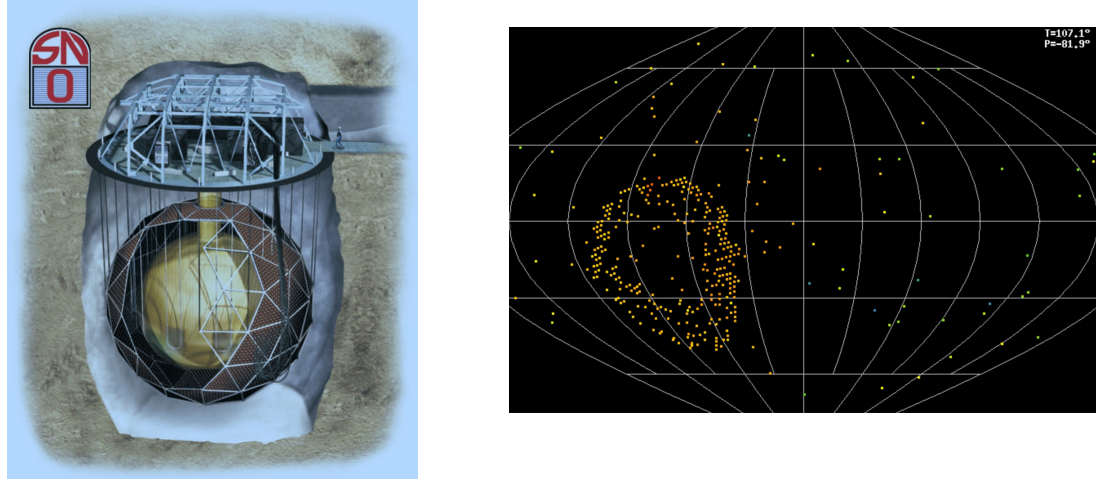


Figure 2.9: Left) A schematic drawing of the SNO detector [21], Right) Cherenkov light recorded from a muon created by interaction of an atmospheric neutrino in the heavy water.

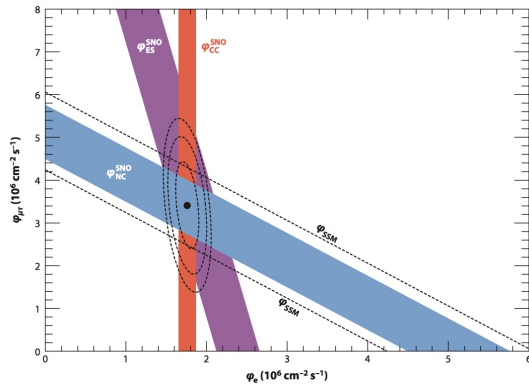


Figure 2.10: The flux of solar neutrinos of μ or τ flavour vs flux of electron neutrinos measured in SNO from the three reactions, CC in red, ES in purple and NC in blue. The diagonal dashed lines show the prediction from the Standard Solar Model. The coloured bands intersect at the fit values for all fluxes indicating that they are consistent with neutrino flavour transformation with no distortion in the solar neutrino energy spectrum. [21].

The experiment is currently replacing the heavy water with liquid scintillator and renaming itself as SNO+ [47].

2.3.3 Borexino

Borexino is a liquid scintillator detector making it more sensitive, especially to the low energetic solar neutrinos, than Cherenkov techniques but lacks the ability to detect directionality of incoming particles requiring an extremely low radioactive contamination of the scintillator media. This is handled by containing the detector within shielding material and utilizing ultra pure materials [48]. The scintillating light is then read out by PMTs uniformly distributed around the active volume seen in figure 2.11.

The experiment started data taking in May 2007 and is still ongoing. It has the goal of making very precise measurements of solar neutrinos fluxes as well as setting limits on charge non conservation, limits on sterile neutrinos and measuring geoneutrinos.

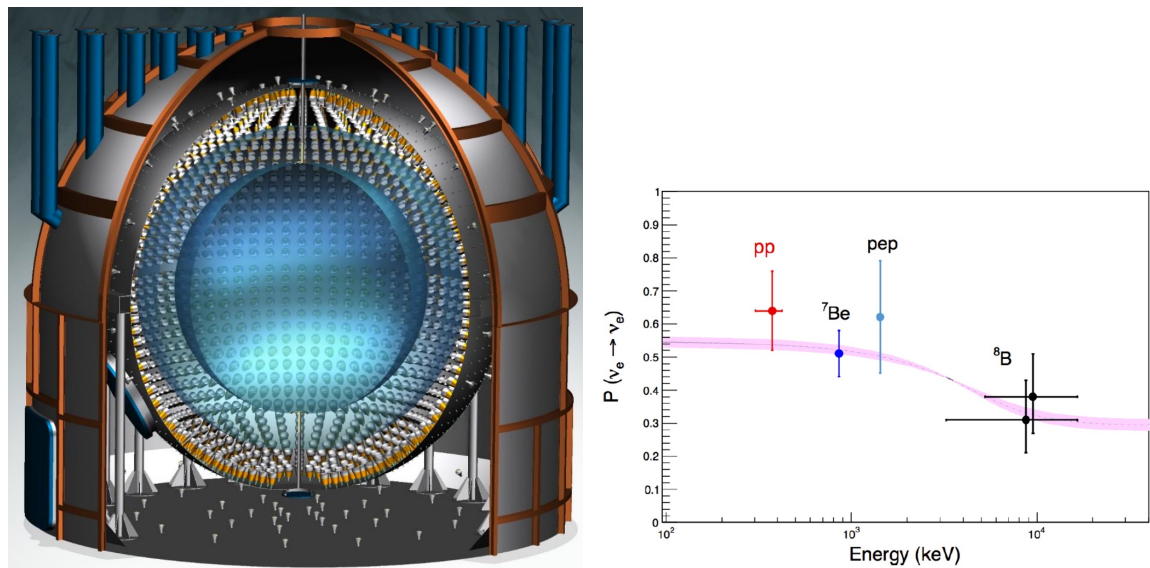


Figure 2.11: (Left) Schematic of the Borexino experiment [48]. (Right) Electron neutrino survival probability as a function of neutrino energy according representing different neutrino solar production channels both from the Solar standard model and measurements from the Borexino experiment [48].

2.4 Accelerator

Currently accelerator facilities can produce muon and electron neutrinos as well as anti neutrinos from accelerated protons. Protons are accelerated in a particle accelerator where the energy of the neutrino will be related to the energy of the protons. The proton beam is then directed at a target where the protons interact with the target material, producing a large number of secondary pions (among other particles). Shaped magnetic fields, so called focusing horns, are used to select out pions of the preferred charge (positive for a neutrino beam, negative for an antineutrino beam) in a specific momentum range and focus them into a collimated beam. The beam is directed into a long decay volume, where the pions decay into muons and (anti)neutrinos. At the end of the decay volume there is a large mass of material which absorbs all the particles except the neutrinos. This provides a nearly pure beam of muon-neutrinos (or muon-antineutrinos if negatively charged pions are selected). There is some inevitable contamination from antineutrinos in the neutrino beam or neutrinos in the antineutrinos beam and from electron-neutrinos, mostly because the original pion beam also includes some kaons, which can decay to produce electron-neutrinos as well as from muon interactions. The main difference between accelerator-based neutrino experiments from the other types is that the beam composition is relatively well known. The energy range is higher than for reactor neutrinos even accelerator neutrinos have some contamination. For oscillation experiments, the beam composition is generally measured using a near detector to determine any oscillation component at a far detector.

The advantage of accelerator neutrinos are that the energy range is well known and can be quite well tailored, the flux is huge compared to other methods. However the energy distribution will be quite wide because of the decay processes involved. It is also hard to produce a clean beam without background, muon neutrinos without electron neutrinos. However, for oscillation experiments this can be a good thing, see subsection 2.7. Based on current experimental values these experiments are sensitive for θ_{23} and Δm_{23}^2

2.4.1 Historical experiments

The European Organization for Nuclear Research (CERN) Dortmund Heidelberg Saclay Warsaw (CDHSW) [49] experiment was designed to study neutrino interactions in iron using the CERN SPS neutrino beam line. The experiment consisted of two similar detectors at different distances from the interaction vertex 130 m and 885 m [49]. The detectors were designed to combine the functions of a muon spectrometer and a hadron calorimeter. It consisted of 19 toroidal magnetised iron modules, with an average field of 1.65 T, separated from each other by wire drift chambers and had a mass of 1250 tons. In the end of the experiment a liquid hydrogen tank was placed in front of the experiment to study neutrino interactions in

hydrogen. This is one of the first MINDs (Magnetised Iron Neutrino Detectors).

The CHARM Collaboration (CERN-Hamburg-Amsterdam-Rome-Moscow Collaboration) proposed to study neutrino-nucleon neutral current interaction as well as muon polarisation. It took data from 1978 to 1991 and was comprised of a fine-grained target calorimeter made up of 78 subunits each surrounded by a frame of magnetized iron for muon identification and spectrometry [50].

The CCFR (University of Chicago, Columbia University, Fermilab, and the University of Rochester) detector installed at Fermilab consists of an 18 m long 690 ton neutrino target calorimeter and followed by an iron toroid spectrometer. The calorimeter consists of 168 iron plates, each 3m x 3m x 5.1cm, with liquid scintillation counters spaced between every two plates and drift chambers spaced every four plates. It provided among other things, precision measurements fro neutrino-nucleon scattering [51]. The experiment was continued through the NuTeV experiment which expanded results using the same detector. CCFR took data from 1979 to 1988, NuTeV started in 1996 and continued until 2003.

2.4.2 NOMAD

The Neutrino Oscillation Magnetic Detector (NOMAD) [52], also using the CERN SPS neutrino beam line, searched for $\nu_\mu \rightarrow \nu_\tau$ oscillation by detecting τ appearance. Its goals were to measure the momenta of charged particles and identify and measure electron, photons and muons. By the detector design it was also possible to look for $\nu_\mu \rightarrow \nu_e$ oscillation. Compared to the modular design of CDHS, NOMAD had drift chambers and other sub-detectors contained inside a dipole magnet at 0.4 T.

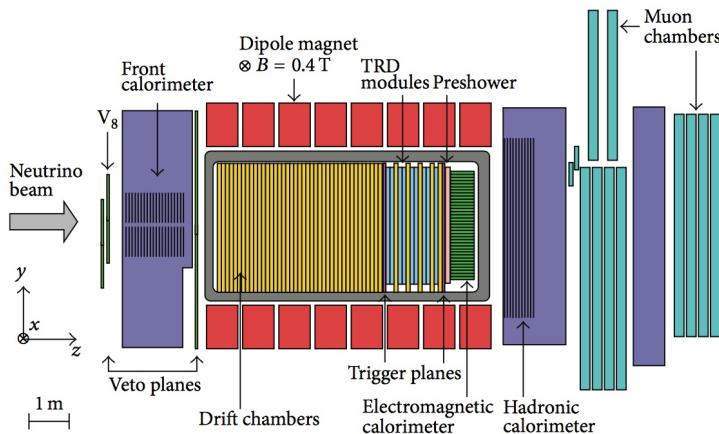


Figure 2.12: A sideview of the NOMAD detector [53].

2.4.3 K2K

After the success of Super-Kamiokande, the The High Energy Accelerator Research Organization (KEK) to Kamiokande (K2K) experiment [54] was created with the main difference of using a well understood muon neutrino beam pointing at the Super-Kamiokande detector at a distance of 250 km. It was the first neutrino oscillation measurement where both the source and detector were controlled, it observed the disappearance of muon neutrinos into tau neutrinos and found results that were consistent with Super-Kamiokande.

K2K, the set up seen in figure 2.13, ran from 1999 to 2004 and used a neutrino beam with a wide spectrum peaked at 1 GeV based on a 12 GeV proton synchrotron beam interacting with an aluminium target and focused through two horns and allowed to decay in a 200 m long decay pipe. This created a 98% pure muon neutrino beam with around 1% contamination of anti muon neutrinos and around 1% electron and anti-electron neutrinos. Understanding the beam composition is required for looking at $\nu_\mu \rightarrow \nu_e$ appearance. To do this a 1-kiloton water Cherenkov near detector, a scaled-down version of Super-Kamiokande, is used to measure the neutrino spectrum which is then extrapolated using Monte Carlos simulated data to provide a neutrino spectrum at Super-Kamiokande detector.

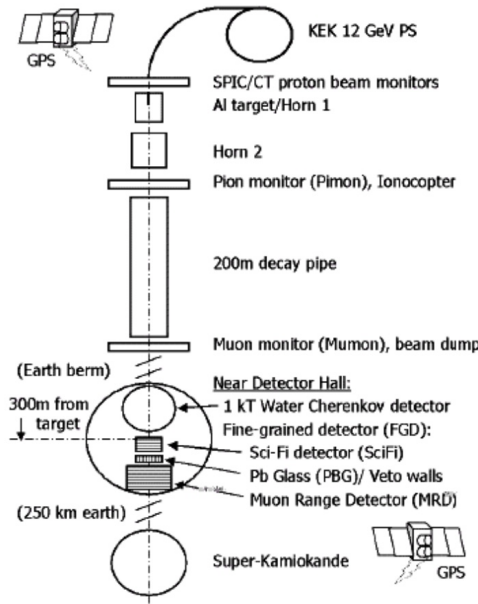


Figure 2.13: A schematic view of the K2K experiment Super-K [55].

2.4.4 MINOS

The Main Injector Neutrino Oscillation Search (MINOS) [56] is a muon neutrino disappearance experiment, consisting of two MINDs, one near (1km from the target) and one far

detector (735km from the target) and using the NuMI [57] beam at Fermilab.

The two detectors have been designed to be as similar as possible to minimize any systematic errors in comparing the observed neutrino spectra in the two detectors. They are both constructed of planes with two magnetised steel plates with a layers of scintillator in-between to measure charged particles and allow discrimination and of charge and measurement of the momentum. The far detector is composed of 486 octagonal plates with a diameter of 8 meters and total length of 30 meters providing a total mass of 5400 tons. The near detector contains only 282 planes, slightly squashed octagonal planes at 3.8 meters \times 4.8 meters. MINOS showed results consistent with Super-Kamiokande and the K2K experiments.

After MINOS the next step using the NuMI [57] beam is the NOvA [58] experiment, which is also an electron neutrino appearance experiment and hopes to be able to determine the mass hierarchy of neutrinos.

The MINERvA (Main INjector ExpeRiment ν -A)experiment [59] will also use the NuMI [57] beam to study neutrino-nucleus scattering to improve models of neutrino-nucleus scattering to reduce systematic uncertainties in results from oscillation experiments.

MiniBooNE[60] continued on what was started by MINOS but had the principle aim on improving neutrino mass measurements.

2.4.5 T2K

After the success of K2K, a similar baseline was constructed with the T2K-experiment [61], a long-baseline neutrino oscillation experiment with a more powerful beam from the JPARC facility at Tokai to Super-Kamiokande, at a distance of 295 km with a near detector at hall 280 meters, in Tokai, from the target, see figure 2.15

The neutrino beam comes from an initial 30 GeV/c proton beam which is passed through a horn fired onto a graphite target. After the target the secondary beam is passed through two magnetic horns and focused into a decay volume before passing the beam stopper. From here there is \approx 180 meters of soil until hitting the near detector hall. This means that the near detector is comprised of only neutrinos with an expected flux as seen in figure 2.14.

The near detector hall contains two main experiments, an on-axis experiment INGRID and the off-axis (2.5^0) ND280 detector both used to reduce model uncertainty and systematic uncertainty in the Super-Kamiokande analysis.

The experiment wanted to improve the understanding of the neutrino oscillation parameters. T2K was able to successfully observe the appearance of muon to electron neutrino oscillations and find evidence that the third mixing angle θ_{13} is not zero. This is still an ongoing experiment.

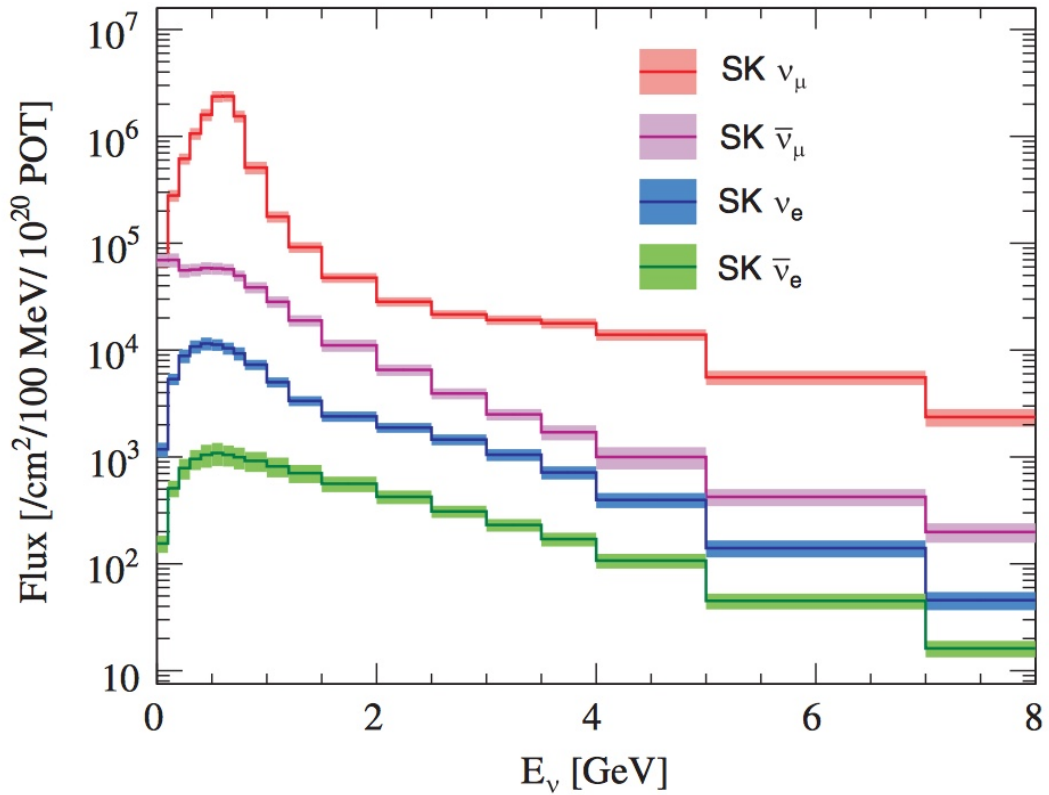


Figure 2.14: Simulated unoscillated expected neutrino fluxes for various flavours with expected systematic before applying near detector data plotted as bands. at Super-K [61].

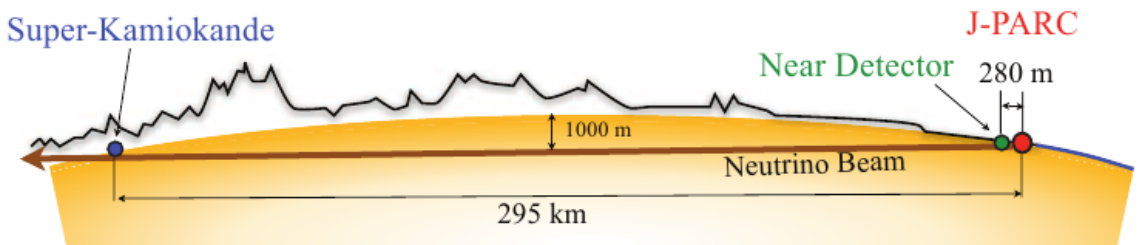


Figure 2.15: A schematic view of the T2K experiment, including the near detector site ND280 and Super-K.

The main source of systematic error for T2K is caused by the difference of the target material and acceptance between the ND280 near detector (hydrocarbon) and the far detector water Cherenkov detector [63] motivating further studies and upgrades to the ND280 detector.

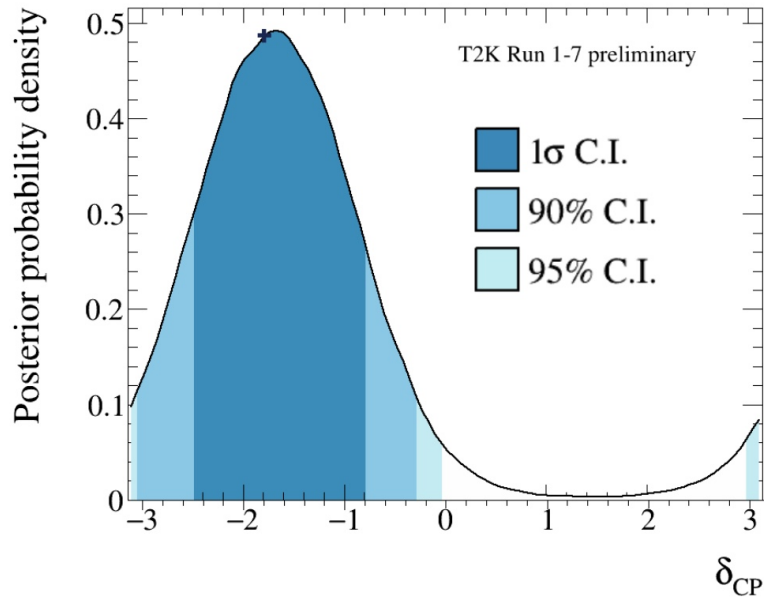


Figure 2.16: Posterior probability density on δ_{CP} , where the cross represent the best-fit [62].

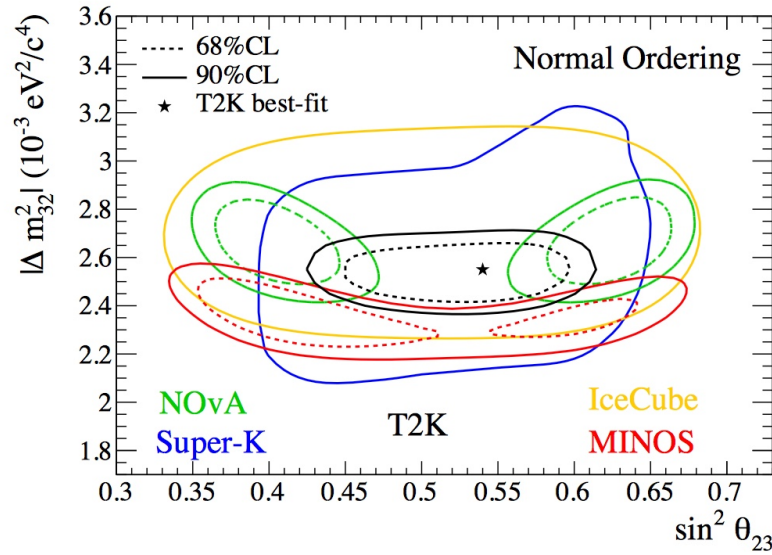


Figure 2.17: The 90% and 68% confidence levels in the $\sin^2 \theta_{23}, \Delta m_{32}^2$ space from T2K compared to other experiments, assuming normal ordering of neutrino masses [62].

2.5 Reactor

Nuclear reactors are very intense sources of low energy neutrinos. Through beta-decay channels electron neutrinos are produced with well known energy spectra and low background. Compared to other neutrino sources the energy range is limited to below $9\text{MeV}/c$, see figure 2.18 as well as a sharp cut of at $1.8\text{MeV}/c$ required for inverse beta decay to occur. The

low energy range means that oscillation experiments can be performed with a short baseline since equation 1.42 provides the same probability by decreasing both the momentum and baseline.

It is also relatively easy to detect as the positron will deposit its kinetic energy in the scintillator and annihilate with an electron and generates two photons. These two photons and the deposited energy cases a so called prompt signal a few nanoseconds after the neutrino event.

The low energy range also means that experiments based on reactor neutrinos can only search for $\bar{\nu}_e$ disappearance since the produced neutrinos do not have enough energy to produce muons or taus and any neutral current interaction will be very difficult to distinguish from background. Based on the current values neutrino reactor experiments are well suited to determine θ_{12} and Δm_{12}^2 as well as θ_{13} and Δm_{13}^2 . Requiring specifically anti-neutrinos, becomes insensitive to δ_{CP} right?

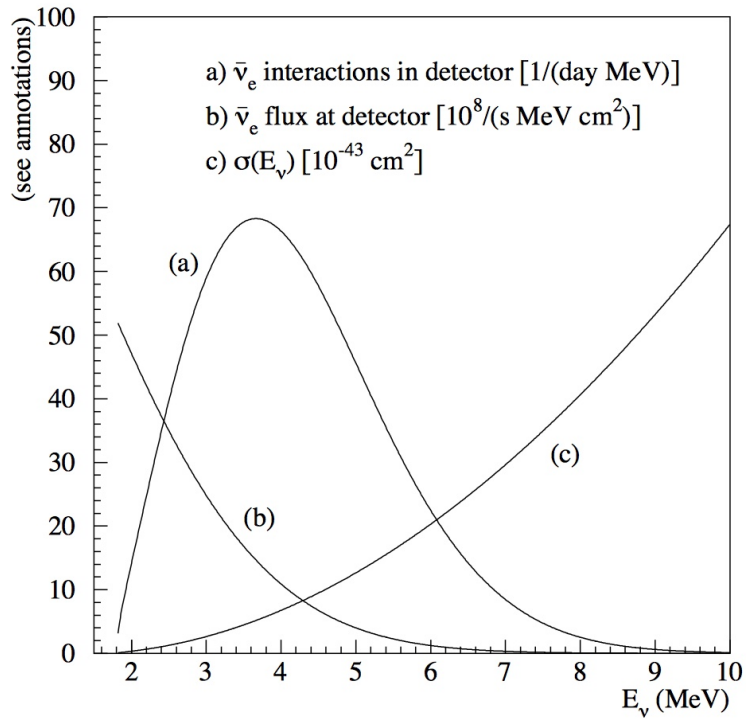


Figure 2.18: Energy spectrum of $\bar{\nu}_e$, the inverse beta decay cross section and interaction spectrum of detected inverse beta decay events [64].

2.5.1 KamLAND

After the completion of the KamiokaNDE experimental run the site used to install the Kamioka Liquid Scintillator Antineutrino Detector (KamLAND) in 2002. KamLAND, seen in figure 2.19, looks specifically for neutrino oscillations by looking at anti electron neutrinos emitted

from distant reactors [65] by using a 1 kton liquid scintillator volume encased by oil. If the neutrinos interact with the volume by inverse beta-decay, it will produce positrons which will annihilate and produce two distinct photon signals, known as prompt signal.

The majority of the neutrino events are from 26 reactors within the distance range of 138-214 km providing a good baseline to see oscillations at the energy spectrum. The spectrum and results can be seen in figure 2.20.

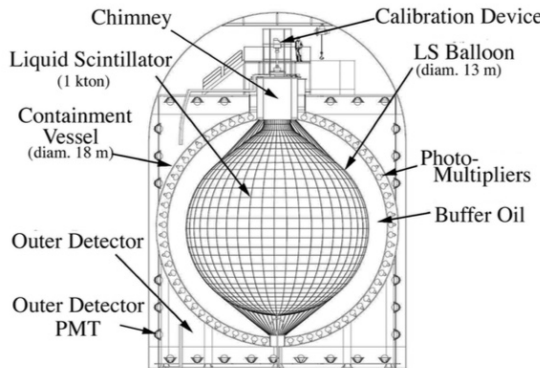


Figure 2.19: Schematic diagram of the KamLAND detector [65].

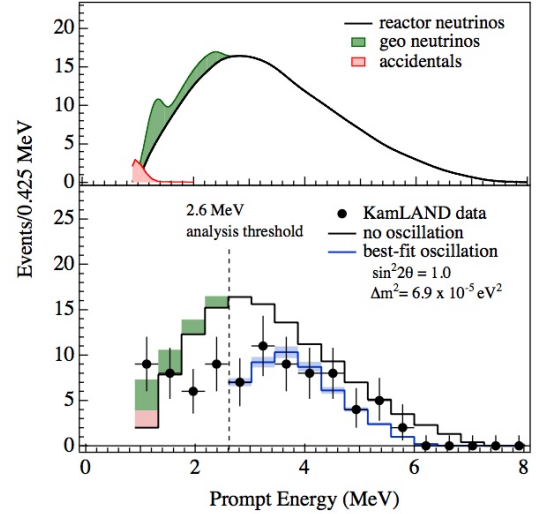


Figure 2.20: Top panel: Expected reactor $\bar{\nu}_e$ energy spectrum. Lower panel: Energy spectrum of the observed events along with the no oscillation spectrum and best fit spectrum.

2.5.2 Double Chooz

The Double Chooz experiment [66] started in 2004, used anti-neutrinos produced two nuclear cores from a nuclear power station to measure the neutrino mixing angle θ_{13} as well as showed that these detectors can be used to ensure non-proliferation [66, 67]. The experiment consisted of two liquid scintillator detectors at a distance of 280m and 1050m both consisted of PMTs inside a scintillating volume shielded from cosmic radiation.

2.5.3 RENO

The Reactor Experiment for Neutrino Oscillation (RENO), started taking data in 2011 and was the first experiment to use two identical detectors placed at a near and far site. The

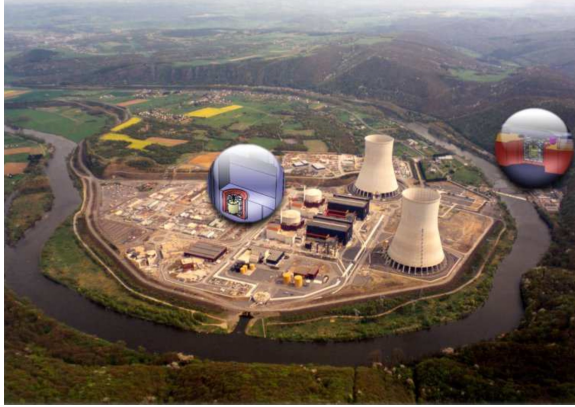


Figure 2.21: Overview of the Double Chooz experimental site [66].

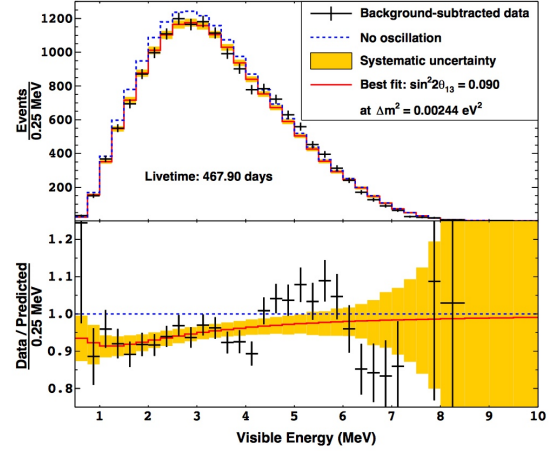


Figure 2.22: Top panel: Measured energy spectrum with data on best fit and no oscillation models. Lower panel: Ratio of data over no-oscillation prediction [68].

detectors are liquid scintillator detectors with 16.5 tons of Gadolinium doped scintillator. It measures neutrinos generated by six nuclear reactors each spread out perpendicular from a base line setting the detectors at 294 m and 1383 m from the center of the base line, see figure 2.23. Reno measured $|\Delta m_{32}^2| = 2.61 \pm 0.16 \pm 0.09 \times 10^{-3} \text{ eV}^2$ and $\sin^2(2\theta_{13}) = 0.086 \pm 0.006 \pm 0.005$ using the data in figure 2.24.



Figure 2.23: Layout of the RENO detectors, yellow and reactors in red. The six reactors are equally spaced in a 1280 m span [69].

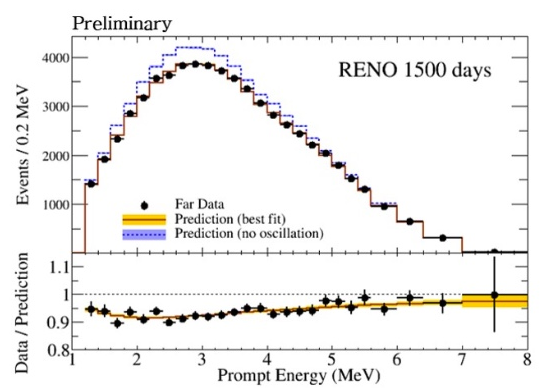


Figure 2.24: Top panel: Measured energy spectrum with data on best fit and no oscillation models. Lower panel: Ratio of data over no-oscillation prediction [69].

2.5.4 Daya Bay

The Daya Bay experiments [70] main goal is to improve the measurement of θ_{13} . It is improving results from Double Chooz by utilizing eight identical detectors placed at three locations around the Daya Bay area consisting of a total of 6 different nuclear cores. This layout allows for maximum sensitivity and the ability to reduce systematic uncertainties due to uncertainties in reactor power levels. It also allows for cross-calibration of the detectors since they are all identical. Each detector is a segmented Gadolinium doped liquid scintillator detector using PMTs to read out photons produced through inverse beta-decay and annihilation. The experiment has been taking data since 2011.



Figure 2.25: Layout of the Daya Bay experiment [70].

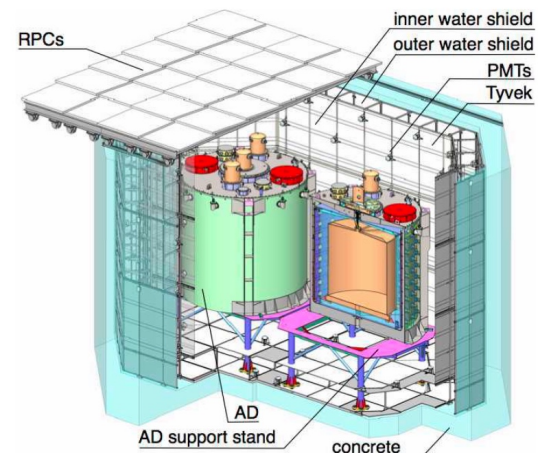


Figure 2.26: Near site layout of the Daya Bay detector with surrounding structure [71].

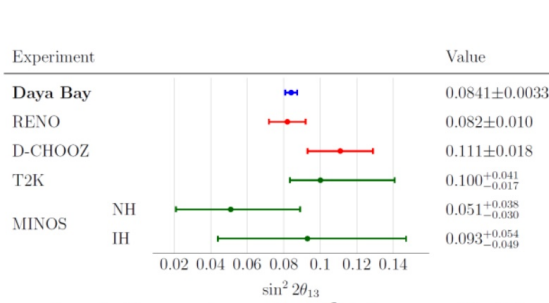


Figure 2.27: Comparison of $\sin^2 2\theta_{13}$ measurements from various experiments, taken from [71].

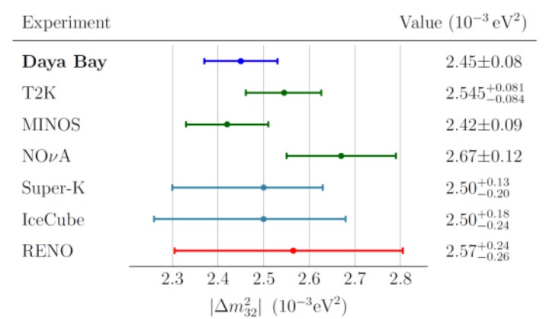


Figure 2.28: Comparison of $|\Delta m^2_{32}|$ measurements from various experiments, taken from [71].

2.5.5 JUNO

The Jiangmen Underground Neutrino Observatory (JUNO) [72] is a 20 kton liquid scintillator detector currently under construction and aiming to start data taking in 2020, seen in both figure 2.29 and figure 2.30. It has as one of its primary aims to determine the mass hierarchy, sign of the mass splitting, using reactor neutrinos and inverse beta-decay with an improved energy resolution compared to previous experiments [72]. It uses the Daya Bay reactor as a far reactor and results from the Daya Bay experiment to reduce systematic errors from the reactor.



Figure 2.29: Location of the JUNO site with distances to the near by reactors, Yangjiang and Taishan at both 53km as well as Daya Bay at 215km away. [72].

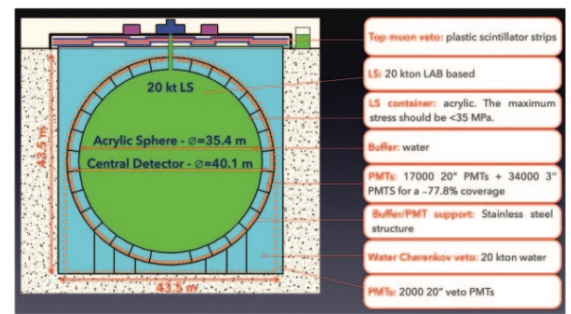


Figure 2.30: Schematic view of the JUNO detector [72].

2.6 Future neutrino oscillation experiments

2.6.1 DUNE

LBNF/DUNE[73], seen in figure 2.32, is a new experiment currently under construction aiming at looking at the full range of δ_{CP} with greater sensitivity than before by improving on the MINOS [56] experiment, and performing an electron neutrino appearance measurement with a high-powered neutrino beam from Fermilab and a 40 kton liquid argon detector at a distance of 1300 km, in the Homestake mine in South Dakota with a full initial physics study presented in [74]

The main goals are to perform precision measurements of neutrino oscillation to determine δ_{CP} within 5σ , determining the neutrino mass ordering, seen in figure 2.31, and measuring the sign of the mixing angle θ_{23} all to within new limits.

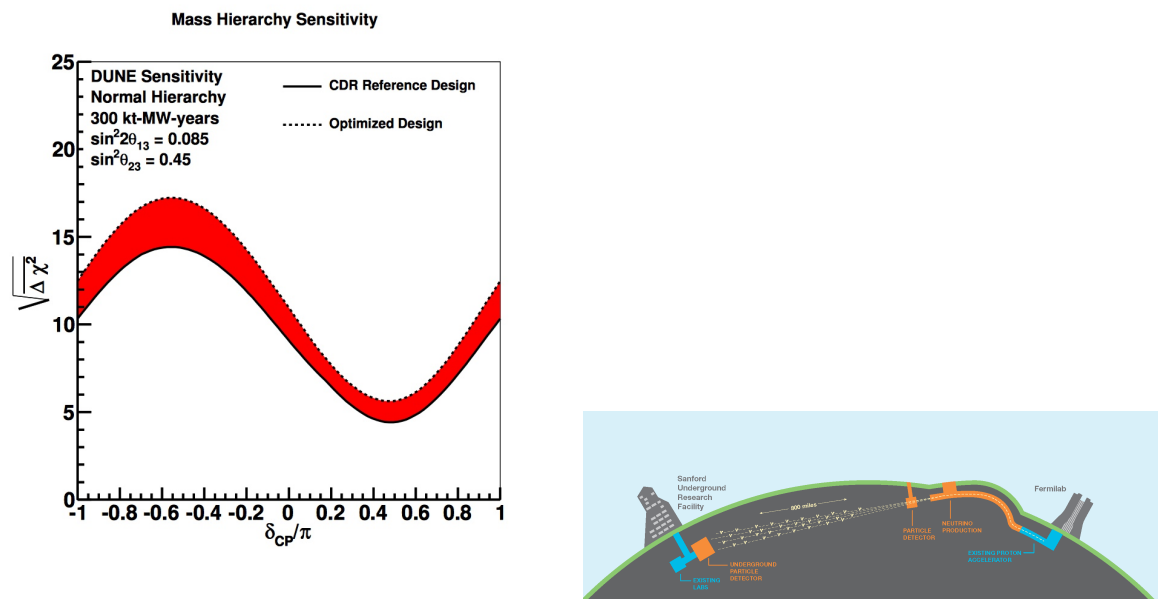


Figure 2.31: Estimated significance of the mass hierarchy discrimination metric as a function of values for δ_{CP} [73].

Figure 2.32: Schematic view of the DUNE detectors [73].

2.6.2 Hyper-K

The Hyper-Kamiokande Experiment (Hyper-K) [75] builds on the T2K-experiment [61] by improving the neutrino beam at JPARC, and expanding the water Cherenkov detector by a factor of 10 to a fiducial volume of 500 ktons, which aims to improve the sensitivity for δ_{CP} and determine the value within $> 3\sigma$, and $< 18^\circ$ and determine the mass hierarchy within $> 3\sigma$ and the sign of θ_{23} with a $> 90\%$ confidence level.

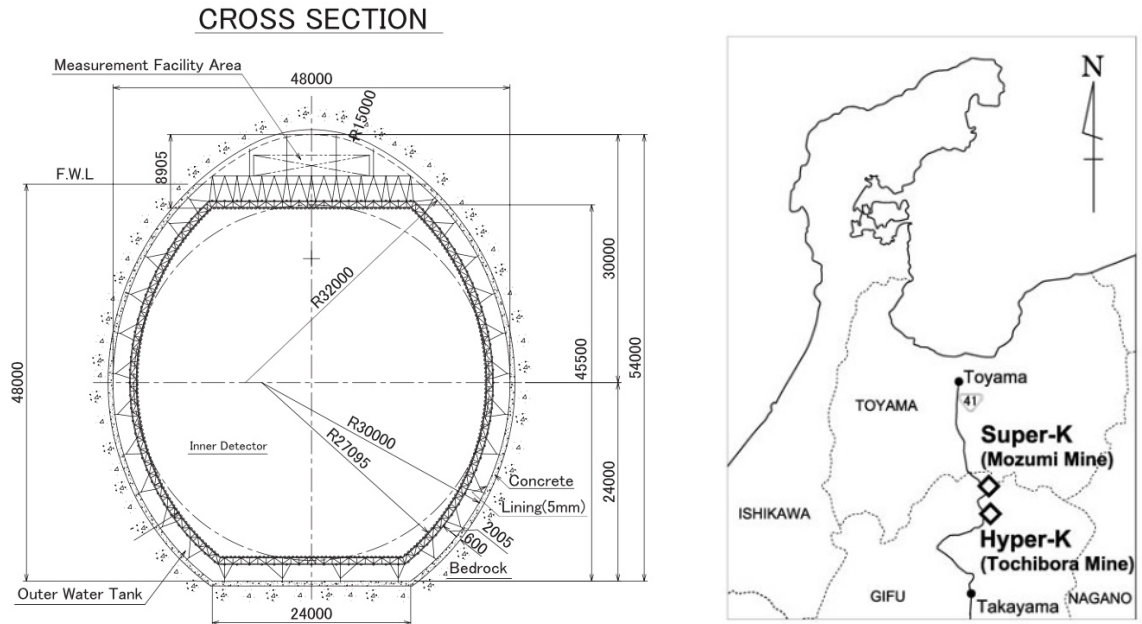


Figure 2.33: Cross section view of the Hyper-Kamiokande detector [75].

Figure 2.34: A map showing the proposed candidate site [75].

2.7 Neutrino Factory

The Neutrino Factory (NuFACT) is a novel concept for a neutrino accelerator which will produce a high intensity (1000 higher than previously attained) and a high energy beam (up to 15 GeV [76]). Compared to other previous experiments it will produce a two flavour, electron and muon, neutrino beam through a muon decay ring. The neutrino factory has the capacity to improve the precision of neutrino oscillation measurements, since the neutrino beam from the decay of muons can be determined with high accuracy. The beam produces one bunch of μ^+ and one bunch of μ^- , so the facility can make measurements of ν_μ and $\bar{\nu}_e$ and $\bar{\nu}_\mu$ and ν_e simultaneously. Using this δ_{CP} can be decisively explored, with an expected accuracy of $\Delta\delta_{CP} \sim 5^\circ$ [77]. A schematic of the facility is shown in figure 2.35 showing the full accelerator chain. The full chain, starts by producing muons and pions from a proton beam on target. Pions are then captured in a strong solenoid magnetic field surrounding the target. The bunches are sent through the so called front end containing a phase rotation and a ionisation cooling channel before being re-accelerated and entering the muon storage ring. Before entering the ring the muons are charge separated and go into the storage ring in counter-rotating directions. After ≈ 70 turns of the circuit the muons decay through the following modes with the branching ratio:

$$\mu^- \rightarrow e^- + \bar{\nu}_e + \nu_\mu, \approx 100\% \quad (2.4)$$

$$\mu^- \rightarrow e^- + \bar{\nu}_e + \nu_\mu + \gamma, < 1\% \quad (2.5)$$

$$\mu^- \rightarrow e^- + \bar{\nu}_e + \nu_\mu + e^+ + e^-, < 1\% \quad (2.6)$$

From the branching ratio the energy spectrum and composition of the neutrino beam is well known as the decays only produces two different neutrino flavours. It is important to note that a $\mu^+\mu^-$ beam will produce $\bar{\nu}_\mu + \nu_e / \nu_\mu + \bar{\nu}_e$. Thus for a μ^- beam any electron neutrinos or anti-muon neutrinos discovered must have been produced through oscillation. To be able to distinguish muons from anti-muons at a detector, a magnetic field is required motivating the design of any considered detector, described in subsection 2.8. Currently there are proposals for NuFACT to be constructed at CERN [77], ESS [78] and FERMILAB [79], where it is also seen as a step toward a full muon collider experiment.

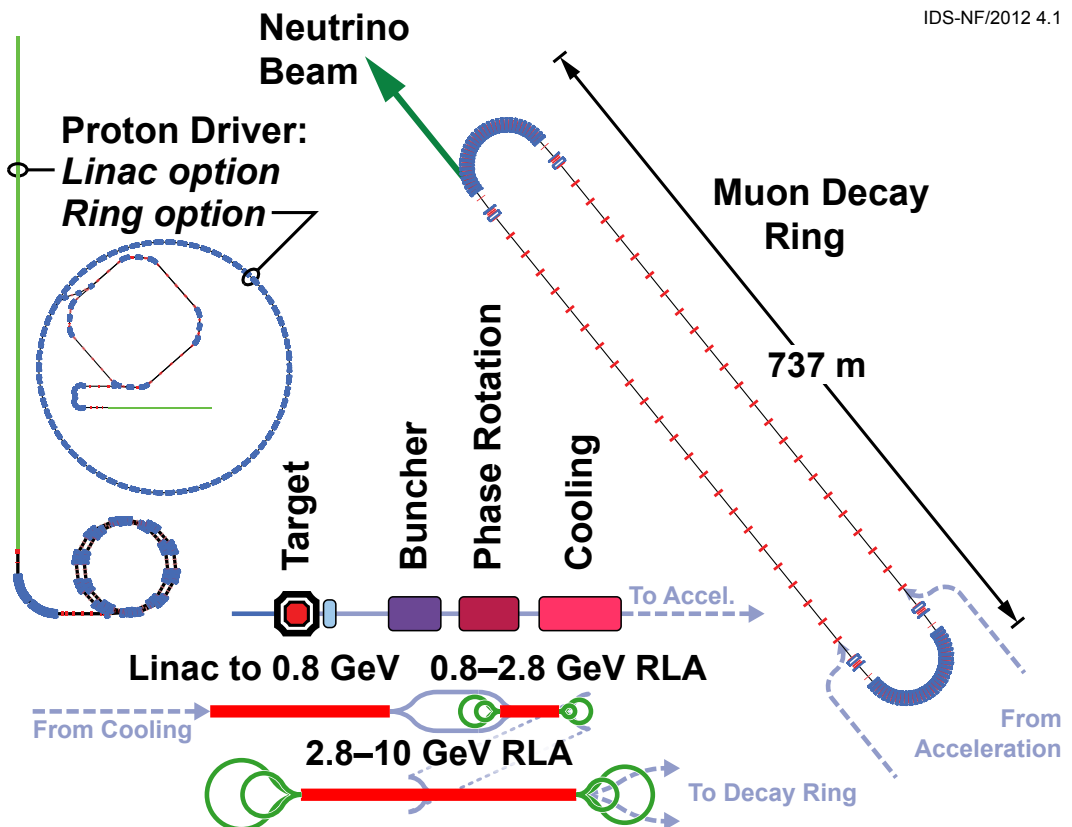


Figure 2.35: Schematic diagram of the Neutrino Factory [76].

2.7.1 NuSTORM

The Neutrino Factory is a complex and expensive facility which requires new technology to be realised. To overcome this a staged approach has been suggested, where each stage would

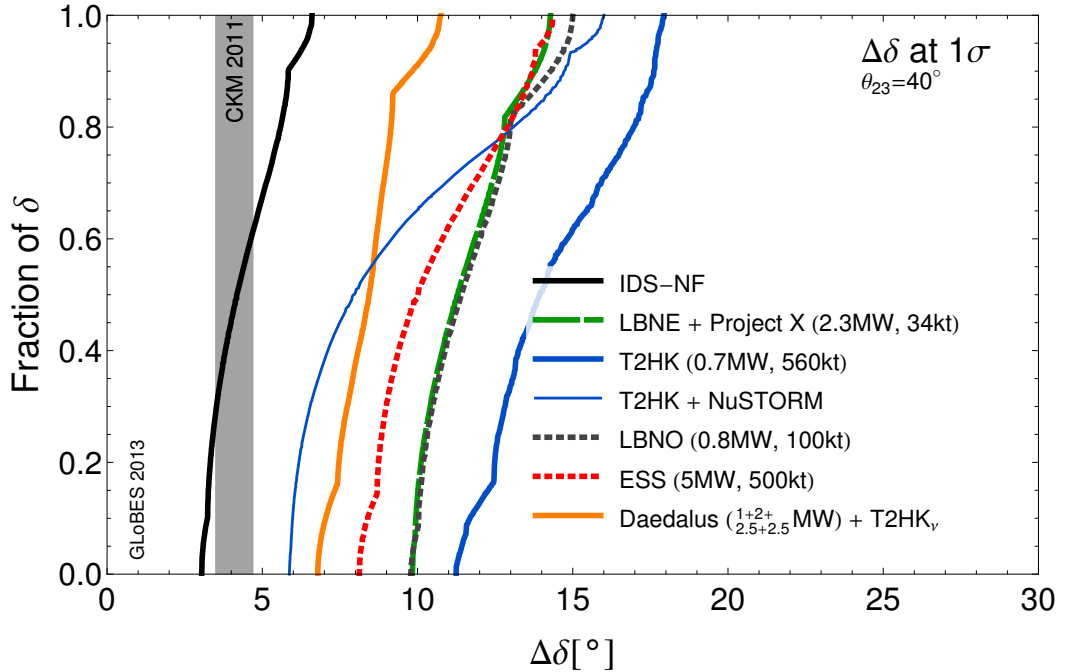


Figure 2.36: Expected precision for a measurement of the δ_{cp} at a Neutrino Factory compared to alternate neutrino oscillation facilities [76].

be delivering physics [76]. The first stage in this plan is named NuSTORM (Neutrinos from Stored Muons) with a schematic shown in figure 2.37. The NuSTORM beam is designed to produce 3.8 GeV/c muons which are injected into a muon storage ring. Compared to the full neutrino factory, NuSTORM is expected to have some pions and kaons for the first pass in the storage ring providing some contamination in the final beam producing both neutrinos and anti-neutrinos for both muon and anti-muon modes and thus a near detector is required to measure the flux of both.

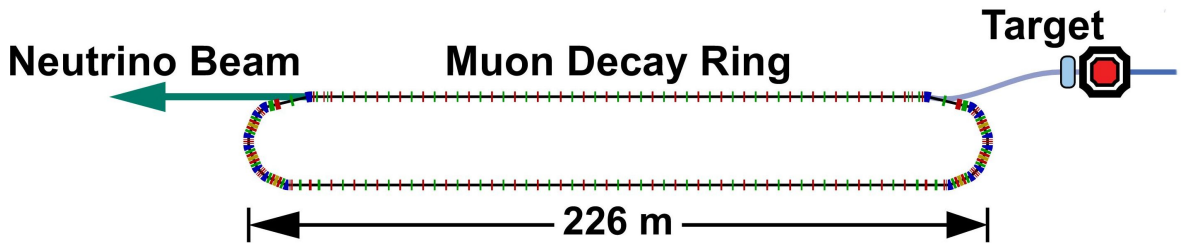


Figure 2.37: A schematic of a NuSTORM facility [76].

For the both NuFACT and NuSTORM [80] the detector type proposed will be a MIND type, similar to the ones used in CDHSW and MINOS [81].

2.8 Magnetized Iron Neutrino Detectors

Magnetized Iron Neutrino Detectors (MINDs) have been operated in several experiments such as CDHSW [49] and MINOS [56]. This type of detector, with magnetized steel plates and scintillation plates, is well suited to provide large mass for neutrino experiments and is able to provide momentum measurements by using range and curvature calculations as well as providing charge identification. A MIND type detector has been selected as the baseline detector for a neutrino factory [82, 83], since it is the cheapest and most effective way of producing a large magnetized volume. This has provided the motivation for creating a prototype detector to perform a number of studies.

Since water Cherenkov and liquid argon detectors have been established or are actively studied for future very large scale neutrino oscillation experiments, a MIND type detector is not foreseen to be used as the main interaction medium for any planned upcoming experiments.. A MIND type detector can however be used to provide charge identification of muons if positioned downstream of any neutrino target which is not magnetized.

2.9 Summary

In this chapter the some history of neutrino experiments have been presented and context given for the Baby MIND experiment.

Chapter 3

Baby MIND + WAGASCI

3.1 Baby MIND/NP05

The prototype Magnetized Iron Neutrino Detector (Baby MIND) [84] was designed with the aim to study muon charge identification efficiencies in order to get estimates for a future Neutrino Factory, discussed in this section. The Baby MIND project was launched as a prototyping activity within the European Commission-funded AIDA-2020 project. The particle charge is essential for their oscillation measurements since wrong-sign muons are the neutrino oscillation signal. During the design process a secondary aim was added, to measure the momentum and charge of muons from neutrino interactions in water and hydro-carbon targets at the J-PARC T59 WAter-Grid-SCItilator-detector (WAGASCI) experiment, further discussed in section 3.2

The Baby MIND collaboration is comprised of around 46 scientists from 10 different institutions, and is part of the CERN Neutrino Platform as experiment NP05 [85] and is as of 2018 fully integrated into WAGASCI and in turn T2K.

3.1.1 Motivation

The Baby MIND aims to show that MIND type detectors are viable to use for muon charge identification at low momenta ($< 1\text{GeV}/c$) and also to show how well the charge can be identified from a Neutrino Factory [77] beam. A secondary motivation is to act as a platform to test new electronics, scintillation fibres and data acquisition for future experiments. Additionally the experiment aims to compare simulations from GEANT4 [86] to data taken from the detector to be able to verify the properties of muon interactions at momentum ranges of 0.5 to 10 GeV/c. Separating and identifying particles of different charges requires a magnetic field, and to perform identification at low momenta a high uniform field has to be created in

a large volume and preferably without fully stopping the particles which are being identified. The main difficulty that arises is to magnetise the volume in an inexpensive and simple manner.

In essence one has to balance having a large magnetized volume over for instance gas, which will not stop particles but it will not be strong/cheap/large or uniform over the other option of magnetising a large iron block which is cheap and uniform but stops particles.

For the Baby MIND a novel approach was chosen to use thin high quality magnetised ARMCO steel plates in an arrangement to optimize charge identification while minimizing the amount of steel plates interspersed with scintillator modules. The optimal design has been slightly shifted due to limiting constraints such as construction time, size of the ND280 shaft [61] and design costs. An added advantage of this approach is the addition of a fully modular design leading to the Baby MIND being able to be set in any configuration with an appropriate support frame. The use of magnetised steel modules instead of requiring the use of an all encompassing magnet, simplifies the magnetic design, lowers the cost and allows for a more uniform field. The direct disadvantages of this is the momentum resolution which is limited by multiple Coulomb scattering and difficulty of performing track reconstruction, discussed further in section 4.6.

The CERN Neutrino Platform approved Baby MIND as experiment NP05 in December 2015 and construction started in August 2016 and finished in June 2017.

During the development of the detector it was proposed to use Baby MIND as a muon spectrometer downstream of the WAGASCI experiment (T59) at J-PARC, using neutrinos from the T2K beamline, to provide charge and momentum of outgoing muons from neutrino charged current interactions. Baby MIND was installed in the ND280 pit at J-PARC in early 2018.

3.1.2 Magnet modules

The magnetised volume for the Baby MIND has been chosen as a total of 33 steel modules both to have a simple magnetic field as well as being modular and cheaper than the alternatives. An overview of the magnetic field is seen in figure 3.1 with two open slots in order to cover the entire plate with coils with currents in opposite directions. This improves the flux return, contains the stray fields and reduces power dissipation outside of the plates compared to a single conducting coil wound on the surface of each individual plate. Each module consists of ARMCO steel with two slits to allow aluminium coils to be wrapped around the steel (25 turns) and two side caps to allow for the magnetic flux return. The field is split into 3 parts where the field is 1.5 T but with opposite orientation as can be seen in figure 3.1. Because of this simple design, the field lines are contained in the steel and have negligible

stray fields of less than 15 mT, with a good uniformity in the area of interest (seen as red in the figure 3.1). This provides a bending direction either up or down depending where the particle passes and its charge. The magnet module dimensions are $3500 \times 2000 \times 30$ mm 3 , with the field oriented along the x direction (right) and bending with respect to the bend in z axis (into the figure). Simulations show the magnet field map to be very uniform over this central tracking region covering an area of 2800×2000 mm 2 , where the field component in the x direction dominates with respect to the field in the other orthogonal directions. The magnet modules were constructed at CERN through the CERN Neutrino Platform [87].

Test results on the 33 modules show all to achieve the required field of 1.5 T for a current of 140 A, with a total power consumption of 11.5 kW.

3.1.3 Scintillator modules

In the Baby MIND, particle hits are detected by scintillating bars which provide both horizontal and vertical position information. There are a total of 18 scintillator modules, where each scintillator module is constructed from 95 horizontal bars for each of the two horizontal planes, $3000 \times 31 \times 7.5$ mm 3 , and 16 vertical bars, $1950 \times 210 \times 7.5$ mm 3 for two planes of vertical bars each providing a total size of the scintillator module as $3000 \times 1950 \times 30$ mm 3 . Since the vertical information is important for curvature, smaller bars are used to provide a better position resolution. The bars are arranged in 4 planes, of horizontal, vertical, vertical, horizontal, with an overlap between planes to achieve close to 100% hit efficiency for minimum ionizing muons [88]. INR Moscow built and designed the scintillator bars, providing a good light yield, figure 3.2 3.3, regardless of where the bar is hit. The bars are polystyrene based, 1.5%PTP, 0.01% POPOP and held together mechanically within an aluminium support frame. The bars contain Kuraray WLS fibers (200 ppm, S-type, diameter 1.0 mm) and contain a reflective coating 30 to 100 μ m from chemical etching of the surface. The connectors are custom made using Eljen EJ-500 optical cement. A schematic view of the horizontal bars can be seen in figure 3.2 and the vertical bars in figure 3.3.

3.1.4 Layout

Design constraints came from the need the need for Baby MIND to operate at both CERN and J-PARC on a relatively short time scale. The installation at J-PARC has driven the overall design with the requirement to lower segments of detector elements through a narrow shaft down to the lowest floor of the ND280 building pit at J-PARC. The magnetisation scheme for the Baby MIND developed within the CERN Neutrino Platform framework is a direct result of this constraint.

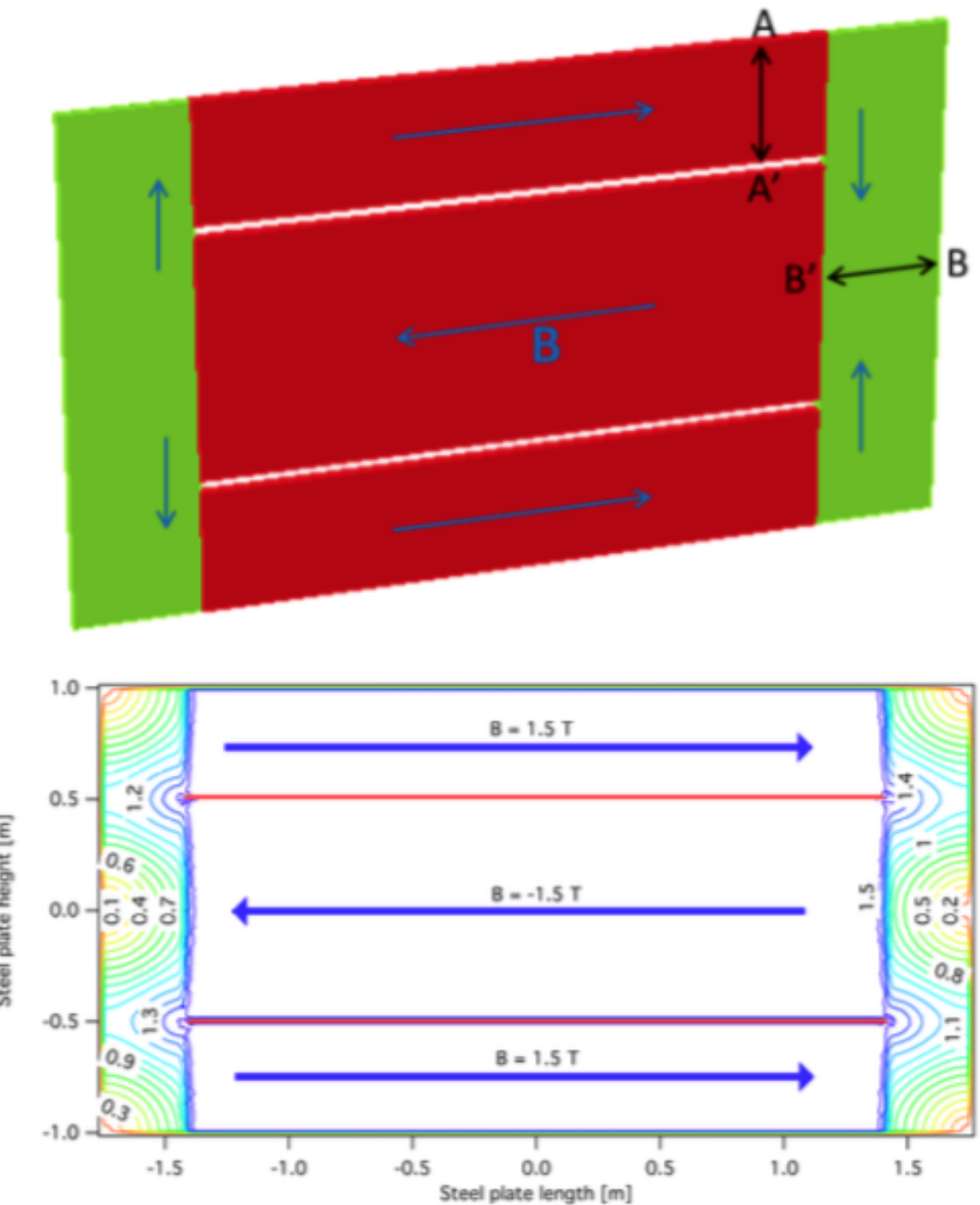


Figure 3.1: (Top) Schematic view of the magnet module. (Bottom) A contour plot of the magnet module, with the fiducial areas of interest showing magnetic field uniformity.

Previous magnetised iron detector, discussed in chapter 2, have been in the kiloton range, Baby MIND is comparatively small weighing only 65 t. A schematic overview of the detector can be seen in figure 3.4, showing the full detector composed of 18 scintillator modules, and 33 magnetised ARMCO steel plates, referred to as magnet modules. The full detector is around 4 meters in length with a height of around 2 meters and width of 3.5 meters. The chosen layout of the detector for the test beam is divided into four blocks with first

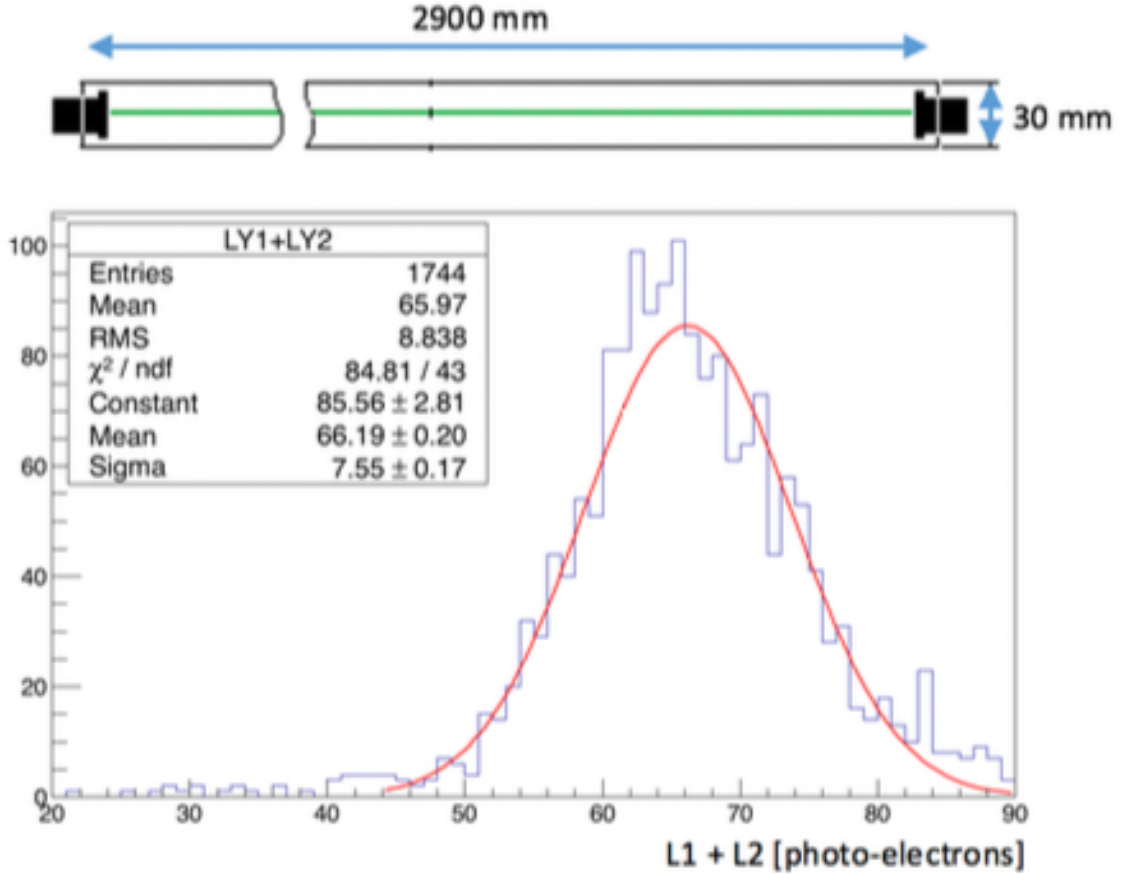


Figure 3.2: Schematic view of the horizontal bar and light yield curves.

block, block 1, containing 3 sub-blocks and the last block, block 4, containing 2 sub-blocks. The gaps between sub-blocks in block 1 have been added to improve the low momentum reconstruction using a lever-arm approach, discussed further in section 4.6.

3.1.5 Electronics

The scintillating fibres, present in the bars are read out using Hamamatsu MPPC (Multi Pixel Photon Counters). Compared to PMTs these use a lower voltage, less current and are compatible with magnetic fields. This provides a small size, and simple electronics for the modules. The MPPCs are custom made S12571-025C (and derived S10943-5796), a size of $1 \times 1 \text{ mm}^2$ (65% fill factor) and 25 m cell size. The operating voltage is ≈ 67.5 V with photon detection efficiency (PDE) 35%, gain 5×10^5 and dark counts of typically 100 kcps. The MPPC signals, sampled at 400 MHz, are powered (HV/LV) and read out by custom made Front End Boards (FEBs), seen in figure 3.5, designed for 96 channels using CITIROC ASICs [89]. The MPPC signals are connected through a 5 m extension coaxial cable bundle containing up to 32 photosensors signals. The purpose is to decouple

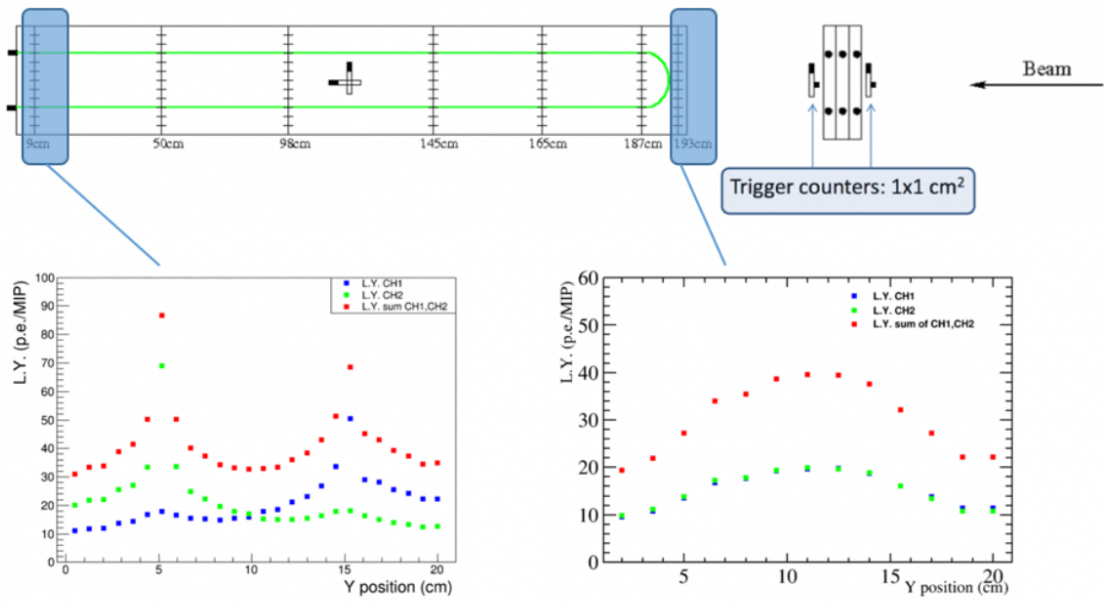


Figure 3.3: Schematic view of the vertical bar and light yield curves performed for hits at the near and far end of the bar.

d: scintillator detector module

a: ARMCO steel module

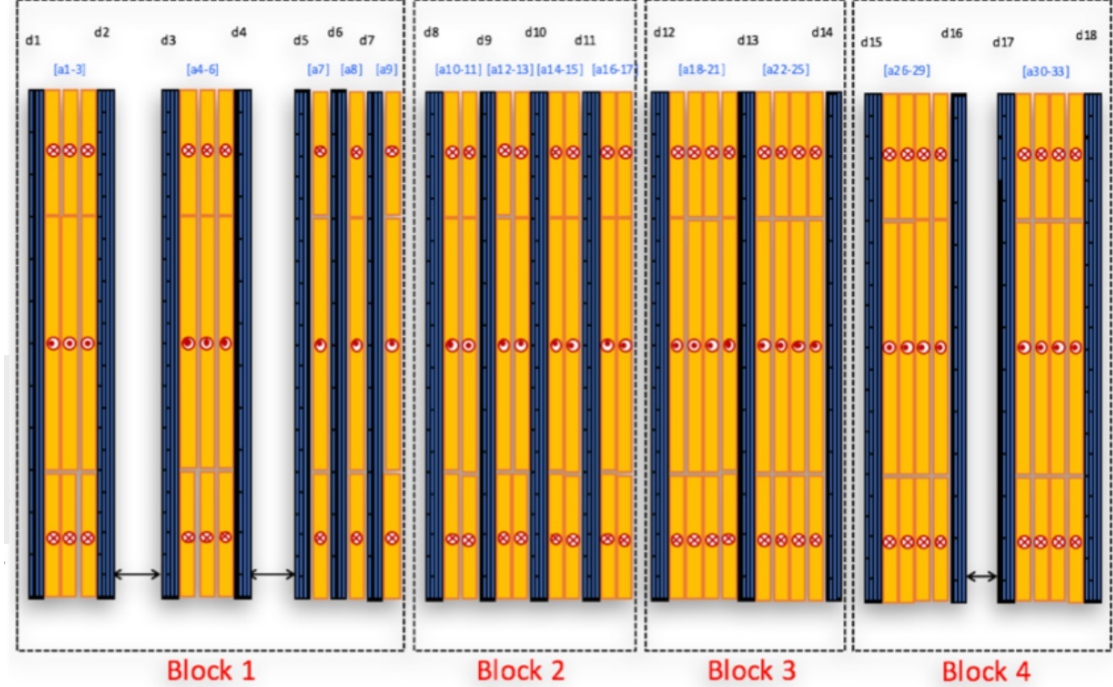


Figure 3.4: The test beam Baby MIND design, in yellow the magnet modules and in blue the scintillator modules.

the FEBs from the scintillator modules, which improves accessibility to FEBs and their long

term maintainability. These rack mounted FEBs have been designed by Geneva University containing 3×32 channel connectors, 3 CITIROC ASICs with 32 channels each. The FEBs are installed in mini-crates which can connect up to 7 FEBs via readout/slow control on USB3 and/or Gigabit using a backplane seen in figure 3.6. Data is sent from the mini-crates to DAQ computers via USB3 and passed on to a final computer located in a control room. The full readout chain can be seen in the block diagram in figure 3.7.

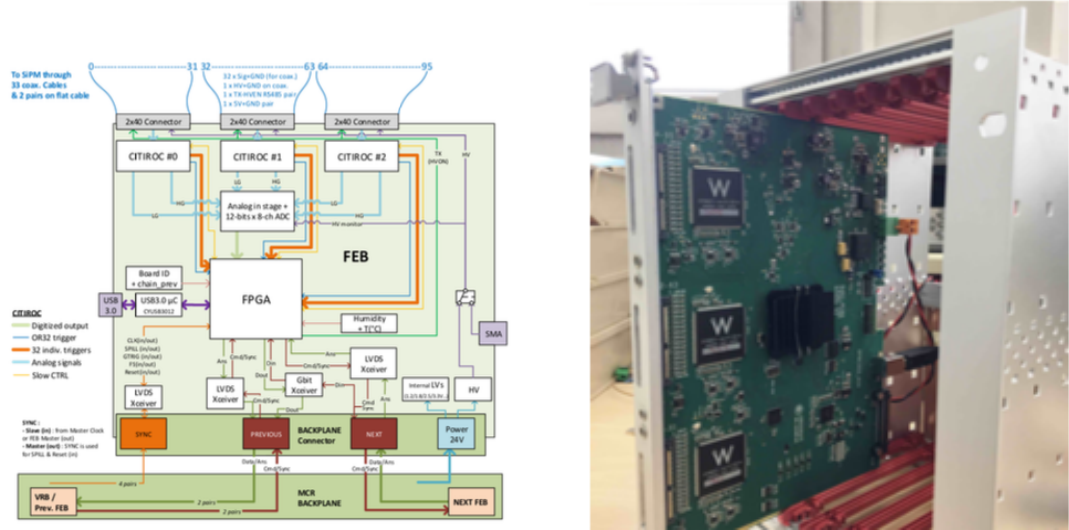


Figure 3.5: (Left) Schematic view of FEB layout. (Right) An image of the FEB in one of the racks.

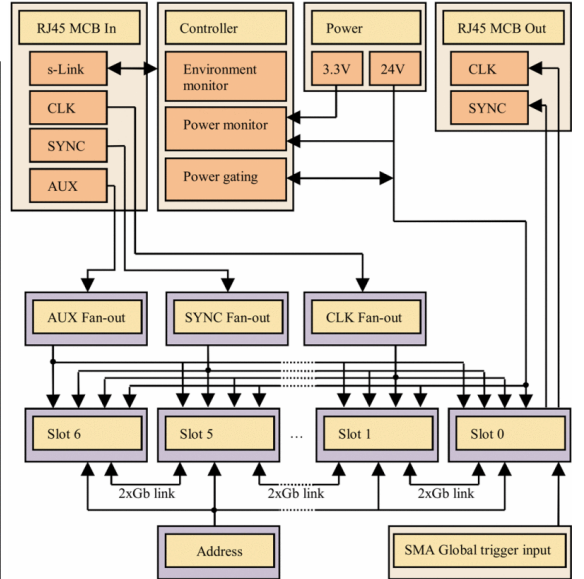
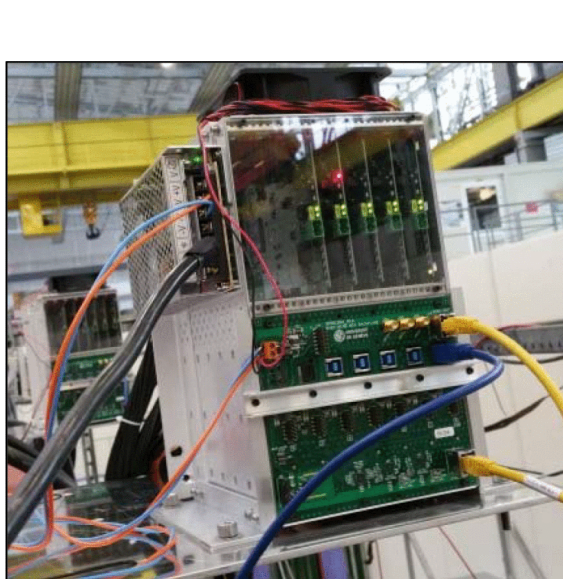


Figure 3.6: (Left) Front end electronics mini-crate installed on the detector. (Right) Block diagram representing the backplane. Figures from [90]

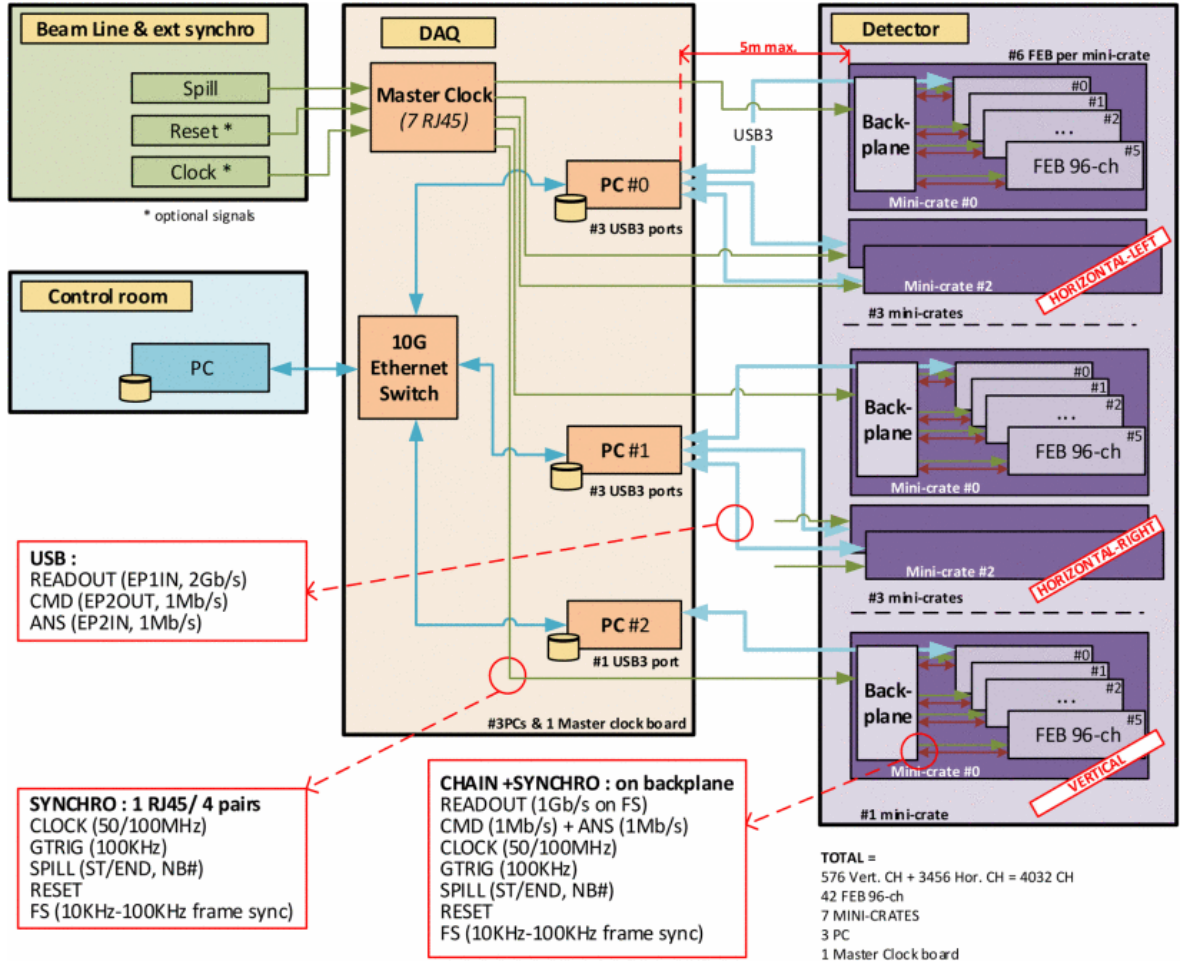


Figure 3.7: Readout block for the Baby MIND. Figure from [90]

3.1.6 Construction and test beam

The CERN Neutrino Platform approved Baby MIND as experiment NP05 in December 2015 and construction started in August 2016 and finished in June 2017. During the development of the detector it was proposed to use Baby MIND as a muon spectrometer downstream of the WAGASCI experiment (T59) at J-PARC, using neutrinos from the T2K beamline, to provide charge and momentum of outgoing muons from neutrino charged current interactions. The installation and commissioning of the detector in J-PARC will take place in the beginning of 2018, with commissioning in the summer and started to take beam at J-PARC in October 2018.

3.2 WAGASCI/T59

The new WAter-Grid-SCIintilator-detector (WAGASCI) at the J-PARC neutrino beam line will measure the difference in cross sections from neutrinos interacting with a water and scintillator targets, in order to constrain neutrino cross sections in oxygen and carbon, essential for the T2K neutrino oscillation measurements. It follows a similar approach to the one used for iron scintillator cross-sections in the INGRID detector [61].

Baby MIND will act as a magnetic spectrometer behind the main WAGASCI target. Baby MIND was installed behind the WAGASCI at J-PARC in the beginning of 2018 to measure the charge and momentum of the outgoing muon from neutrino charged current interactions, to enable full neutrino event reconstruction in WAGASCI.

3.2.1 Motivation

The WAGASCI experiment (T-59) at J-PARC on the T2K beamline aims to improve measurements of the ratio of neutrino interaction cross-sections on water and carbon. This is required to reduce systematics due to nuclear effects in water, currently the dominant systematic uncertainty in the T2K neutrino oscillation analyses [61]. With planned upgrades to the T2K and a planned follow-up project HyperK [75], there is a strong motivation to reduce the systematic uncertainties. The aim is for T2K to improve the level of systematic precision to 4%.

WAGASCI proposes to test a new 3-D grid-type detector, composed of plastic scintillator and water, to improve on the current understanding of nuclear effects in neutrino interactions. The WAGASCI collaboration states that the detector will be able to measure this cross-section to a level of 3% systematic uncertainties in the $1 \text{ GeV}/c$ energy region with a generic MIND [91]. Using WAGASCI as a near detector, in the ND280 building, combined with the far Cherenkov detector provides knowledge of the ratio of neutrino interaction cross-sections in water and plastic scintillator. Due to the design of the WAGASCI being both small and not including any magnets, it is impossible to reconstruct charge or momentum for incoming particles. By including the Baby MIND to provide reconstruction downstream, this obstacle is overcome. The size of the Baby MIND is particularly well suited for the WAGASCI experiment providing excellent acceptance for forward secondaries from interactions in the upstream WAGASCI water and carbon targets. During operation with the WAGASCI experiment, Baby MIND is referred to as the Muon Range Detector (MRD). The layout can be seen in figure 3.8.

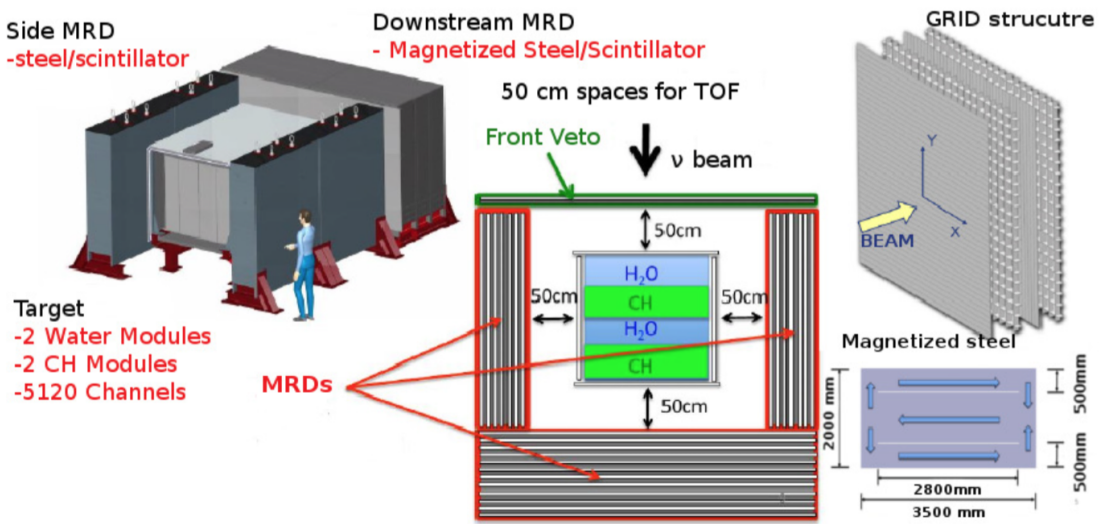


Figure 3.8: The basic structure of the WAGASCI detector including one of the possible designs for the MIND plates. The MIND detector is denoted as Downstream MRD [91].

3.2.2 Layout

There are two main elements of the WAGASCI, the central part is a neutrino interaction target which contains water and hydrocarbon, the target is surrounded by muon range detectors (MRDs). The target it self has scintillator bars in different orientation. The current layout is horizontally stacked bars, 3D grid, vertically stacked bars, 3D grid repeated twice providing a total of 8 planes. The 3D grid, seen in figure 3.9, is made of thin scintillator bars of $1000 \times 25 \times 3 \text{ mm}^3$ put together to form a grid with small pieces cut out to form a full grid, seen in figure 3.10. The 3D structure is currently submerged in water to provide the water in which to study neutrino interactions. This design maximizes the fraction of the target material and also provides good particle tracking capabilities allowing to reconstruct tracks emerging at large angles w.r.t. neutrino beam direction. The WAGASCI detector will collect data with both polarities of T2K focusing horn system. The WAGASCI modules are mainly composed of 1280 plastic scintillator bars and a surrounding stainless steel tank. One WAGASCI module consists of 16 scintillator tracking planes, where each plane is an array of 80 scintillator bars fixed within a frame. The 40 bars, called parallel scintillators, are placed perpendicularly to the beam, and the other 40 bars, called lattice scintillators, are placed in parallel to the beam with hollow cuboid lattice.

WAGASCI has the possibility of being operated both with water-in and water-out providing either a fiducial volume of the module of 188 kg and the mass ratio of scintillator bars to water as 1 : 4 or a fiducial volume of 47 kg and the mass fraction of scintillator bars as 100 %.

In conjunction with WAGASCI there is also the INGRID proton module, seen in figure 3.11, and INGRID module, seen in figure 3.12. The proton module can be used as a hydro carbon target and solely comprised of scintillator bars and is read out in the same way as the experiment it was taken from, Interactive Neutrino GRID (INGRID) [92]. From this experiment there is also the INGRID module which is a non-magnetised muon range detector comprised of scintillator bars interlaced with iron. The fully installed module chain, without the Baby MIND, can be seen in figure 3.13 and the full sketch with the Baby MIND in figures 3.14 and 3.15. By combining and taking measurements with all of these different modules as targets measurements can be made on inclusive and exclusive differential cross sections of the charged current neutrino and antineutrino interactions with water and hydrocarbon. This will in turn make it possible to reduce one of the most significant sources of uncertainties of the T2K experiment [61].

The main MRD, downstream of the target is the Baby MIND. It can all be seen in figure 3.8 and in figure 3.9.

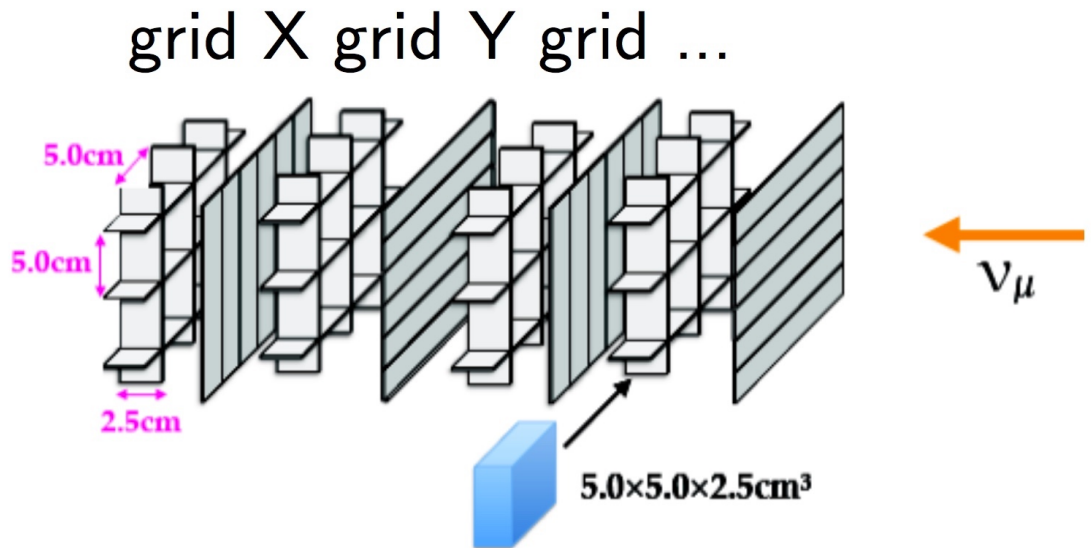


Figure 3.9: The structure of the WAGASCI detector with scintillator bars either horizontally or vertically with a structure to support each the boxes.

3.2.3 Electronics

Scintillator bars are used as active elements in the WAGASCI detector. The bars are similar to the Baby MIND as they also use WLS fibres to transport light to Hamamatsu MPPCs. The performance of the scintillator bars was measured with a 600 MeV positron beam. The average light yield was found to be 10-18 p.e. and the detection efficiency was better than 99% for the whole region of scintillator with a threshold set to 1.5 p.e. The detector performance of the water-in WAGASCI module was checked during the beam operation in 2017.

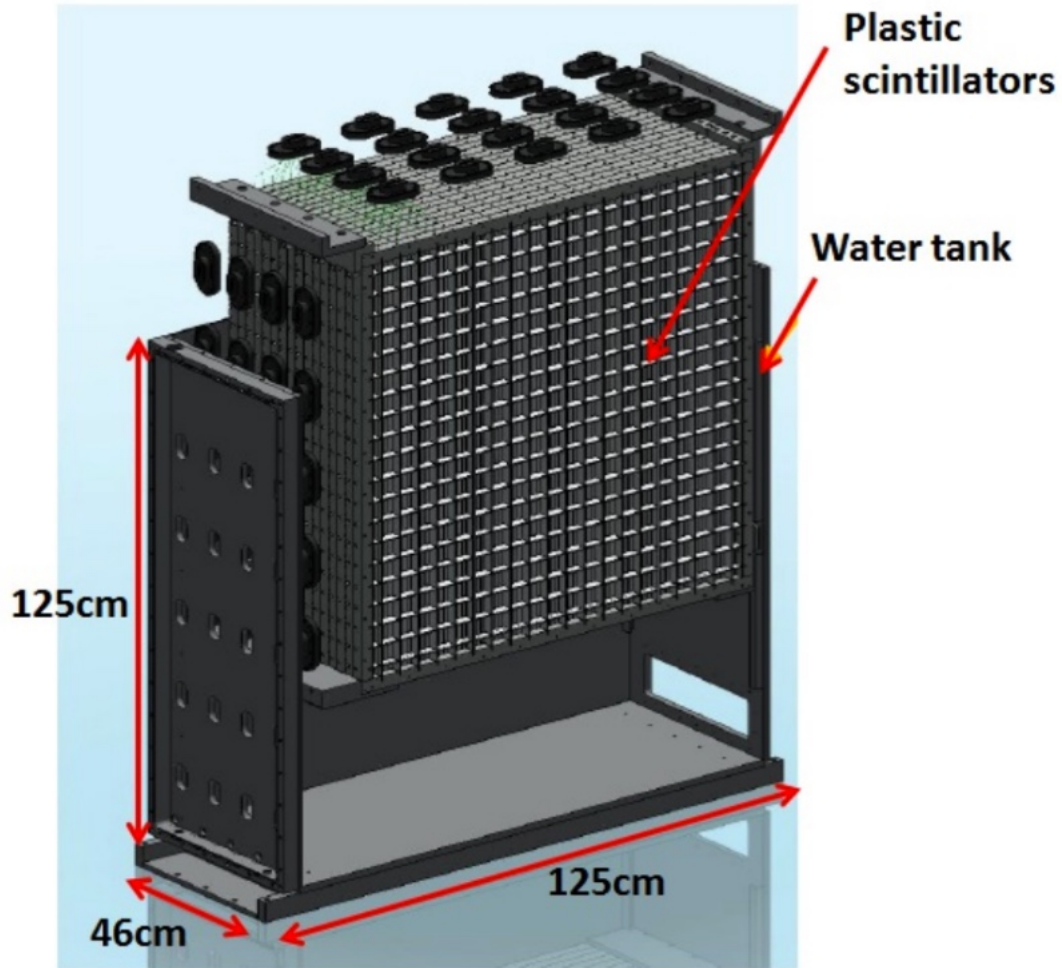


Figure 3.10: An illustration of the full WAGASCI module

As front-end electronics of the WAGASCI modules, a Silicon PM Integrated Read-Out Chip (SPIROC) is adopted. SPIROC is a 36-channel auto-triggered front-end ASIC, and is produced by OMEGA/IN2P3. It not only contains an analog signal processing part such as amplification and shaping of the waveform, but contains a digital signal processing parts such as auto-trigger and timing measurement. Charge of MPPC signal is sampled by track-and-hold circuit. A Front-end electronics board, Active Sensor Unit (ASU), has been developed with the SPIROC2D chip, which is the latest version of SPIROC. Each readout board is designed to control a 32-channel arrayed MPPC, and 40 of the ASU boards are aligned on the module surface. The data acquisition system used for this detector, including back-end boards, has been developed for prototypes of ultra-granular calorimeters for the International Linear Collider (ILC), and independent of the T2K DAQ system. To synchronize the DAQ system to J-PARC neutrino beam, pre-beam trigger and beam trigger are sent to the clock control card. The beam trigger signals are converted from optical signals to NIM signals at NIM module

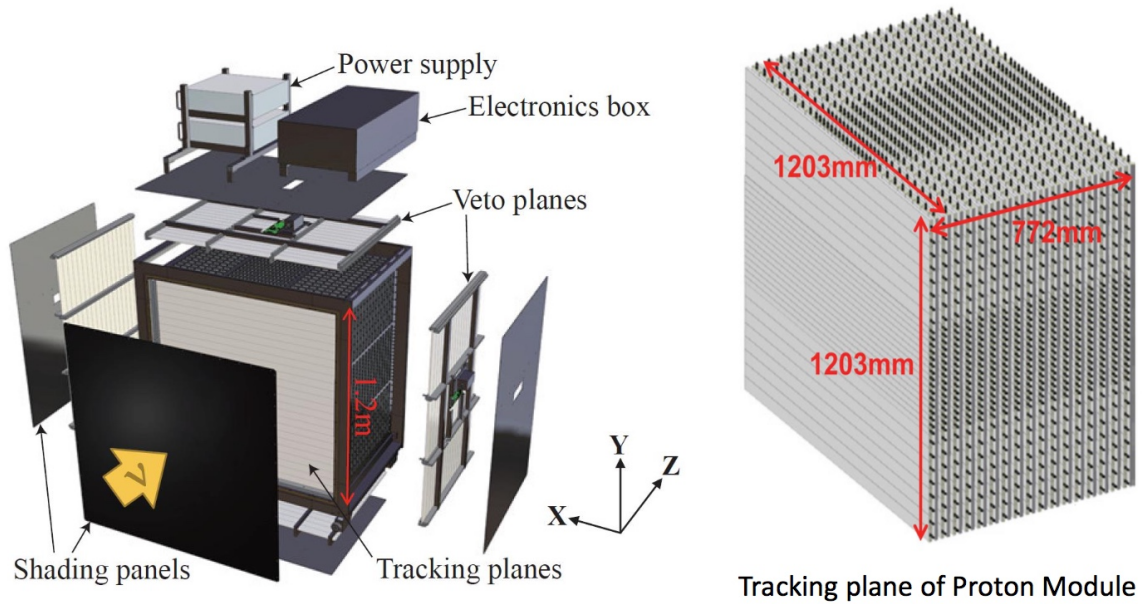


Figure 3.11: An illustration of the INGRID proton module.

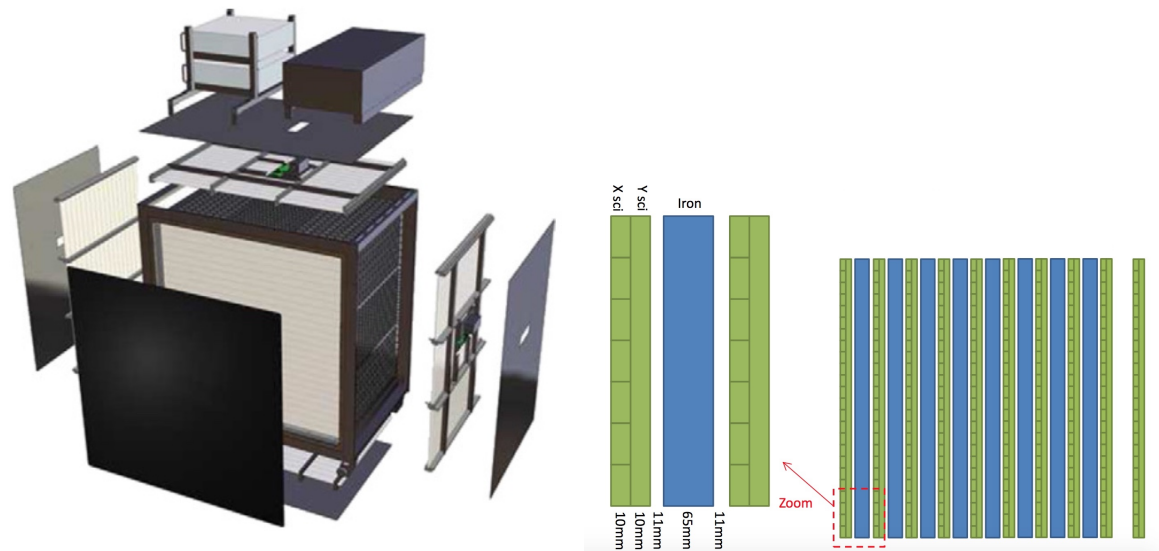


Figure 3.12: An illustration of the INGRID module.

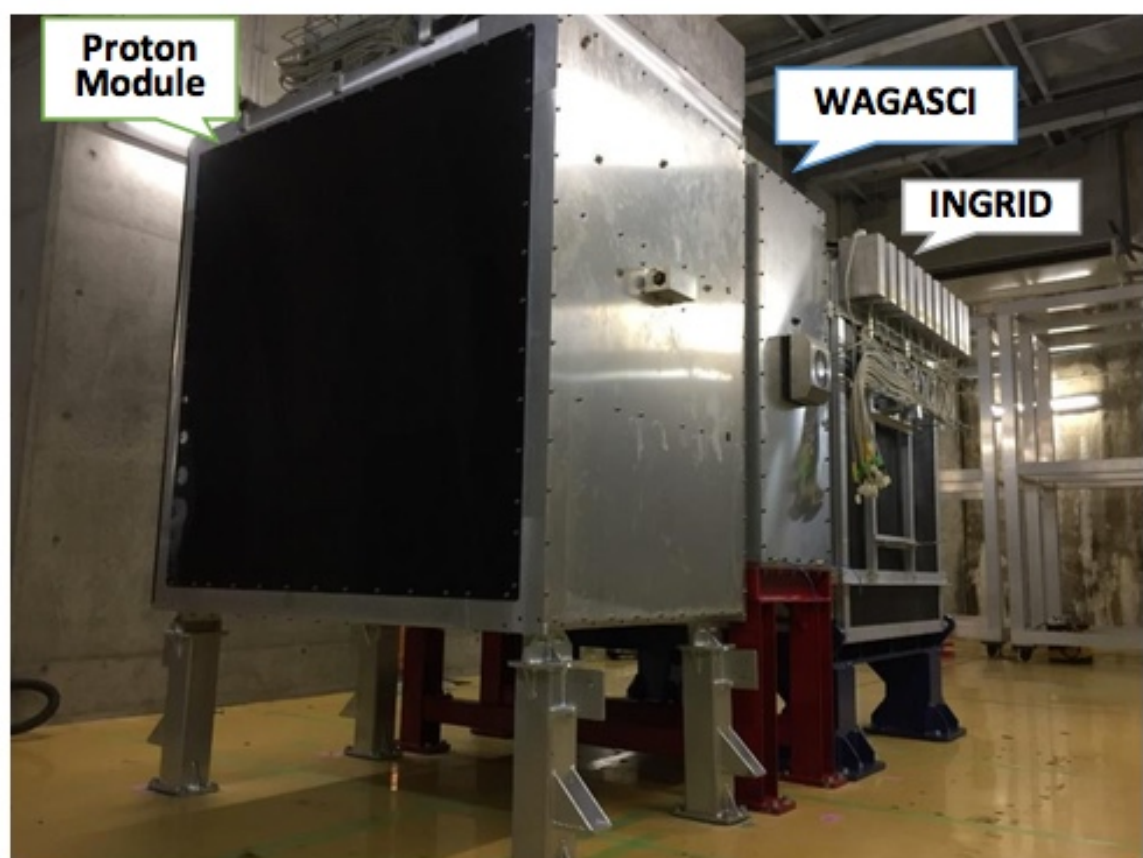


Figure 3.13: A photo of the fully installed WAGASCI module with the INGRID and INGRID proton modules at the B2 floor at J-PARC.

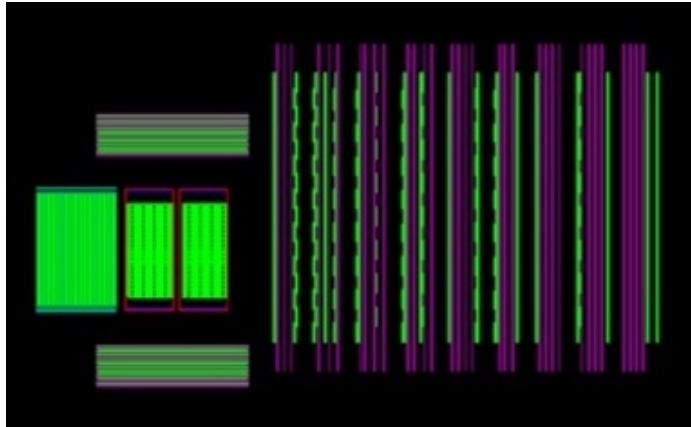


Figure 3.14: An image showing the B2 environment with (From left) INGRID proton module, WAGASCI, INGRID module and Baby MIND. The side MRDs are in gray.

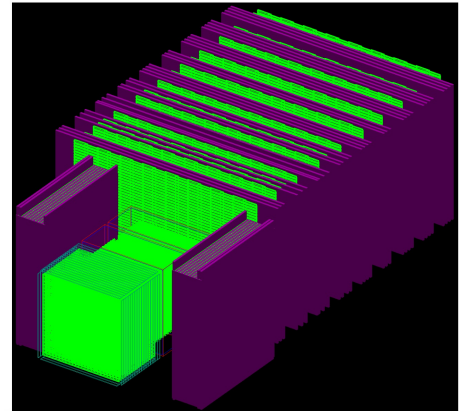


Figure 3.15: B2 environment seen slightly from the side.

on the B2 floor. In addition, the information of spill number are delivered with 16-bit ECL level signals, and converted to an Ethernet frame by an FPGA evaluation board to be directly sent to the DAQ PC.

3.2.4 MRD and Baby MIND

The WAGASCI detector requires a muon range detector to measure the momentum and charge of outgoing muons to identify the neutrino event and calculate the neutrino cross-section. As mentioned above, Baby MIND provides this role placed after the main target. There are also two much smaller MRDs on either side of the target to measure background muons from other sources or which have been produced from the neutrino beam but will miss the target or Baby MIND. These side MRDs will not be able to provide any momentum or charge information and will only be used as an extra veto plane for acceptance measurements. The layout can be seen in As seen in figure 3.8. The main event requirements are that the neutrinos decay somewhere in the target and produces a muon within a suitable angle to traverse four scintillator planes of the Baby MIND.

3.3 Summary

In this chapter the Baby MIND and WAGASCI detectors and collaboration has been presented as well as a description of the current status.

Chapter 4

SaRoMaN

4.1 Introduction

The software environment used for Baby MIND is the Simulation and Reconstruction of Muons and Neutrinos (SaRoMaN) software suite which is a comprehensive software for MIND/nuSTORM detectors and has been developed at the University of Glasgow over several iterations [83, 93, 94]. The software has been expanded to be able to model and simulate a generic detector with limitations in the current implementation of the reconstruction. It includes a complete range of functionality for simulating single particle beams, through GEANT4 [86] or neutrino beams, through GENIE [95], including geometry design, digitisation and reconstruction through RecPack [96]. The software suite is also shipped with several analysis code examples written in ROOT [97]. It has been created exploiting software engineering and object-oriented techniques and implemented in the C++ and Python programming languages. The software is accessible on request from <https://1space.ppe.gla.ac.uk>.

4.2 General structure

The SaRoMaN software suites main design goals have been to promote modularity, provide a single point of entry for the design and input variables and to simplify usage. With this in mind the SaRoMaN software is split into four main parts which can be replaced or altered independently of the others as long as the input/output flow is conserved. The parts are denoted, wrapper, simulation, digitisation and reconstruction with the main flow regulated by the wrapper seen in figure 4.1 and a more detailed view in figure 4.2. Each part will be discussed further below.

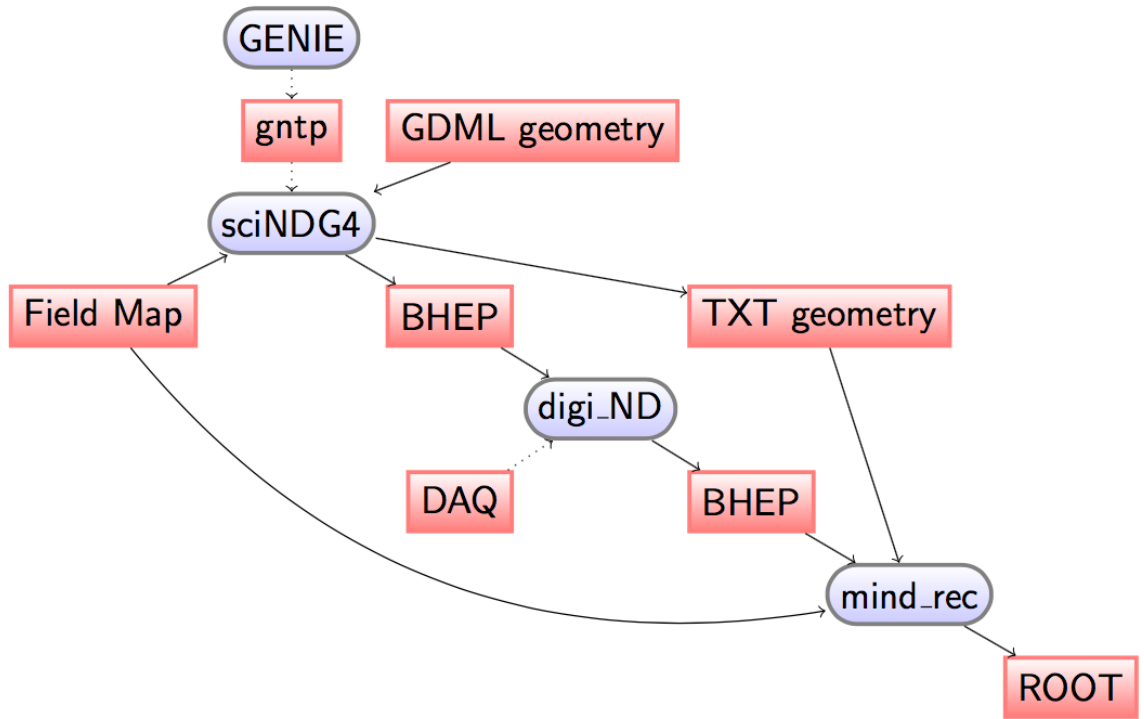


Figure 4.1: Code flow of the SaRoMaN software suite all controlled and handled through a wrapper.

4.3 Wrapper

To simplify the installation, compilation and usage of the other parts in the SaRoMaN suite, a wrapper has been developed in the Python programming language. This wrapper, aside from the above, handles all input variables, file names, writing of configuration files, standardisation of magnetic field map and geometry, and data flow between the other parts.

To simplify for the user, all of the installation, compilation and running are handled through simple command line inputs with the option of more advanced commands being issued through the use of the Python wrapper class. After installation SaRoMaN can be run with some default parameters, a full run diagram can be seen in figure 4.3.

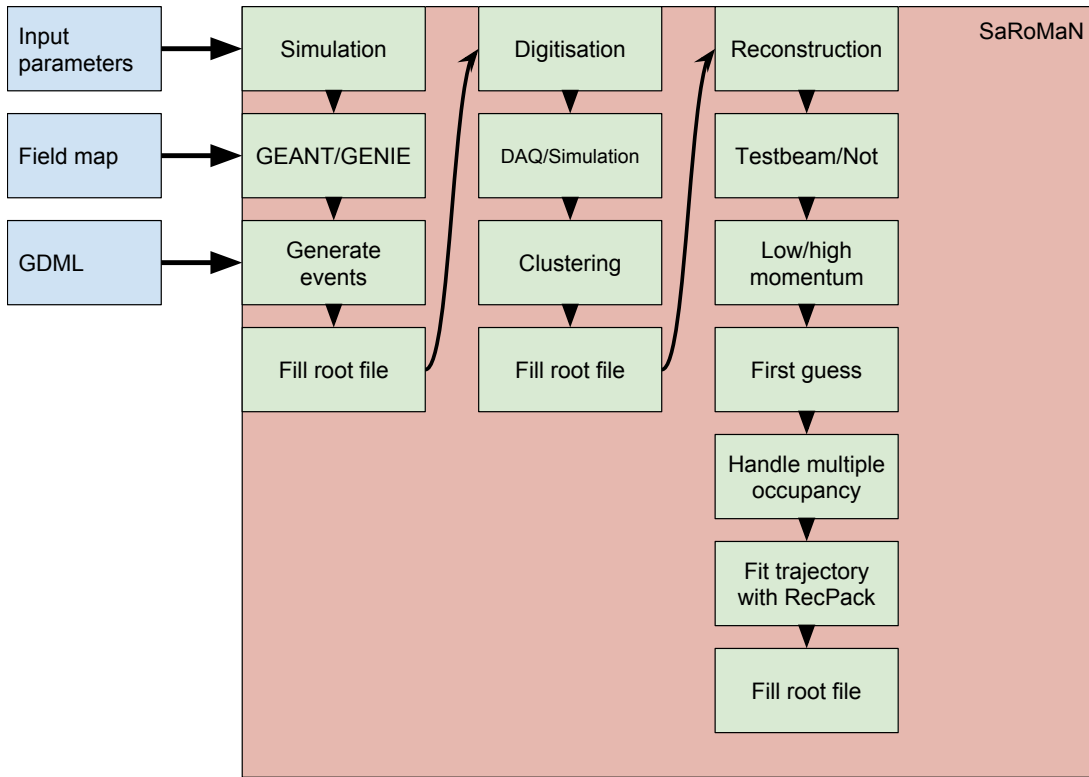


Figure 4.2: Code structure of the SaRoMaN software suite all controlled and handled through a wrapper.

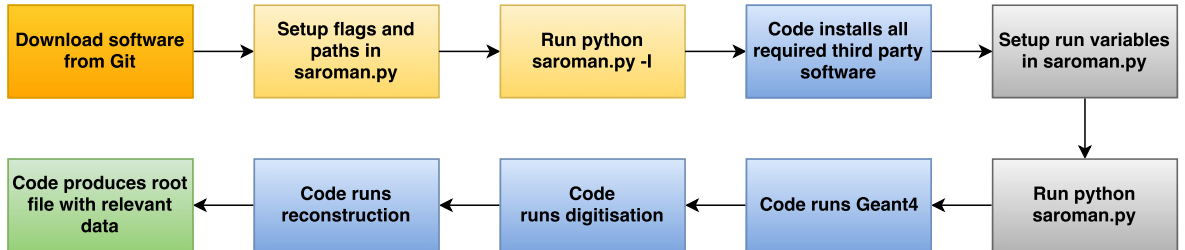


Figure 4.3: Example of how to run a default simulation.

4.4 Simulation

Simulations are used to test and model how particles will interact with a detector model and what scintillator hits can be expected. The outputs from the simulation include the position of the hit on a bar, the location of a bar, the time of the hit and the amount of energy that was deposited. For the studies performed in SaRoMaN well tested physics models are used in GEANT however the option exists to add new physics and to test new theoretical models.

The simulation comes with two different modes, neutrino or "single particle". For neutrinos GENIE is first run to generate neutrino events. These events are later populated and the de-

tector constructed through GEANT. In a single particle mode a beam of a single particle type is assumed, GENIE is not called and the simulation and detector construction are handled through GEANT.

A unique feature is that the whole SaRoMaN suite uses a single geometry definition for the whole suite, written in Geometry Description Markup Language (GDML) [98] which is interpreted in GEANT and is passed as a simplified .txt file to the reconstruction, which simplifies any changes of the geometry. This GDML file can be used to describe simple detectors, such as the TASD, as well as the full Baby MIND and even any combination of several of these put together in any layout. It is also possible to generate a GDML file from CAD software to get all of the constructional details from the detector.

4.5 Digitisation

Digitization is the emulation of the hardware required to build the detector. It needs to handle the response of the electronics and describes the expected output signals, based on input hits in the detector. Any electrical system can be described as providing an output based on the systems response function and the input signal. The digitization is based on a description of the response function of the detector for the simulated input.

This is currently done in a simplified way by smearing data with different Poisson distributions as well as handling events which are distinguished by a large time difference. For the Baby MIND detector the algorithms take the horizontal and vertical bar hits and clusters together hits to construct x, y and z positions along with the energy deposition and time to produce physical hit points. The full program flow can be seen in figure 4.4.

As a way to simplify the integration and implementation, the data acquisition (DAQ) used for the different test beams have been implemented in the digitisation as well. In this mode, real data is given as input and only the clustering takes place. Due to the usage of a single geometry, a token simulation has to be run in this mode as well to properly construct the geometry.

To ensure that all further analysis is performed properly, there is no way to distinguish data coming out of the digitisation as being simulated or read in through the DAQ.

One of the most difficult design features of Baby MIND is combining hits from both vertical and horizontal bars. It is possible to get hits which can not be combined without ambiguity. In figure figure 4.5 it is impossible to distinguished the green hits from each other and the same with the red hits. The current method is for the digitisation to create both hits at all times and these hits being handled by the reconstruction where they can be distinguished by looking at track construction.

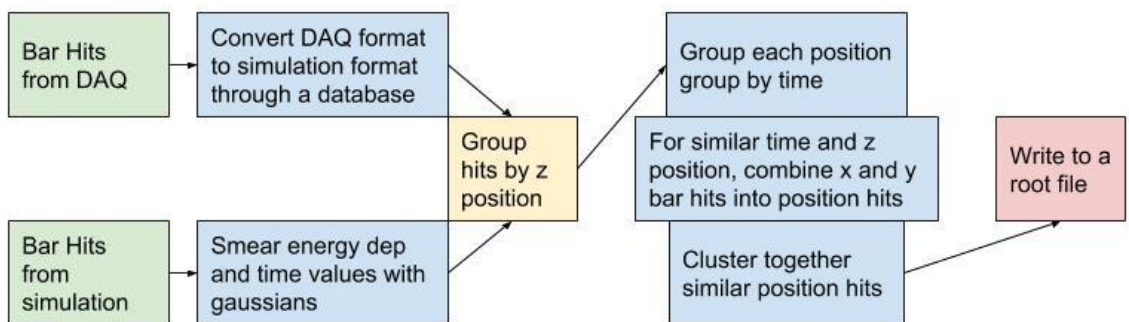


Figure 4.4: Program flow for the digitisation.

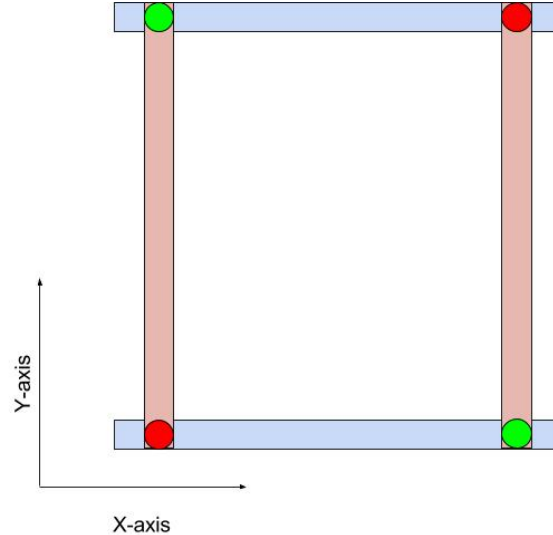


Figure 4.5: Illustration of the difficulty in combining hits in vertical and horizontal bars.

4.5.1 Simulated data

The digitisation is provided with a .root file containing all of the information from the simulation. Given that the data is assumed to be analysed offline, the first task is to separate any hits into event time windows, where hits can be seen as coming from the same particle. The main difficulty is to allow for the particle to fully traverse the detector and allow delay in electronics response in the time window. This provides a number of hits in several time bins, denoted as events without having any filter by use the position.

After the timing clustering so called 3D space points are created by combining the vertical and horizontal bar hits for a specific module. These three points are combined to provide an x,y and z coordinate. In this bar coincidence as well as overlap are taken into account as mentioned previously by creating all of the possible points. For this position clustering energy is combined between the individual hits to create a or several clusters with a discrete position based on bar overlap, deposited energy and hit time.

The final step in the digitisation is to smear the value of deposited energy and hit time based on measured values of propagation time through the scintillator bars given the simulated hit position and not only the bar position.

4.5.2 DAQ

The current DAQ framework for the Baby MIND detector is based on being used offline, processed both after and away from the acquisition.

For simplicity the DAQ converts the acquired data and converts it into the same format as expected from a simulation so that the digitisation can be used in the same way. The main

difference is that the smearing used for simulated data is turned off.

Data comes in with files specific for each FEB. This data, has channel number, hit time and hit amplitude. The first step is to convert the data into space-positions, either vertical or horizontal bar position information and z-position. This is done by using a database based on FEB, channel number and knowledge of the physical layout of the detector. The second step is ensuring that each hit position has a corresponding time and amplitude. Step three is to cluster all of the hits in specific time slots, which are equivalent to the event time windows. When this is done several low level filters are performed, to ensure that an event has enough hits to produce atleast four 3D space positions in a time slot. After these steps the data is equivalent to the data produced by a simulation and is processed to be passed onto the reconstruction.

4.6 Reconstruction

The reconstruction takes the digitized hit data and assembles tracks and vertices. The main physics parameters are the momentum as well as the charge of the particle. The main problems occur when there are overlapping hits with multiple occupancy per bar. In this situation, it is difficult to distinguish between valid hits and to extract the momentum of the track and its charge. The first problem is handled by removing and adding hits and using a χ^2 analysis through a Kalman fitter package, RecPack [96], to find the best trajectory that fits all hits. The second problem is solved through various algorithms to estimate the charge and momentum using different fits.

For simplicity the reconstruction currently contains a mode denoted as "test beam" where it does nothing more than writes out the input data into a final .root file.

4.6.1 Structure

The reconstruction software has been structured to ensure that the software is as modular as possible. It is currently based on the Kalman fitter package known as RecPack [96] to provide both a framework and back bone for handling track objects. It is used for historical reasons, however SaRoMaN would benefit from using a Kalman fitter implementation which is still maintained, development, with few and understood bugs and has documentation.

A Kalman fitter is given an underlying model of the system, in our case knowing that particles travel as helices, and a model of the detector as well as other known inputs to the system to form an estimate of the different states in a way that is better than using only a single measurement. This is particularly well suited in particle physics where random noise is given through multiple scattering. It can also take into account the various energy losses and varying magnetic fields. Through this it can use measurements in different parts of the detector to estimate both how the particle has and will continue its propagation. Compared to other models, a Kalman fitter has no underlying assumption about the errors being Gaussian.

In high energy physics one frequently faces the problem of modeling the evolution of a dynamic system from a set of experimental measurements. Most of reconstruction programs use similar methods. However, in general they are reimplemented for each specific experimental setup. Some examples are fitting algorithms (i.e. Kalman Filter), equations for propagation, random noise estimation (i.e. multiple scattering), model corrections (i.e. energy loss, inhomogeneous magnetic field, etc.), model conversion, etc. Similarly, the data structure (measurements, tracks, vertices, etc.), which can be generalised as well, is not reused in most of the cases. The motivation for using RecPack comes from it combining all of this into a simple software package.

SaRoMaN has been split into first initializing the fitter, then using an initial pattern classification to choose reconstruction mode. Currently particles and showers are identified, but only muon-like particles are reconstructed. In this identification a track is produced along with any off track hits. Finally the fitter performs a final charge and momentum estimate on the track and tries to fit more tracks to the off track hits. If this is a neutrino sample, proton/neutron tracks are only built if it finds an initial muon track.

The test beam mode ignores the event classification and uses the fitter to pass information from input through to the final root file.

The reconstruction has split into several minor tasks.

- Handling data. Pushing the input data into a final root file.
- Track building / pattern recognition, given an event, (a time window) can we build a track from this?
- Fitting, with a candidate track, is it possible to add more hits to the track and make it longer? Find secondary tracks? Also, is it possible to estimate the momentum and charge of the track?

4.6.2 Pattern recognition

The pattern recognition tries to estimate if the event is muon like or not. It starts by looking at the number of hits for a given event. There are currently two main limitations to if a track can be fitted in SaRoMaN:

- At least 4 hit modules are required to do any form of charge estimation or track building.
- At least 10 hit modules are required to perform a Kalman fitting.

Outside of these limitations, currently only muon track fitting has been implemented. The general assumption is that each event will contain at least one muon track followed by other secondary tracks. If this is not the case the event is discarded. The event filtering is done very simply by assuming anything that is not a shower is a muon. Single hits here refers to separable space points meaning that for each z-position there is only one unique hit. The aim of the pattern recognition is to find as many tracks with single hits as possible. In the pattern recognition track are built up from so called track stubs of at least 4 single hits. As soon as a track stub is created other hits can be added onto the track stub to create a final track using a χ^2 analysis as a metric. This χ^2 analysis is run through the fitter and requires an initial charge

and momentum guess. This means that the best suitable hits are added to the track stub and the other hits saved for use in finding secondary tracks.

The program flow can be seen as taking in an event worth of hits and returning a number of tracks along with hits which could not be fitted into any track. Each returned track contains only single hits as well as a momentum and charge estimate. The latter two are then improved by the fitter.

4.6.3 Fitting

The fitters main job is to build tracks and to estimate the momentum and charge of that track. There are two modes, one main mode for hits with more than 9 hits are passed into the Kalman fitter RecPack. When it is not possible to perform a helical fit and for any track with more than 3 hits, a self implemented lever-arm approach is used. In both cases RecPack is used to build the tracks, however the momentum and charge reconstruction has to be split depending on the possibility of a helical fit or not. The full helix equation seen below, has a total of 9 parameters and takes 10 measurements to be fully fitted.

$$x(t) = a\cos(bt + c) + d \quad (4.1)$$

$$y(t) = e\sin(ft + g) + h \quad (4.2)$$

$$z(t) = kt \quad (4.3)$$

The helix can be related to physical quantities as.

$$x(\phi) = x_0 + d_p \cos \phi_0 + \frac{\alpha}{\kappa} (\cos \phi_0 - \cos(\phi_0 + \phi)) \quad (4.4)$$

$$y(\phi) = y_0 + d_p \sin \phi_0 + \frac{\alpha}{\kappa} (\sin \phi_0 - \cos(\phi_0 + \phi)) \quad (4.5)$$

$$z(\phi) = z_0 + d_z - \frac{\alpha}{\kappa} \tan \lambda \phi \quad (4.6)$$

where $\vec{X} = (x_0, y_0, z_0)$ is the arbitrary helix pivot point, d_p is the distance from the helix to the pivot point in the xy plane, ϕ_0 is the azimuthal angle from the pivot point with respect to the helix center, κ is the signed reciprocal transverse momentum, d_z is the distance of the helix from the pivot point in the z direction, and $\tan \lambda$ is the dip angle. The deflection angle ϕ is measured from the pivot point and specifies the position of the charged particle on the helical track. The variable κ can be used to relate to the transverse particle momentum, P_T

and relate to the magnetic field as

$$\kappa = Q/P_T \quad (4.7)$$

$$\rho = \alpha/\kappa \quad (4.8)$$

where Q is the particle charge, ρ being the signed radius of the helix, and $\alpha \equiv 1/cB$ being a magnetic-field-dependent constant with c as a constant and B the magnetic field strength. The full particle momentum can be obtained as:

$$\vec{P} = -\frac{Q}{\alpha} \frac{d\vec{X}}{d\phi} = \frac{1}{|\kappa|} \begin{pmatrix} -\sin(\phi_0 + \phi) \\ \cos(\phi_0 + \phi) \\ \tan\lambda \end{pmatrix} \quad (4.9)$$

In practice, this fit also takes both energy loss in the detector and multiple scattering into account when calculating the χ^2 values when fitting the parameters.

This motivates the requirement for two different modes. If a helical fit is possible RecPack performs the fitting and returns a final fitted helix, within provided measurement errors, with a momentum and charge estimate.

If a helical fit is not possible, denoted the low momentum case, several different algorithms are used.

The fitting is performed in a usual Kalman way by using this underlying equation and assuming each measurement point has some error. Each measurement point \vec{X} is related to the next through extrapolating the helical equation and assuming an error: $\vec{X}_{k+1} = F_{k+1,k} \vec{X}_k + \vec{w}_k$. It is in this error term where multiple scattering and energy loss is taken into account. The output is then given as: $\vec{Y}_k = H_k \vec{X}_k + \vec{v}_k$. The helical equation goes into forming the matrix F and H .

It should be noted that in the Baby MIND a helix model is an approximation given that there is no fully encompassing magnetic field and various different materials, iron and scintillator, in the detector. A more correct, but much more complex model would be a helix in the iron with straight line segments in-between for the non-magnetised air gaps and scintillator modules.

4.6.4 Low momentum algorithms

The force applied to a particle travelling through a magnetic field is given by the Lorentz force:

$$\vec{F} = q \frac{\vec{v} \times \vec{B}}{c} \quad (4.10)$$

where c is the speed of light in vacuum, v is the velocity, q the charge and B the magnetic field vector.

Using Newtons second law one produces the following differential vector equation.

$$\vec{F} = m\vec{a} = m\dot{\vec{v}} = q\frac{\vec{v} \times \vec{B}}{c} \quad (4.11)$$

The solution to this equation is given by:

$$\vec{P} = m\vec{v} = q\frac{\vec{l} \times \vec{B}}{c} \quad (4.12)$$

where P is the momentum of the particle and $\vec{l} = \vec{X} - \vec{X}_0$ is a vector containing the lengths traversed through the magnetic field.

Using the definition of the cross-product, writing this as a scalar equation, using the small angle approximation and writing using S.I. units produces the normally recognisable equation

$$P = 0.3QB_{\perp}\frac{|\vec{l}|}{\theta} = 0.3QB_{\perp}R \quad (4.13)$$

where P is the momentum in MeV/c, the charge Q in in units of e , the magnetic field strength B is in T and the radius of curvature R is in cm. This is only one way of deriving the relation, but it is one of the main equations used for momentum reconstruction in SaRoMaN. The charge is then reconstructed using $P/|P|$.

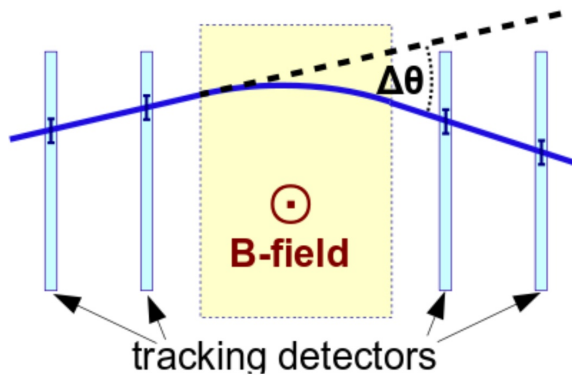


Figure 4.6: Figure of one bending in first plane in mind.

A previous study performed in the collaboration showed that the best way of evaluating the charge using this method comes from comparing both the first and second bending in the detector, seen in figure 4.6, using two different distributions to handle the scattering.

Using the distribution of multiple scattering angles and the notation in figure 4.7, the choice is taken as.

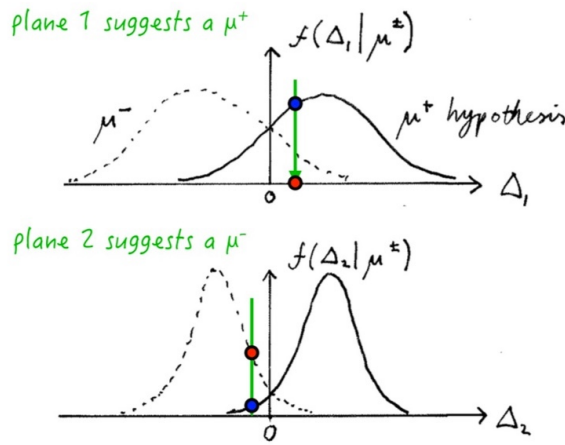


Figure 4.7: Illustration of the angular distributions and criteria for selecting charge.

Reconstruct μ^- if

$$\frac{f_{\mu^-}(\Delta_1)}{f_{\mu^+}(\Delta_1)} > \frac{f_{\mu^+}(\Delta_2)}{f_{\mu^-}(\Delta_2)} \quad (4.14)$$

and as μ^+ if

$$\frac{f_{\mu^+}(\Delta_1)}{f_{\mu^-}(\Delta_1)} > \frac{f_{\mu^-}(\Delta_2)}{f_{\mu^+}(\Delta_2)} \quad (4.15)$$

The bending angles are calculated from both measurement planes, (or only one if not possible) and tested against a null-hypothesis of having deflection from only multiple scattering [12] given by:

$$\theta_0 = \frac{13.6 MeV}{\beta c p} z \sqrt{x/X_0} [1 + 0.038 \ln(x/X_0)] \quad (4.16)$$

where p is the momentum, βc the velocity, z the charge number of the incident particle and x/X_0 is the thickness of the scattering medium in radiation lengths.

The probability, using this notation is given in equation 4.17.

$$F_{\mu^\pm} \frac{1}{2\pi} e^{-(\theta_0 \pm \Delta)^2} \quad (4.17)$$

Another part of the reconstruction is to estimate the momentum. Many different methods using the scattering or fits have been studied for this low momentum region, however the current best approach is to use the continuous slowing down approximation (CSDA) range. CSDA is based on knowledge of the energy loss in the material before a certain measurement in the detector, assuming the particle deposits an average energy in all materials which it passes through. In the Baby MIND given that the density varies and that there are measuring planes at some distance of each other, this provides a rough estimate of the momentum and the errors depend on how many iron plates are between the specific scintillator modules

for that measurement. In the part of the detector which is least designed for this, where there are three iron modules between scintillators the error on the momentum estimate can be approximated as $\sqrt{2} \times 90\text{ MeV}/c$. This method cannot be used for tracks which pass through the full detector as then the error is impossible to estimate. Combining information from the CSDA and the angle produces the final momentum and charge estimate.

If the angular estimate does not work due to multiple scattering a final estimate is used by using a quadratic fit for the few hits provided.

4.6.5 Performance

During development of SaRoMaN two main metrics were used to evaluate performance, charge reconstruction efficiency and track reconstructed efficiency. These metrics provide information about how many simulated tracks can be reconstructed compared to total number of simulated tracks and how many of those reconstructed tracks have the correct charge. This is done for muons of both charges and different momentum values.

Performance will be shown for the initial and proposed layout, for which the software algorithms were designed, the layout required for the test beam due to construction constraints and a final study based on the layout used for the WAGASCI detector layout. The main difference between the initial and test beam layout is removing the initial measurement point D0, restructuring the layout and adding gaps between each of the blocks, seen in figure 4.8. This was done from a constructional not a physics motivation.

The charge identification is however improved when utilizing a measurement point from a neutrino target such as the WAGASCI, however this will reduce the lower limit of reconstruction since the muons must traverse the material of the WAGASCI.

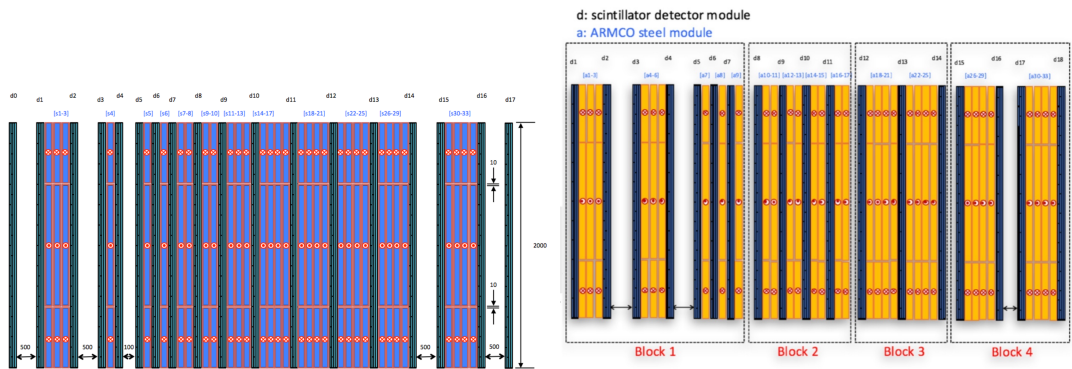


Figure 4.8: (Left) Image of the initial Baby MIND layout. (Right) The current Baby MIND layout. The main differences consists of removing the first scintillator plane, some different layout in the middle blocks and removed the final scintillator plane.

In figure 4.9 results for the initially proposed geometry can be seen. The plots have been

generated by simulating muons and anti-muons in the SaRoMaN framework. The results for the slightly changed test beam geometry layout can be seen in figure 4.10.

The main difference between the results are both below $1 \text{ GeV}/c$ and in the region above $1 \text{ GeV}/c$ and below $2 \text{ GeV}/c$. Below $1 \text{ GeV}/c$ the charge reconstruction is slightly worse for the test beam geometry which can be attributed to the removal of the first scintillating plate D0. There is also a slight change in the shape of the reconstruction efficiency above $1 \text{ GeV}/c$ and below $2 \text{ GeV}/c$ related to the change of the structure of the detector and additions of gaps providing some drift between measurement positions. For both of the layouts the reconstruction efficiency $> 95\%$ above $0.7 \text{ GeV}/c$ and is charge identification efficiency is $> 95\%$ above $0.7 \text{ GeV}/c$. For the full region both reconstruction and charge identification efficiencies are $> 80\%$.

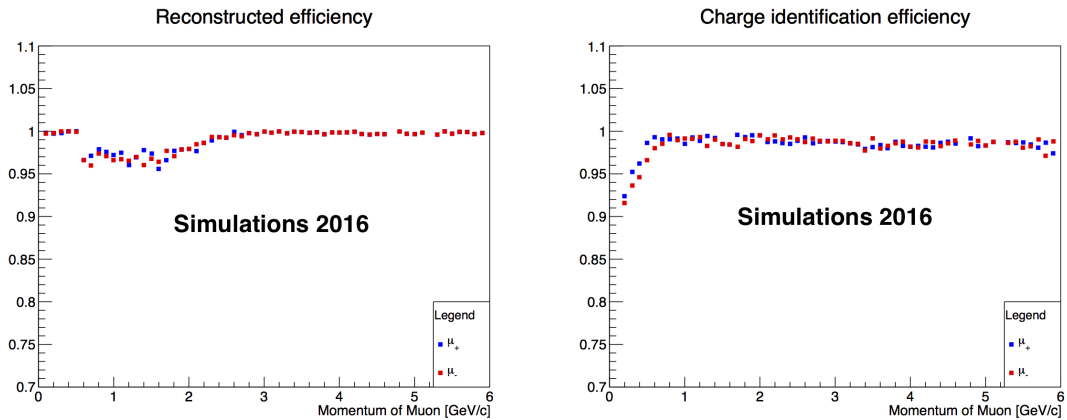


Figure 4.9: Metric plots of the initial Baby MIND layout with all algorithms adjusted to utilize this layout.

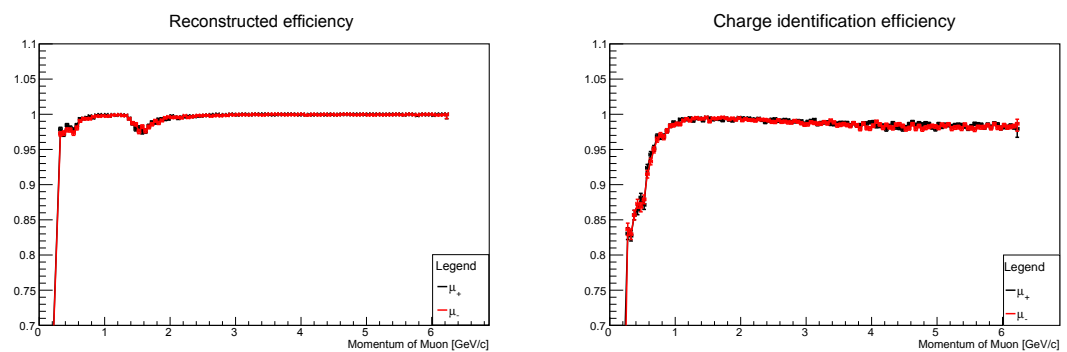


Figure 4.10: Metric plots of the CERN test beam Baby MIND layout.

4.6.6 DAQ/Unpacking

Currently data has to be recorded by the electronics and handled by a test beam computer system. The data is written to disk and needs to be written completely with full spills before

it can be processed off-line after the data taking.

The format consists of a Time slot containing a spill with several triggers. Each trigger contains all of the hit data from the various channels at all the times inside the trigger. Hit data contains amplitude and time measurements with the channel information. Each time measurement comes in steps of 2.5 ns so the system can only distinguish hits on a channel if they happen more than 2.5 ns between each other. The triggers come in block of 10 μs resulting in at most 4000 events per channel per trigger. The format can be seen a bit clearer in figure 4.11.

Time Slot Start																																																										
31	30	29	28	27	26	25	24	23	22	21	20	19	18	17	16	15	14	13	12	11	10	9	8	7	6	5	4	3	2	1	0																											
TDM ID = 0																											TDM TAG																															
Spill header																																																										
31	30	29	28	27	26	25	24	23	22	21	20	19	18	17	16	15	14	13	12	11	10	9	8	7	6	5	4	3	2	1	0																											
Spill header ID		Board ID		1	SId	DAQ type		Spill Time from GTRIG (10ms res.)																																																		
Spill header ID		Board ID		0	SId	Spill tag (from reset request)																																																				
Spill time ID		Spill time on spill start (10ms resolution, max=745.6 h=31 days)																																																								
GTRIG header #1																																																										
31	30	29	28	27	26	25	24	23	22	21	20	19	18	17	16	15	14	13	12	11	10	9	8	7	6	5	4	3	2	1	0																											
GTRIG header ID		Global Trigger tag (from reset request)																																																								
Event Data : Hit #1																																																										
31	30	29	28	27	26	25	24	23	22	21	20	19	18	17	16	15	14	13	12	11	10	9	8	7	6	5	4	3	2	1	0																											
Hit time ID		Channel ID		Hit ID		Tag ID		EDGE		Hit time (2.5ns res.)																																																
31	30	29	28	27	26	25	24	23	22	21	20	19	18	17	16	15	14	13	12	11	10	9	8	7	6	5	4	3	2	1	0																											
Hit Amplitude ID		Channel ID		Hit ID		Tag ID		Amplitude ID		Amplitude measurement																																																
...																																																										
Event Data : Hit #n																																																										
31	30	29	28	27	26	25	24	23	22	21	20	19	18	17	16	15	14	13	12	11	10	9	8	7	6	5	4	3	2	1	0																											
Hit time ID		Channel ID		Hit ID		Tag ID		EDGE		Hit time (2.5ns res.)																																																
31	30	29	28	27	26	25	24	23	22	21	20	19	18	17	16	15	14	13	12	11	10	9	8	7	6	5	4	3	2	1	0																											
Hit amplitude ID		Channel ID		Hit ID		Tag ID		Amplitude ID		Amplitude measurement																																																
GTRIG trailer #1																																																										
31	30	29	28	27	26	25	24	23	22	21	20	19	18	17	16	15	14	13	12	11	10	9	8	7	6	5	4	3	2	1	0																											
GTRIG trailer 1 ID		Global Trigger tag (from reset request)																																																								
GTRIG trailer 2 ID		Hit counts within trigger		Global Trigger time (10us res. % current spill start, max=10.5s)																																																						
Spill trailer																																																										
31	30	29	28	27	26	25	24	23	22	21	20	19	18	17	16	15	14	13	12	11	10	9	8	7	6	5	4	3	2	1	0																											
Spill trailer ID		Board ID		0	SId	Spill tag (from reset request)																																																				
Spill trailer ID		Board ID		1	SId	Temperature																																																				
Spill time ID		Spill time on spill end (10ms resolution, max=745.6 h=31 days)																																																								
Time Slot End																																																										
31	30	29	28	27	26	25	24	23	22	21	20	19	18	17	16	15	14	13	12	11	10	9	8	7	6	5	4	3	2	1	0																											
TDM ID		ID=1	Slot ID		21-bits CHECKSUM																																																					

Figure 4.11: TDM, GTRIG, SPILL and DATA structure for the FEB readout communication.

4.6.7 Particle identification

For the particle identification Machine learning algorithms are used through the Toolkit for Multivariate Data Analysis with ROOT (TMVA) [99]. The main goal of the particle identification is to identify muon tracks from other background events on a high level basis. There are several filter trying to do this with the lower level however TMVA is needed to further improve this identification. This will be described in the MIND-test beam section.

4.7 Future development

Based on the main principles of easily shareable code, using the latest versions and simplicity, a further development of SaRoMaN has already been started by creating a fully new version based on newer versions of the third party software packages such as GEANT4, Geenie and root. By moving to the latest versions and ensuring that they will be easy to maintain the software becomes "future proof" which is very important for ensuring that the results are making use of the latest physics software. The new framework, following the Lord of the Rings theme [100], has been named SAURON (Simulation And Universal Reconstruction Of Neutrino-like events). SAURON also makes sure to only use open source software and has thus moved from the RecPack Kalman filter to use a Runge-Kutta and Kalman open source fitter known as GENFIT [101]. The software environment and code can be found in a docker environment at: <https://hub.docker.com/r/patha325/science/> If you only want the code, you can find it: <https://github.com/patha325/NewSaRoMaN>.

The simulation is based on a generic Geant4 simulation, which takes in neutrino data through are simulated with the GENIE open source code used by many. The reconstruction package GENFIT [101] package, used by several different experiments, takes generic points and uses a Runge-Kutta method to fit the points and calculate the track momentum and charge.

In a similar way to SaRoMaN, the running is handled by a very simple python script which ensures that all software runs coherently with each other. The geometry is handled in a GDMF file and read through all different parts to provide one single point of entry for the geometry. To ensure that the code can be used by anyone on different machines without a difficult installation process, the full software is provided in a docker container which means that the code can be run on any operating system.

To be compatible with the DAQ unpacking software developed by my colleagues, a secondary docker container has been created to handle the specific root version requirement as well as some other minor software requirements which all clash with the SAURON container.

SAURON is currently in a state where it can be seen as a simplified and novel version of SaRoMaN. Bar representation, clustering and pattern recognition is not currently implemented in the reconstruction, these are all handled by using truth information from the simulation or provided as extra information. None of these are seen to have a major impact on the results, but should be implemented in a future version. In a similar way, the DAQ unpacking is not included, instead the data is assumed to have been processed through it before being passed into the reconstruction. There are currently discussions regarding a unification of the DAQ unpacking and SAURON.

4.7.1 Containers

One of the main issues with scientific software is that they are developed by small teams, often not made publicly available and often the knowledge is only spread through scientific papers. This means that there are many great software solutions and packages which are not used by scientific collaborations, or are misused due to a lack of knowledge. One could argue that code is easy to read and that the purpose of a software should be easy to understand, however this assumes that all developers follow some form of coding standard and has/takes the time to develop their code properly which is often not the case. The clear solution to this problem would be to let physicists spend more time documenting and cleaning up their code as well as sharing it publicly. One problem which may arise is the use of specific third party software versions which make installation quite difficult especially in a climate where documentation is not prioritised and where software is constantly in development.

One proposed solutions which solves the problem would be to provide a full runnable coding platform such as a virtual machine. The benefits are numerous however most of these are even improved by moving to a new software technique known as a container.

4.7.1.1 Container vs Virtual machine

A container is similar to a Virtual machine (VM) but without requiring any abstraction of hardware, they also run on the OS kernel not requiring an added layer. In essence a container contains an application with the code and dependencies without also requiring a full copy of an operating system. This reduces the size of a container compared to a VM and decreases the boot time. It can handle more applications and require fewer VMs and Operating systems.

4.7.1.2 Container for particle physics simulations

There exists several containers which can be combined for various particle physics simulations. There is currently an official version of the root software in a container <https://root.cern.ch/root-docker-container-alpha-version> as well as various unofficial containers for software such as GEANT.

During the development of SAURON, early versions of the the container provide good tools for running particle physics simulations, without providing the SAURON framework or the neutrino specific parts. There are also early versions which provide the GENIE neutrino generator which provides a good staring point for running neutrino simulations.

4.7.2 Machine learning in particle physics

There has been some development of using machine learning techniques for various physics analysis as well as in event selection or particle identification for events in detectors. Focusing on the neutrino physics field, there have been a lot of interesting articles relating to how to identify neutrino events in Argon detectors using machine learning [102] [103].

4.7.3 Other good practises

4.7.3.1 Versioning

Currently the software is provided as is without any main release or naming convention. It would be beneficial to adapt a good versioning convention by tagging the software on gitlab. The container used has been provided with version numbers in an adhoc manner which should be tied into the software version number.

4.7.3.2 Continuous integration

For the SaRoMaN software a continuous integration platform was provided to ensure that installation of third party software as well as simple test analysis would always work regardless of bad committed code or broken download links. Something similar has been started for SAURON but not implemented fully and it is clear that it could be extended with thorough analysis and more specific test examples.

4.7.3.3 Documenting

Due to the time constraint no documentation exists for either of the software frameworks. The direct recommendation would be to spend time developing some doxygen documentation for the SAURON framework along with an easy how-to guide for new users.

4.8 Summary

In this chapter the software framework for Baby MIND has been described as well as future ongoing developments for improving the software framework. There has been a short discussion detailing the some of the metrics used for evaluation and discussion on how to continue the software development.

Chapter 5

Test beam

The Baby MIND collaboration performed an electronics validation using a Totally Active Scintillating Detector (TASD) at the T9 test beam in the PS facility at CERN in 2016. After construction was completed of Baby MIND in 2017, the full Baby MIND was commissioned in the same test beam.

The Baby MIND test beams tests took place at the T9 beam line at the proton synchrotron (PS) experimental hall. The beam lines are derived from the 24 GeV/c primary proton beam from the PS, which provides 2.4 s cycles of about 400 ms spill duration. The T9 beam comes of as a secondary beam by firing the proton beam at a 200 mm thick aluminium target which delivers secondary particles up to 15 GeV/c at a production angle of 0 degrees. The line is designed to provide the users with non-separated secondary particles, with positive or negative polarity, as hadron (pion) or muons and the beam momentum can be adjusted by setting the currents for the optical magnets of the beam line.

In this section details will be given to how data is collected and processed before showing some sample events and then further describe how data is processed in SaRoMaN to provide results obtained from each of the two test beams.

5.1 TASD-test beam

5.1.1 Setup

During June-July 2016 a test beam was performed to characterise the readout system, data acquisition (DAQ) and electronics to be used in the Baby MIND detector. The test beam was at the T9 beam of the East Area, operating at the Proton Synchrotron (PS) at CERN. A Totally Active Scintillation Detector (TASD) constructed under the AIDA-2020 project (Advanced European Infrastructures for Detectors at Accelerators) was used to test the readout

system, electronics, DAQ and reconstruction software. Baby MIND uses the same read out electronics and boards, with some firmware upgrades from this initial test beam.

The TASD detector consisted of horizontal and vertical planes, each plane with 16 scintillator bars, $10 \times 10 \times 1000\text{mm}^3$, and can be seen in figure 5.1 and in 5.2. Each bar is readout on both sides by S12571-025C Hamamatsu Multi Pixel Photon Counters (MPPCs). There are a total of twelve planes of either horizontal or vertical type in an alternating vertical, horizontal pattern. The layout is six combined planes providing both vertical and horizontal information with spacing between each. This summarizes as a detector with 96 horizontal and 96 vertical bars read out on both sides using a total of 384 MPPCs and a total size of 1m^3 . For the test beam only 16×16 bars were instrumented.

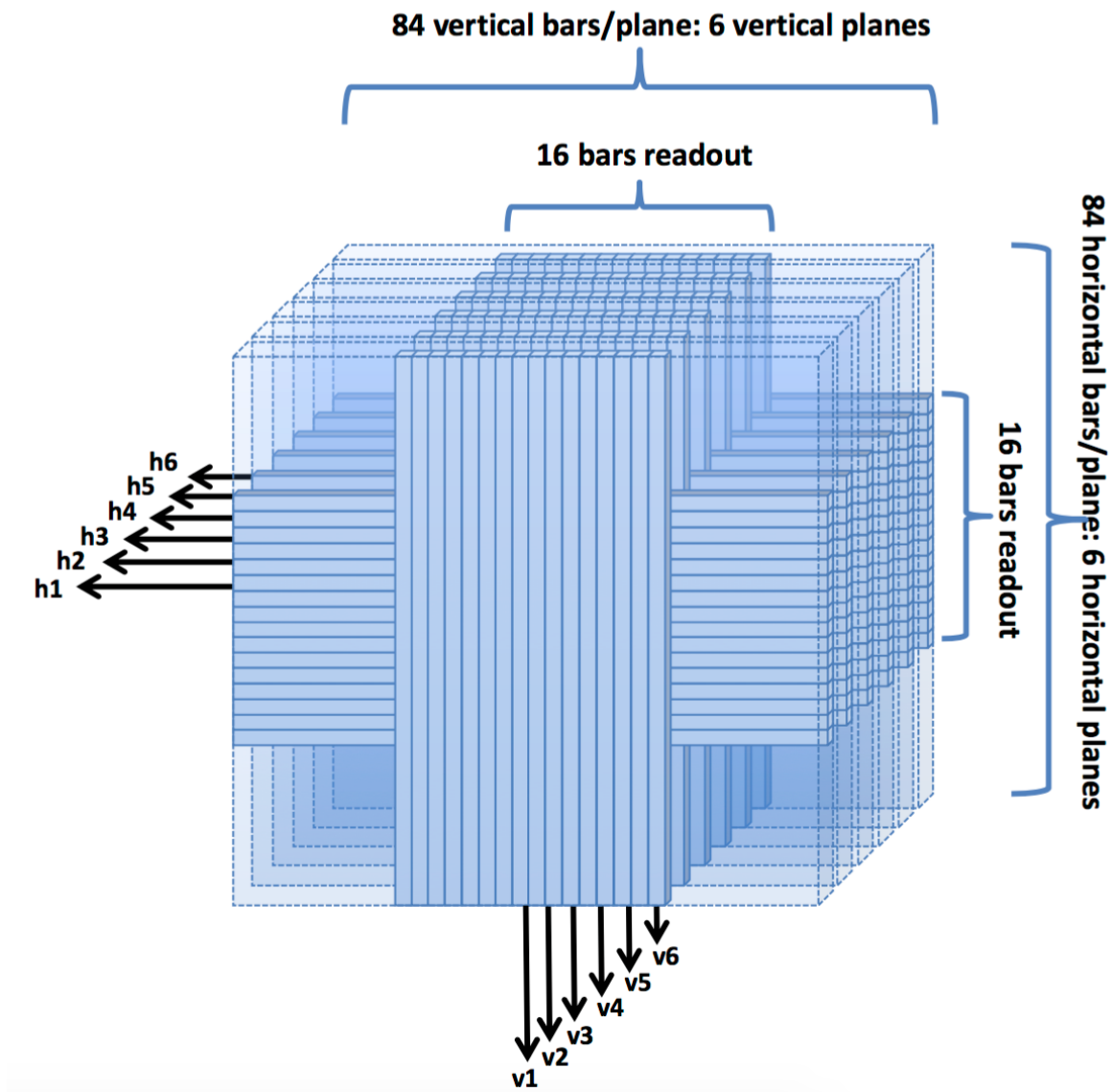


Figure 5.1: The TASD with the instrumented bars visualised

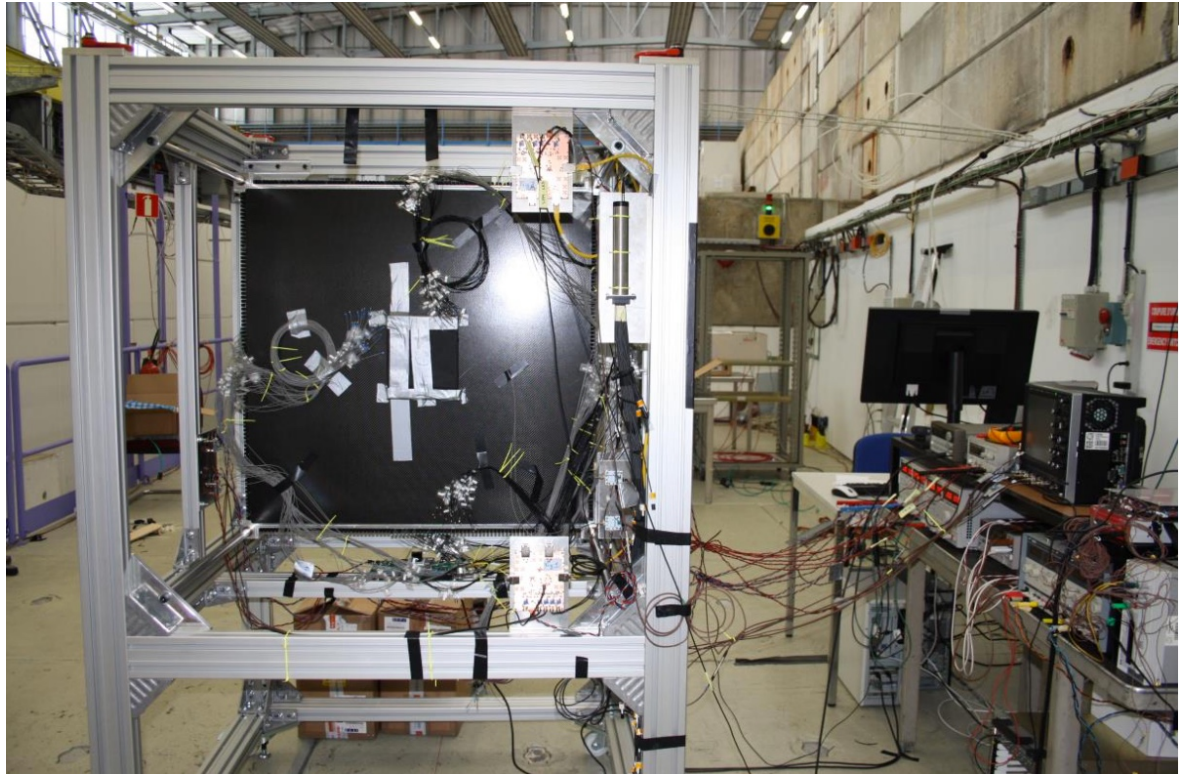


Figure 5.2: The TASD at the PS with the readout PC.

5.1.2 DAQ

Each MPPC is connected to a Front End Board (FEB) which returns data in a specific format. For the setup a full 4 FEBs were used each able to read 96 MPPC channels each. These FEBs were then all connected via USB3 to a readout PC. The readout PC:s are controlled via remote connection/ethernet by a computer outside of the beam area in the control room. The data is currently just recorded, thus all analysis needs to be handled offline. This is both consequences of the data format design and the complexity of unpacking the data.

This data is sent from each of the FEBs in a custom made data format. The data format simplifies combining the data from all of the FEBs, however it only works for offline processing as the footers need to be read before any processing can be done.

When this is done an unpacking software is used to translate the format to actual usable data and hits. During the first test beam conversion between channel and position was hard coded, this was later changed to a database.

5.1.3 Data preprocessing

The data recorded by the DAQ is translated using a database relating the channel number directly to a relative position for the bar as well as passing on the time of the hit. For this

initial test beam there was no conversion possible between signal to deposited energy.

It was possible for the DAQ to return hits without a time which were removed before the analysis, also events which were to large time outside of the initial hit were removed.

5.1.4 Results

The main goal of this first test beam was to test the readout system, electronics, DAQ and reconstruction software. The results can be quite nicely summed up in figure 5.3 and figure 5.4 and noting that the TASD was horizontally aligned but the beam was slightly off-center vertically. Detailed studies of the electronics were performed and published in [90].

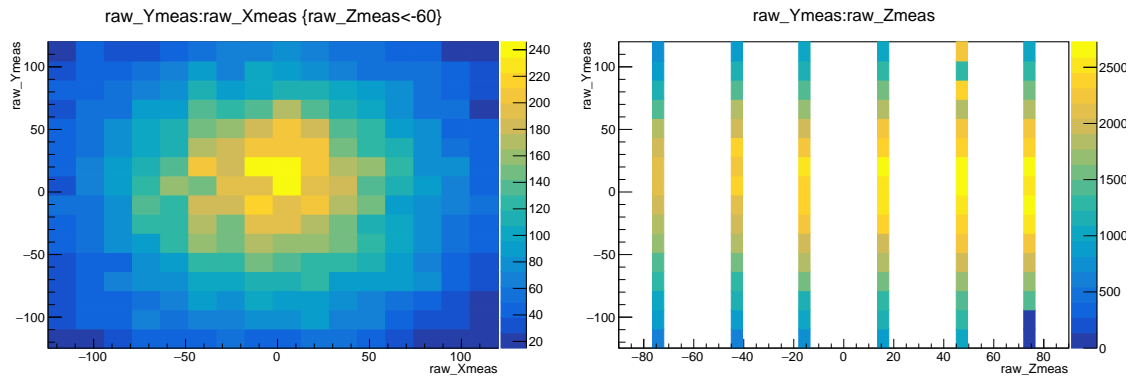


Figure 5.3: (Left) An XY-beam profile as measured by the TASD. (Right) An YZ-beam profile as measured by the TASD

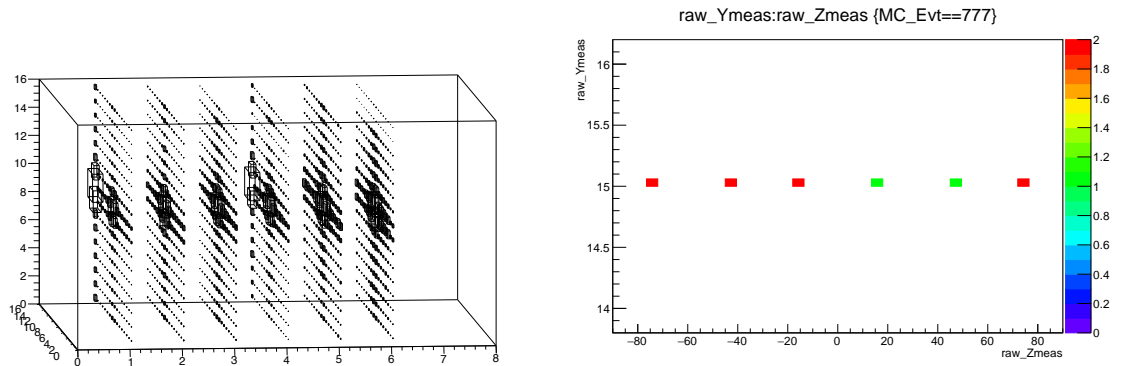


Figure 5.4: (Left) 3D-Beam profile measured by the TASD. (Right) Single muon track passing through the detector.

The plots show both that the electronics and readout system works well, and that the data can be passed through the DAQ into the reconstruction software. Given that the TASD was only 6 planes of scintillator and did not have a magnetic field, the reconstruction software only combined hits in x and y with the z position to a final track, without being able to perform any momentum reconstruction. However it showed that the reconstruction software was operational and could create tracks from these hits.

5.2 MIND-test beam

The Baby MIND qualification took place at the T9 beam line at the PS experimental hall (East Area), during June - July 2017. The beam lines are derived from the 24 GeV/c primary proton beam from the PS, which provides 2.4 s cycles of about 400 ms spill duration. The T9 beam is a secondary beam from the collision of the proton beam with a 200 mm thick Aluminium target, that delivers secondary particles up to 15 GeV/c at a production angle of 0 degrees. The line is designed to provide the users with non-separated secondary particles, with positive or negative polarity. Users can adjust the beam momentum by setting the currents for the optical magnets of the beam line. A sketch of the layout can be seen in figure 5.5 and a photograph in figure 5.6.

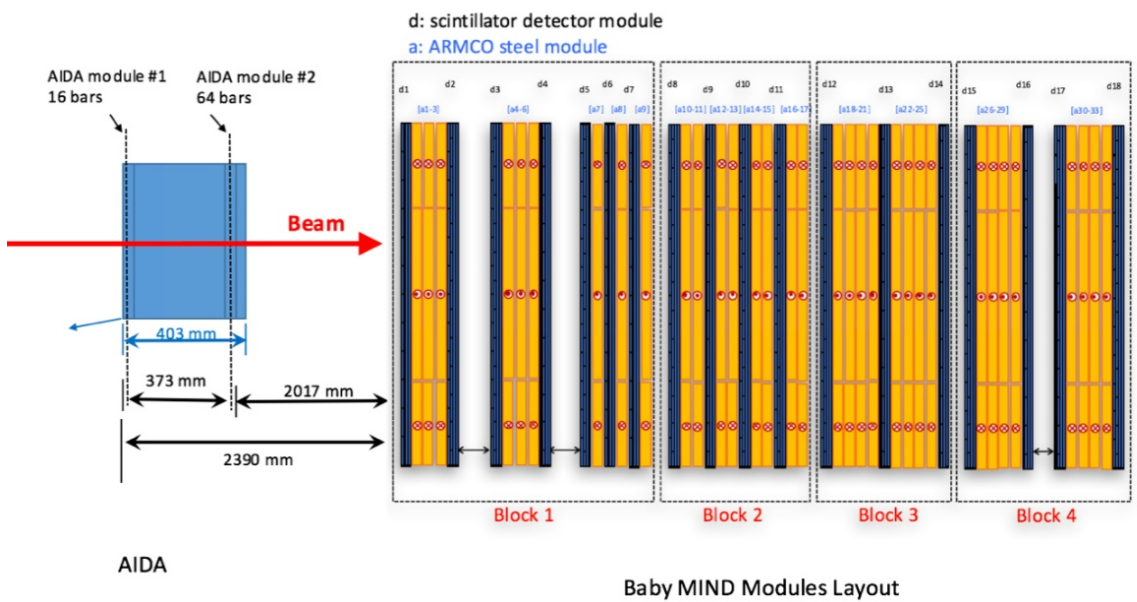


Figure 5.5: MIND in testbeam.

5.2.1 Setup

In order to support the magnets and scintillating modules mechanically, four support frames were constructed specifically to support the Baby MIND and to meet the transport requirements within CERN and shipping to J-PARC. The Baby Mind modules were installed in the four frames. The total weight of the detector is around 65 t giving each block a weight of at less than 20 tons which is within the required limits for crane operations at both sites.

For the data taking during the test beam, the TASD was placed in front of the Baby MIND to provide initial beam information, both an angular measurement of the beam and a veto

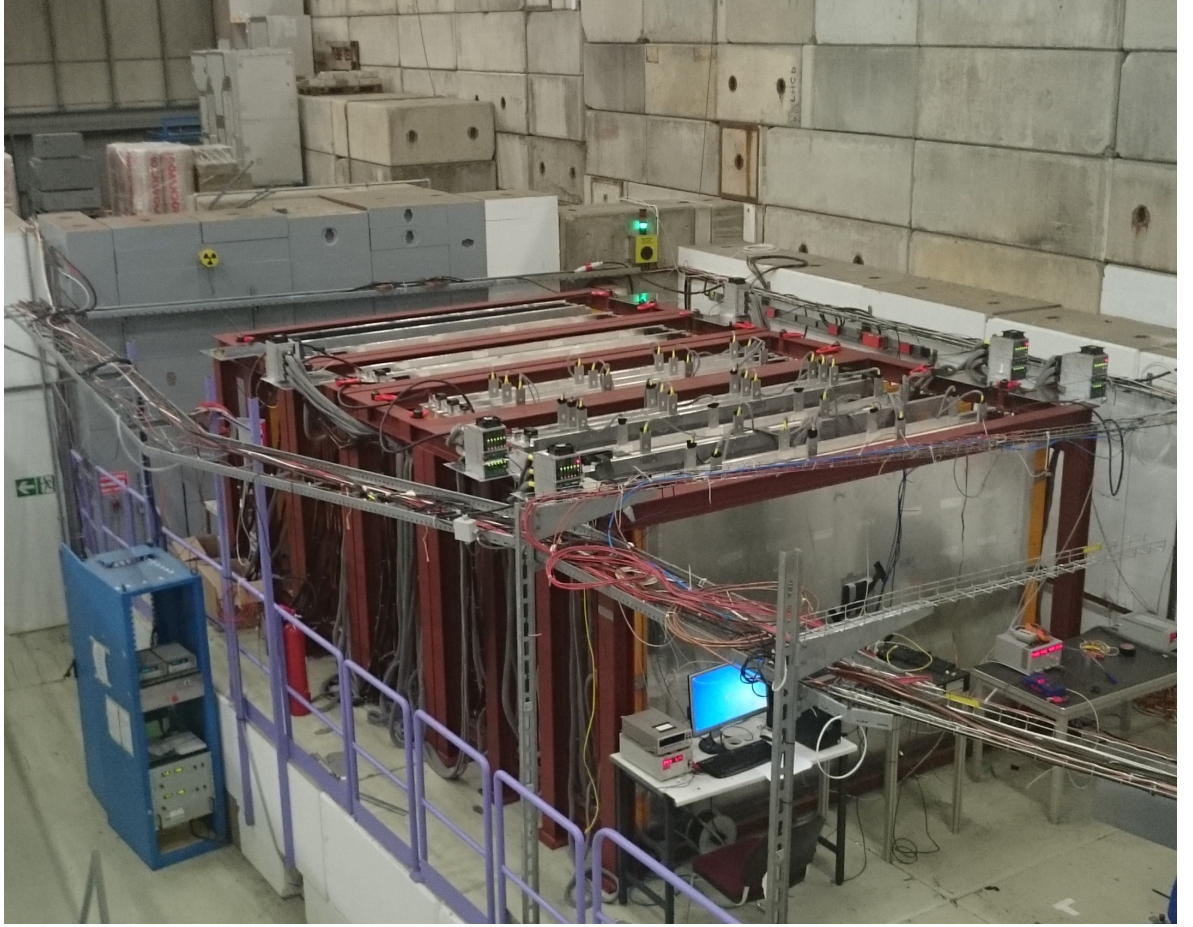


Figure 5.6: MIND in testbeam photo.

measurement from cosmic rays. Only a total of 2 planes of the TASD were instrumented providing 192 channels.

A total of 44 FEBs mounted on 8 mini crates instrumented the 3996 channels of Baby MIND and took the 192 channels from the TASD. All 44 FEBs were synchronized using the spill signal from T9 beam line which arrives one second before the arrival of the spill of particles. This signal was fed to a dedicated Master FEB which would generate a reference clock signal for all the other FEBs acquiring data.

5.2.2 Data preprocessing

The data recorded by the DAQ is translated using a database relating the channel number directly to a relative position for the bar as well as passing on the time of the hit. For this initial test beam there was no conversion possible between signal to deposited energy.

It was possible for the DAQ to return hits without a time which were removed before the analysis. And also events which were to large time outside of the initial hit were removed.

For this test beam initial filters were used to try to remove possible pion contamination such

as removing events where on average more than three hits were recorded for the same plane for an event.

Data was taken for a period of 2 months. Out of the recorded data, a verified samples with the best possible settings for the data acquisition was selected for analysis. The samples contained a few hours worth of data taking at different beam momenta for both muons and anti-muons beam settings. These samples were all run through the unpacking software required to read out the recorded data before being passed to SaRoMaN. The data was passed directly into the digitisation for clustering and grouping before being passed into the reconstruction..

5.2.3 Analysis

For the first part of the analysis the data sample was assumed to be quite clean, containing mostly only muons or anti-muons. To remove any contribution from outside of the beam the hits in the TASD were used as a beam trigger to defined a time window of interest from this time and 125 ns after and used to fit any tracks. This time was chosen after seeing what was appropriate for our data structure. To remove any potential showers or noise any event less than 4 hits in MIND or on average more than 10 hits per plane were removed.

Data was run through the SaRoMaN software framework and produced plots of charge reconstruction efficiency, momentum reconstruction etc etc and compared to simulations.

In the analysis it was also quite clear that the beam was not pure muons and contained some contamination of other particles. The main contamination seems to be pions. Thus for the second analysis the data was firstly run through a TMVA software packages providing many different machine learning techniques which would perform the particle identification of muons vs pions.

5.2.4 Results

Two of the main results provided during the test beam were both to commission the detector by showing that all parts works, including the reconstruction framework with hits in all of the modules, and magnetic field providing the ability to estimate momentum. Results will be presented showing that the detector has been commissioned and showing that the reconstruction framework can read in this data and produce charge and momentum estimates for the beam.

5.2.4.1 Electronics results

Gain plots for all of the 3996 MPPCs installed on Baby MIND. The gain is evenly distributed around 45 ADC/photoelectrons ± 5 as seen in figure 5.7. This can be further improved by optimising the pre-amp gain on the FEB for each of the MPPCs.

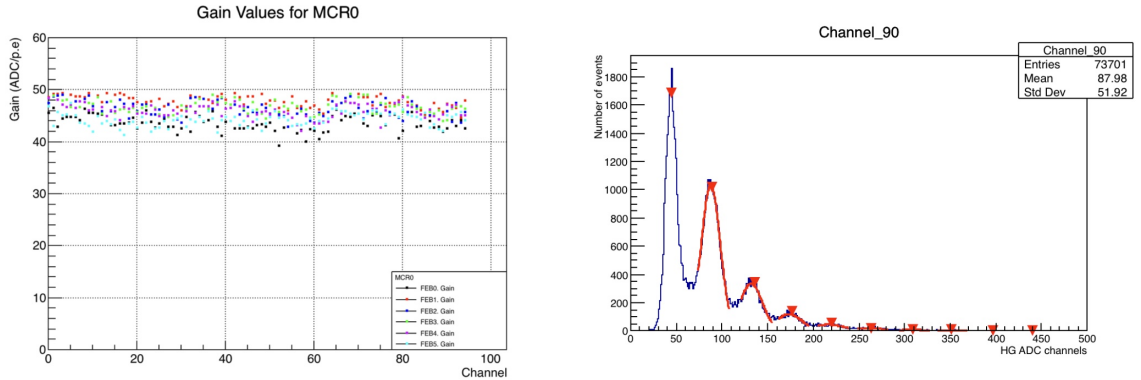


Figure 5.7: Gain for 576 channels (left) and noise spectrum finger plots with 5 viable peaks. for one channel (right).

5.2.4.2 Magnet results

The magnet performance was measured at CERN, with detailed tests on the first module allowing comparisons verification of simulations. The magnet modules reached the design specification of 1.5 T for a current of 140 A. Stray fields were measured at < 10 mT at a distance of 1 mm from the surface of the magnet modules. The measured power consumption at CERN was 11.5 kW. The current and voltage reach stable operating values several hours, this can be seen in figure 5.8.

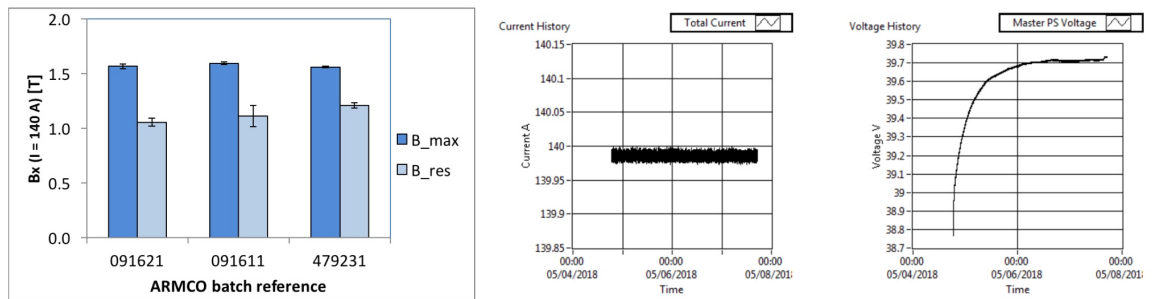


Figure 5.8: Baby MIND magnet measured (at CERN) field values for 33 modules (left), current at J-PARC (middle) and corresponding voltage (right).

5.2.4.3 Hits in SaRoMaN

Using the recorded data, the SaRoMaN needed to be verified to see if it could combine the bar data into 3D space points. As can be seen in figure 5.9 the planes show up well with no obvious missing hits and a similar filling of hits on all planes.

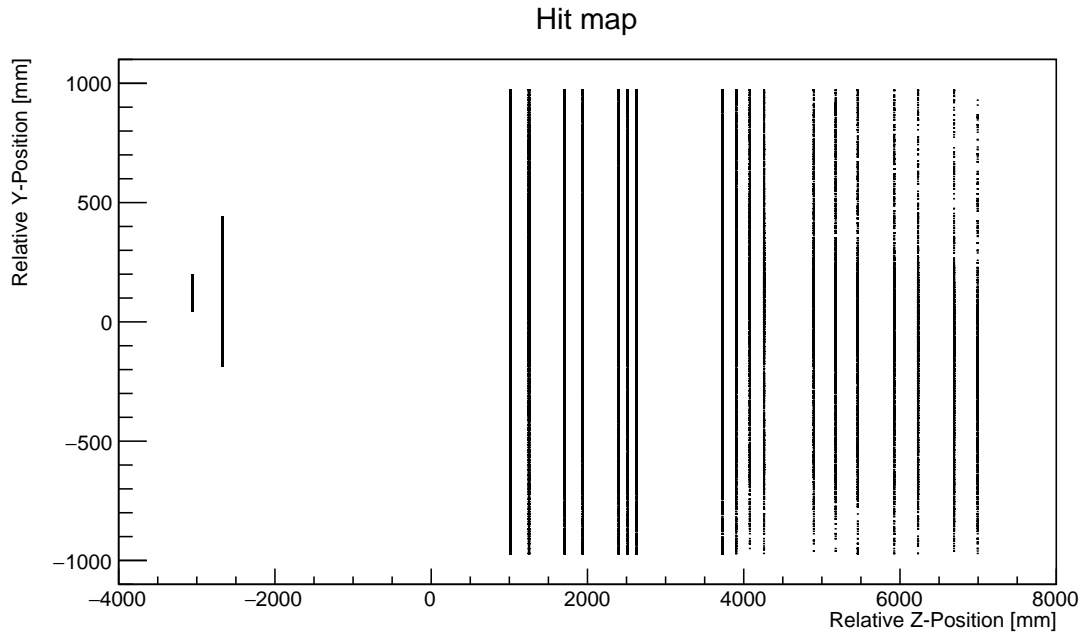


Figure 5.9: All recorded hits for a run with the 5 GeV beam settings.

5.2.4.4 Tracks in SaRoMaN

In a similar way to simulated data, the collected hits are split depending on the time the hits were recorded to build possible tracks, seen in figure 5.10 and figure 5.11. Each of these possible tracks are then filtered through to produce the best possible fitted track for those points and some background or noise hits. This can become quite complicated if there are two tracks passing through simultaneously, however this can be handled by the software even though this phenomena is rare.

The main difficulty comes from the framework only reconstructing tracks and discarding shower events. Any track reconstruction of a shower should fail, but sometimes it will try and return an incorrect charge and momentum value. This makes it clear that data of showers need to be removed before any analysis is performed by using pattern recognition to identify showers (non-muons) from muons (non-showers).

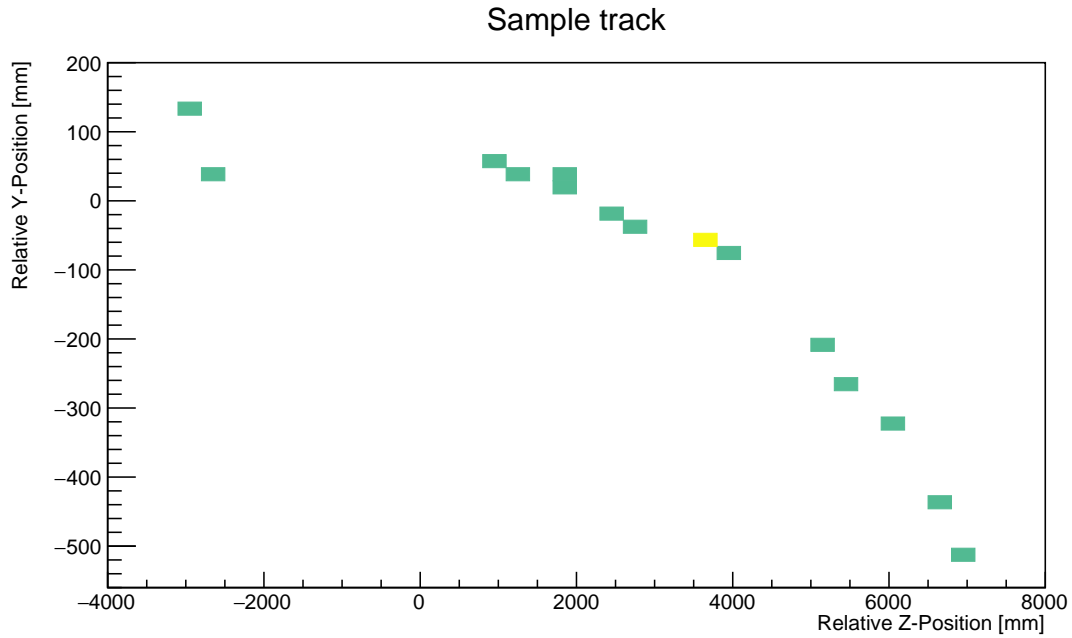


Figure 5.10: A sample track, taking a time cut for the hits for a run with the 5 GeV beam settings.

5.2.4.5 Charge identification efficiency

One of the main goals of the Baby MIND detector is to correctly identify the charge of incoming muons. In the test beam it is difficult to estimate the number of muons produced since the beam itself is a mix of mostly muons and pions. As seen above, the reconstruction software can return the number of tracklike events against the number of reconstructible tracks. With these reconstructible tracks the charge can then be reconstructed and a charge identification efficiency plotted as seen in figure 5.12. Initial results of this study were shown at NuFact2017 and published in [104].

These plots confirm that the full data analysis chain works however the results are slightly less than expected from simulations. Looking on an event by event basis it become clear that the events are a mix of muons and pions even after an initial pattern recognition. This motivated the development of a more advanced pattern recognition algorithm using machine learning. It can be seen that a simulated pion sample, figure 5.13, will be very poorly reconstructed and can explain the difference between data and simulation in the mixed test beam.

It should be mentioned that for future runs the deposited energy will be available and will make the distinction between pion and muon easier.

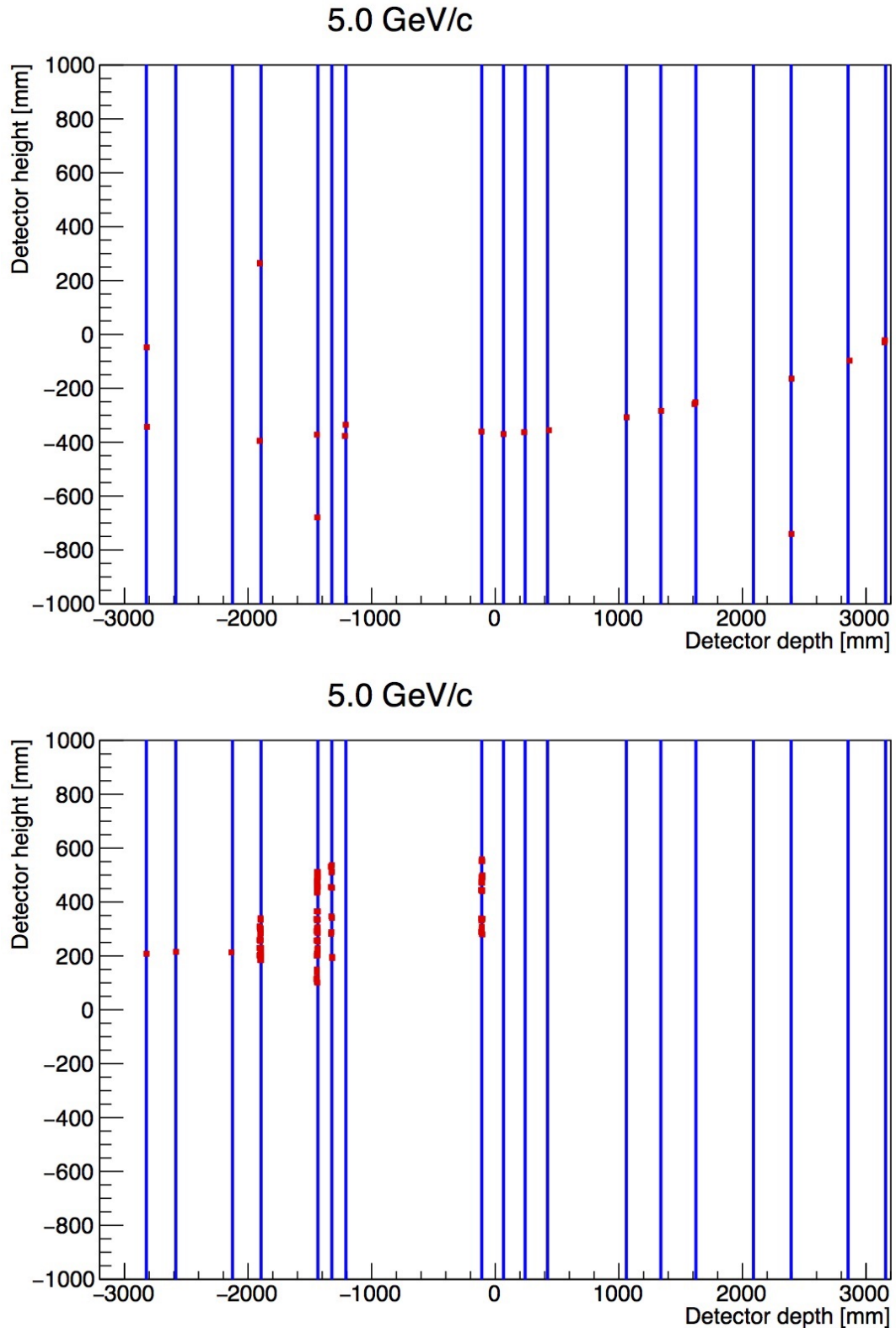


Figure 5.11: Sample events of test beam interactions at a set energy value of $5\text{GeV}/c$.

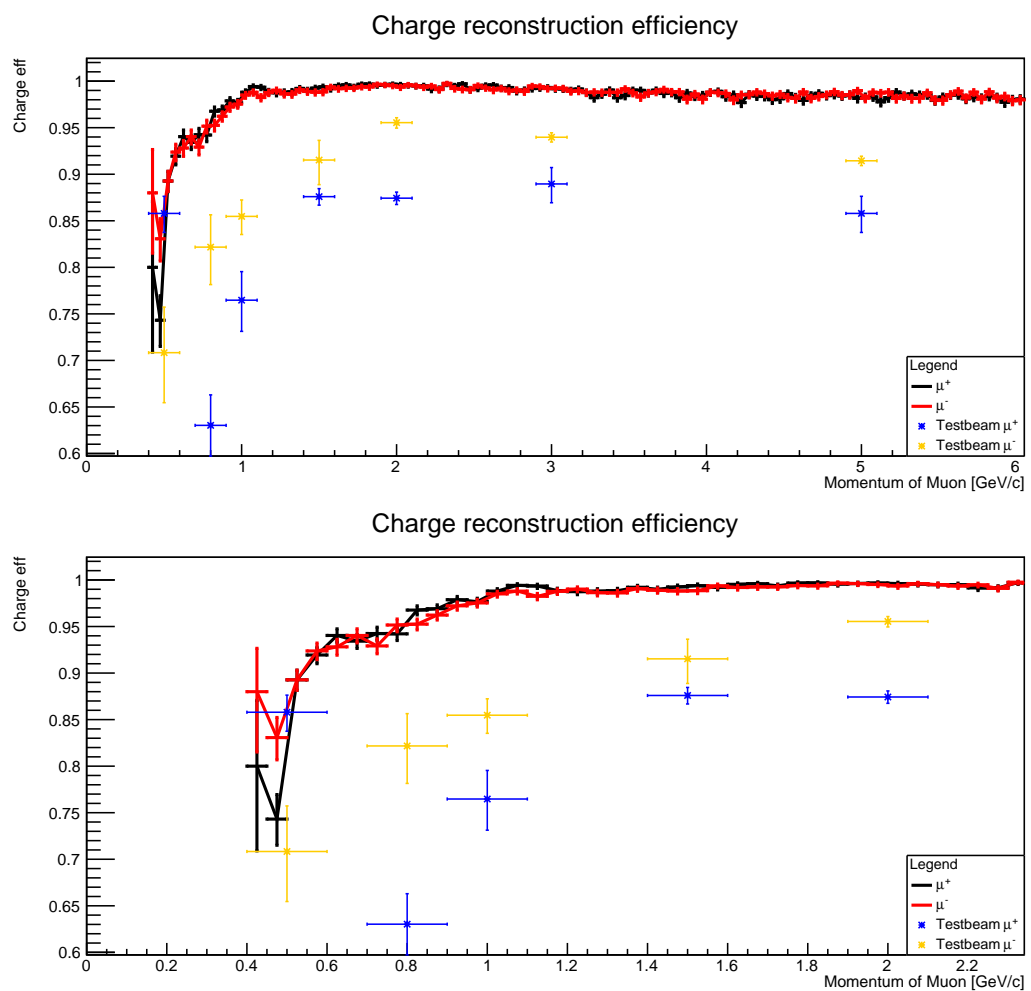


Figure 5.12: Initial charge id results

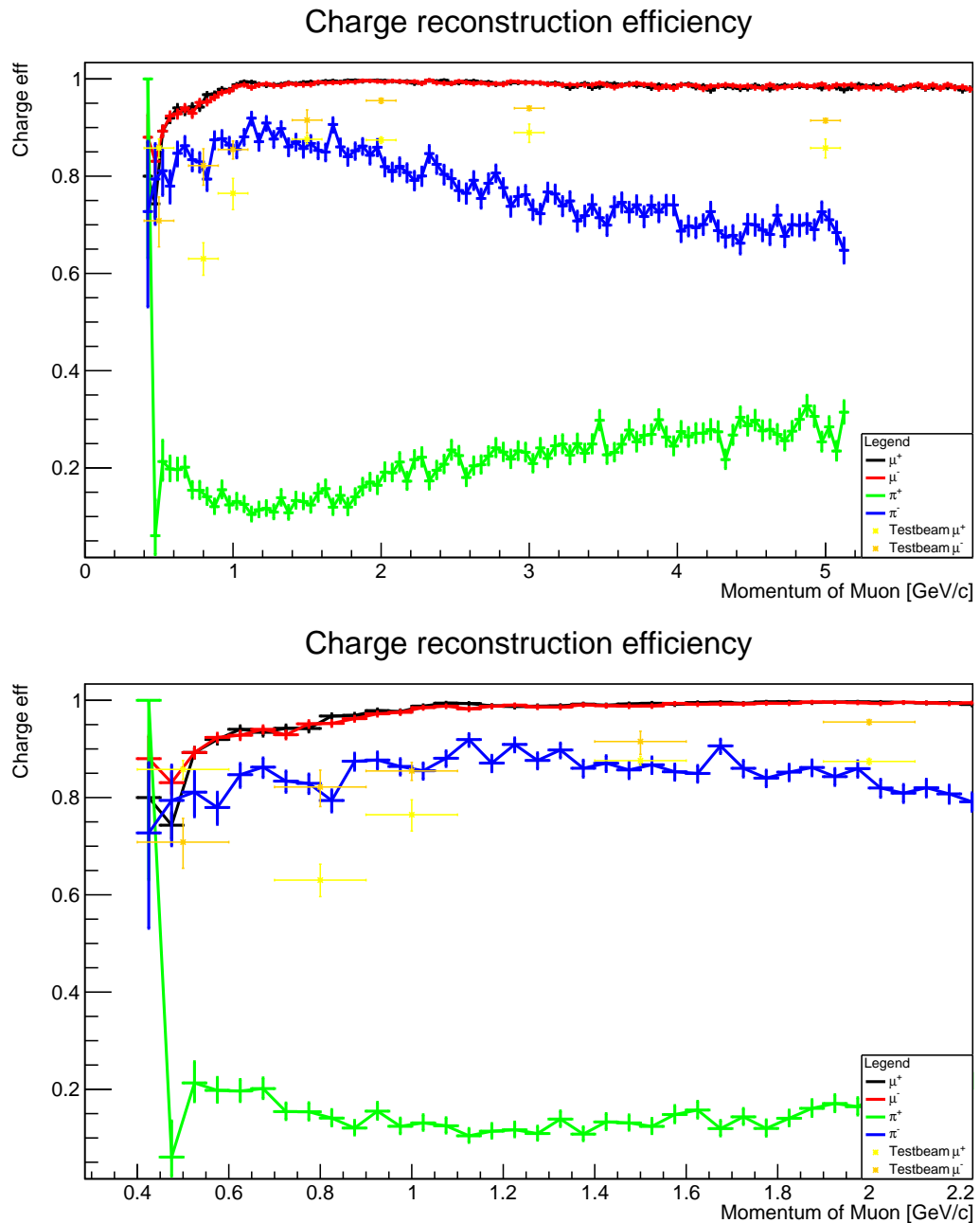


Figure 5.13: Simulated charge id for different particles vs data points

5.2.4.6 Particle identification

To further charge reconstruction, a particle identification algorithm was developed using TMVA [99] to classify muon from other events which may still pass through harsh criteria. The model has been developed to not be dependent on the momentum of the particle, should work for full range.

Essentially the machine learning algorithm identifies muons in a mixed background, but does not identify any particles in the background. This could be a future study and could be used to identify pions as well. In a more formal structure the signal is muons and the background are all of the remaining particles in the beam such as pions, protons etc.

The main variables used in the model are the following:

- Number of total hits in the event
- Number of used planes for fit
- Number of hits used for fit/ number of used planes
- Average number of hits per plane
- Maximum distance between hits in an event / Naive track length

These variables can be seen in figure 5.14.

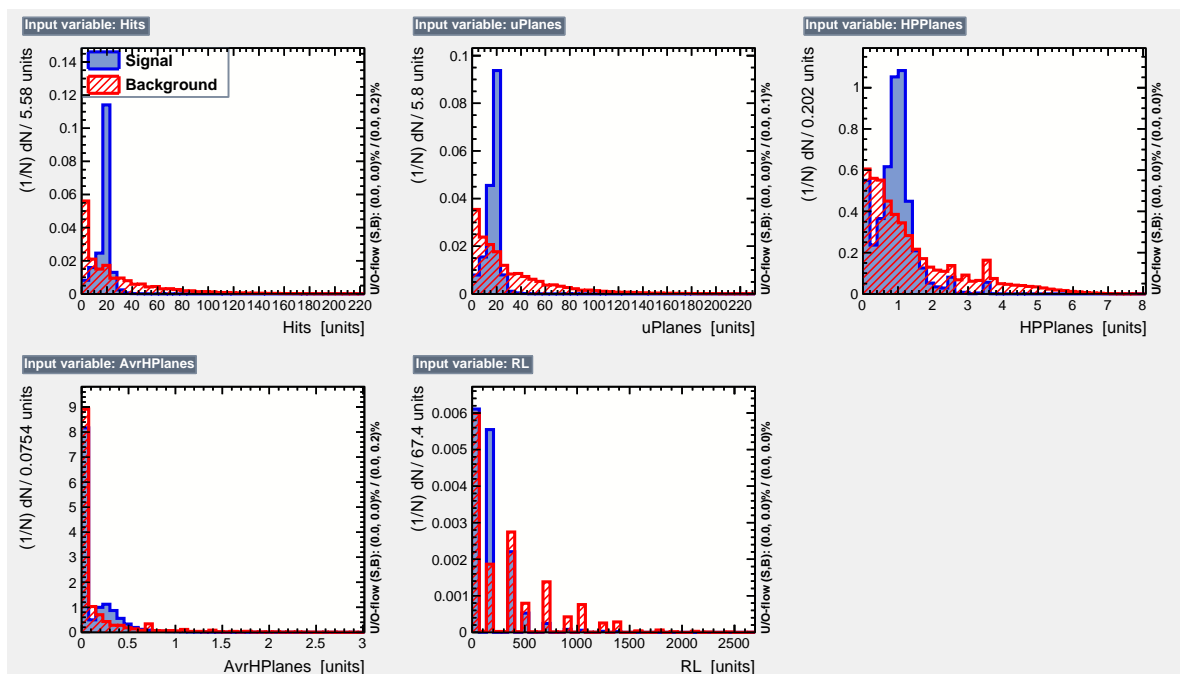


Figure 5.14: Input variables for both signal and background using simulated data

Based on these simulated signal and background samples, TMVA will provide a Signal efficiency curve based on the various built-in models, seen in figure 5.15. In this plot it is clear that several models outperform others, however the multilayer perceptron with a Bayesian Neural Network (MLPBNN) was chosen as the best performing model. The specific performance can be seen in figure 5.16.

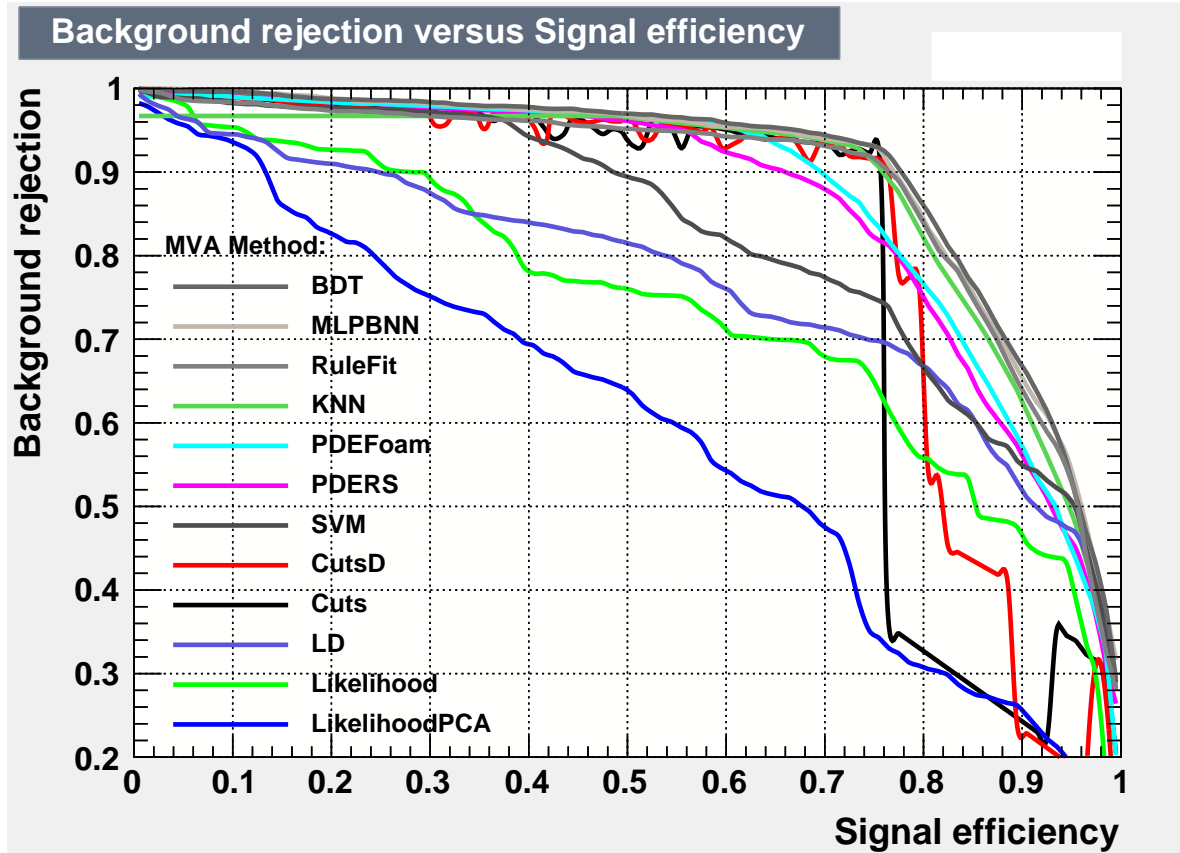


Figure 5.15: ROC curve for various machine learning algorithms.

Running through this model further it is possible to return the evaluation variable, known as the response to see how signal and background are classified by TMVA. Figure 5.17 shows that signal and background can be separated and is understood by the algorithm, however there will always be some events which are incorrectly classified as signal or background. In the same figure it can be seen how data points have been added both by the training and testing sample to show that the algorithm has not been over-trained to work for only specific data.

This translates directly into figure 5.18 showing what value the response should be used to determine what is signal and background, providing a specific purity, efficiency and significance. For this analysis purity is of the most interest as the end goal is to return a data sample with as clean a muon sample as possible.

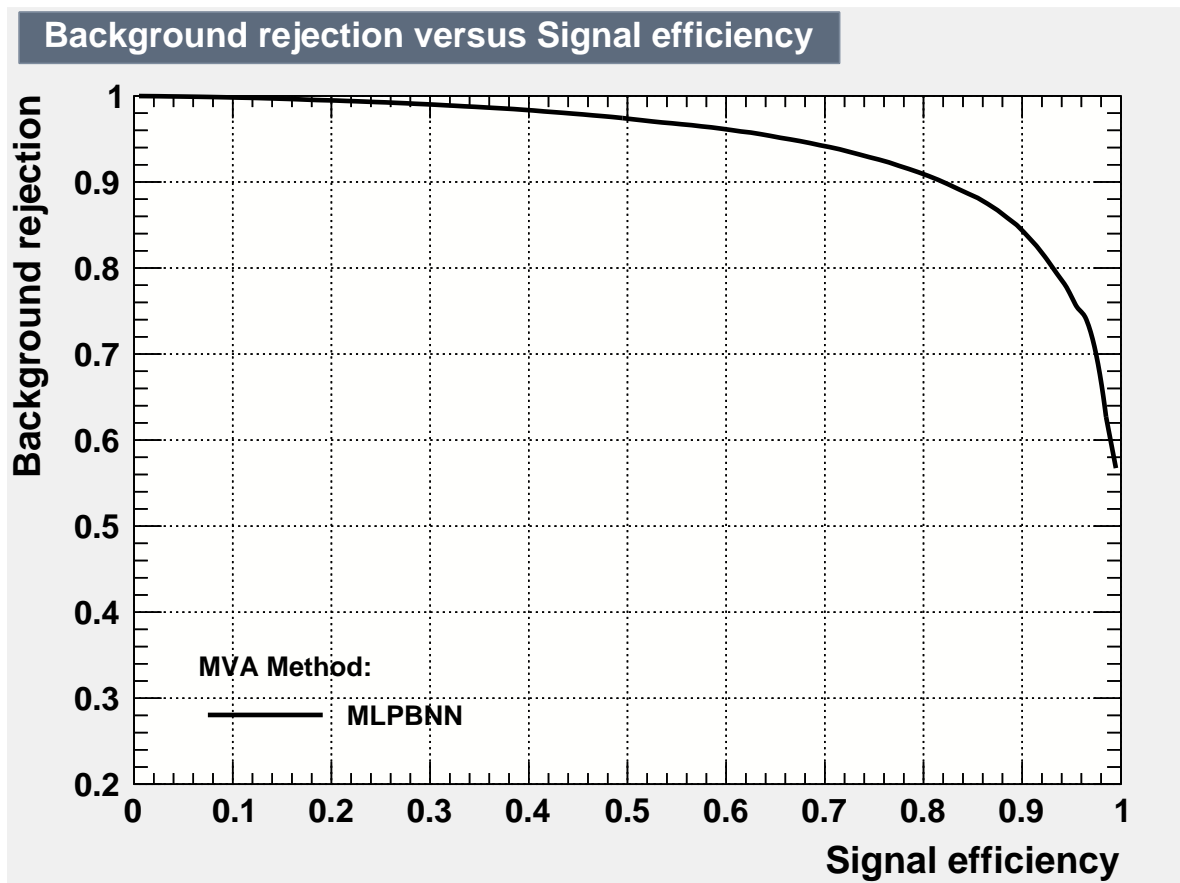


Figure 5.16: ROC curve for the chosen machine learning algorithms.

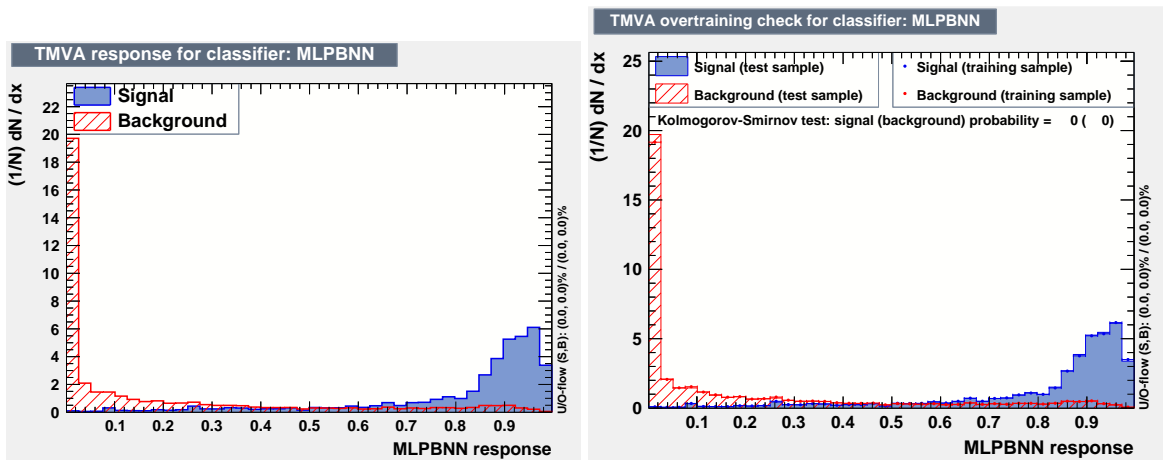


Figure 5.17: Response with and without over-training check

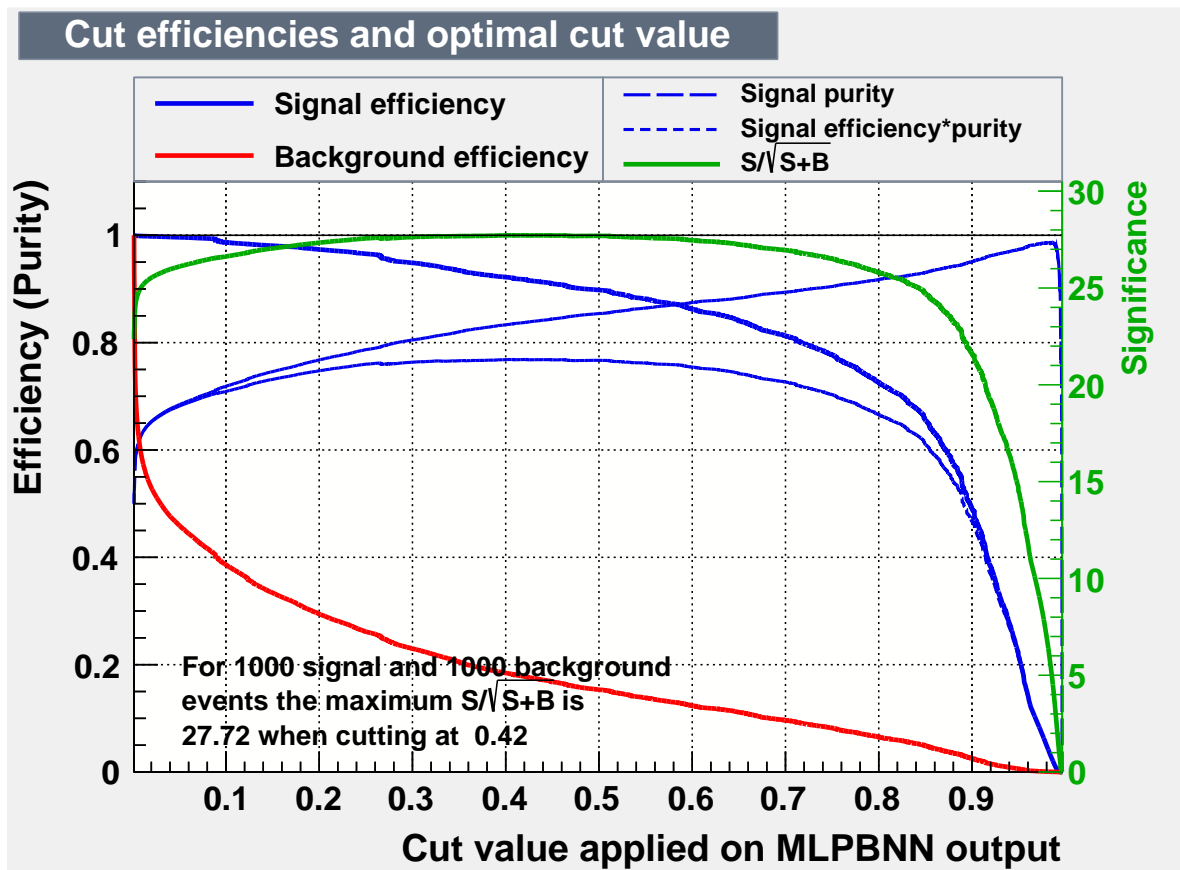


Figure 5.18: Cut efficiency plots.

5.2.4.7 Updated charge identification efficiency

Using the final cleaned sample provides the final charge estimates as seen in figure 5.19.

This finally shows, that assuming the beam after this is sufficiently pure there is a discrepancy between the simulations and final data representing detector and electronics factors which have not been taken into account. It should also be noted that the momentum values for the data are taken as the momenta selection set by the quadrupole magnets in the beam, which may not have been at the correct momentum value. This will require further study and potentially simulations of the entire beamline.

The plots show the potential of using a MIND type detector for muon charge reconstruction at lower momenta than previously thought. It also shows that for the test beam it was possible of attaining above 70% charge identification for the full momentum range and above 85% for muons above 1 GeV/c.

5.3 Summary

From the test beam it is clear that the Baby MIND performs as expected. The electronics works as well as the reconstruction in SaRoMaN, showing that charge identification is possible for muons at low momentum. The results show that the collaboration is ready to be integrated into the WAGASCI experiment for some neutrino data taking.

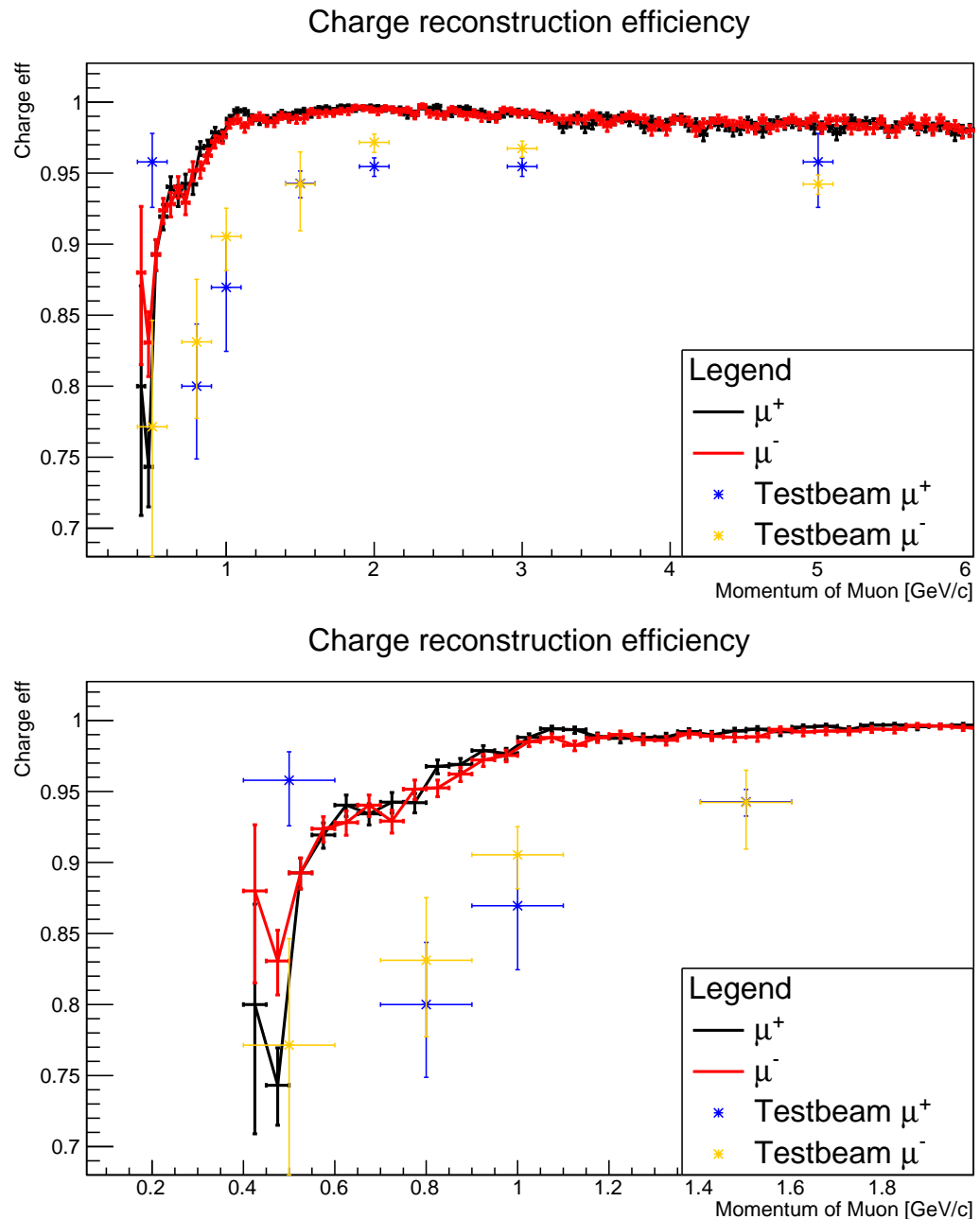


Figure 5.19: After TMVA charge id results

Chapter 6

Neutrino interaction studies

The Baby MIND is build to reconstruct muon tracks passing through the detector. This makes it ideal to be used for muon neutrino reconstruction with an appropriate target. As discussed in subsection 1.4 there are only a few interactions which produce a free muon which can then be reconstructed with the Baby MIND. These are the muon neutrino charge current interactions, quasi-elastic charge current interactions, deep inelastic scattering and resonant interactions each at various energy ranges as can be seen in figure 6.1

The signature for each of these interactions are quite different as a charge-current quasi-elastic interaction will produce a clean proton and muon track, compared to a shower like pion track or the less clear DIS signature. Baby MIND is designed to operate at a lower energy spectrum, below 5 GeV, meaning that the contribution will be mostly from CCQE and pion interactions. Results from various simulations with the T2K near detector beam spectrum and data recorded from the commissioning will be showed.

6.1 Muon charge current quasi-elastic

CCQE interactions produce a clear muon track for both neutrinos and anti-neutrinos, however the interaction only produces a proton track for neutrino interactions as seen below:



For the neutrino interactions, this becomes a very clear signature in a fully active target where both a muon and proton track can be identified. For anti-neutrinos this is not possible since neutron tracks are usually not detectable for most detector types. However the main goal is to identify muon tracks from pion tracks which is simply identifying a shower from a

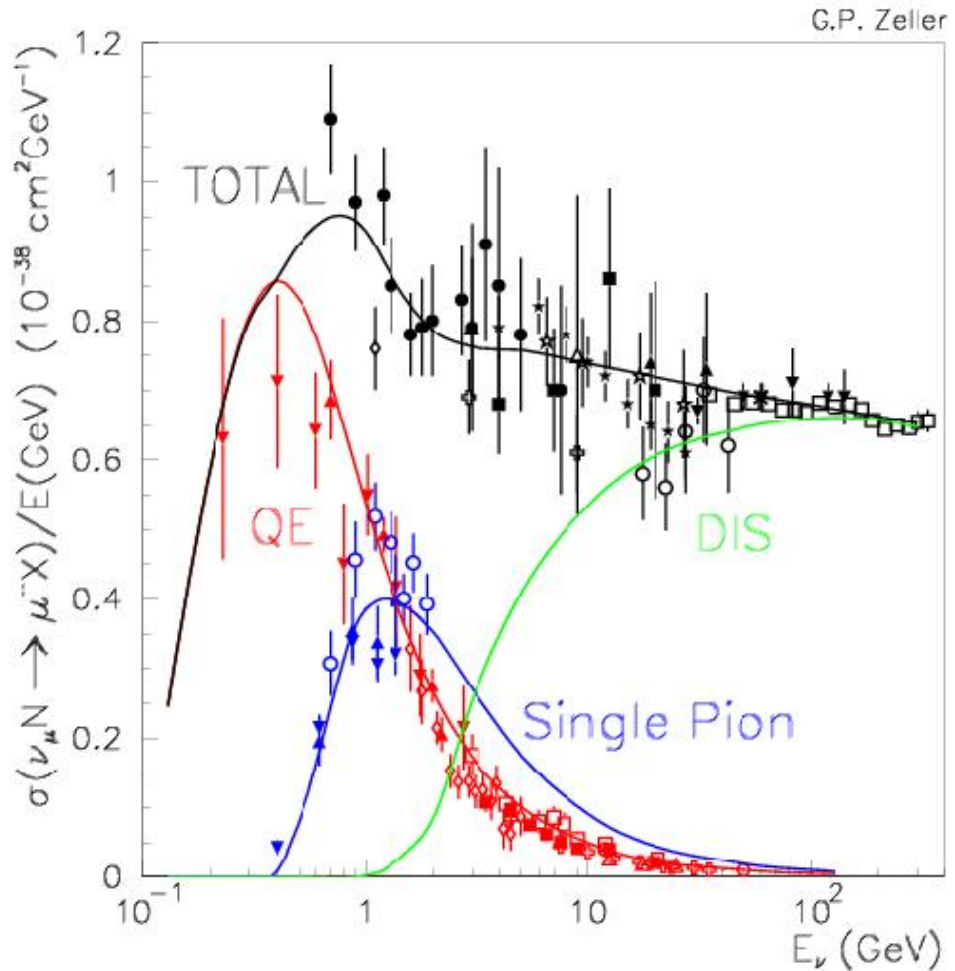


Figure 6.1: Neutrino cross sections, showing the quasi-elastic, deep inelastic and single pion cross sections in the GeV range. Taken from [105] modified from original made by G.P. Zeller [12] containing data points from various experiments.

track. There have been a lot of interesting articles relating to how to identify neutrino events in Argon detectors using machine learning [102] [103]. In a non active target it becomes very difficult to identify neutrino interactions as pions may decay to muons and become indistinguishable from directly produced muons.

6.1.1 Interactions in TASD + Baby MIND (NuSTORM)

As described in subsection 2.7.1 a first stage towards a neutrino factory would contain a storage ring for neutrino and anti-neutrino production from muon decay. From a muon decay both muon and anti-electron neutrinos will be produced at $\approx 100\%$. In this study the TASD and Baby MIND has been used as a near detector to measure the interaction type and reconstruction of muon tracks. The main study is to see if it is possible to identify muon neutrino charge current quasi elastic (CCQE) interactions in a background of neutral current interactions and anti-electron charge current interactions. This is done using a TMVA trained algorithm with simulated samples. Part of this study also shows the fitted efficiency and charge identification efficiency of muon tracks in Baby MIND.

The NuSTORM neutrino energy spectrum has been simulated as can be seen in figure 6.2 for both muon and anti-electron neutrinos. The main job for any detector will be to identify if the neutrino event is produced from either a muon interaction or an electron interaction as well as dealing with the small background ($< 1\%$) of anti-muon produced electron and anti-muon neutrinos.

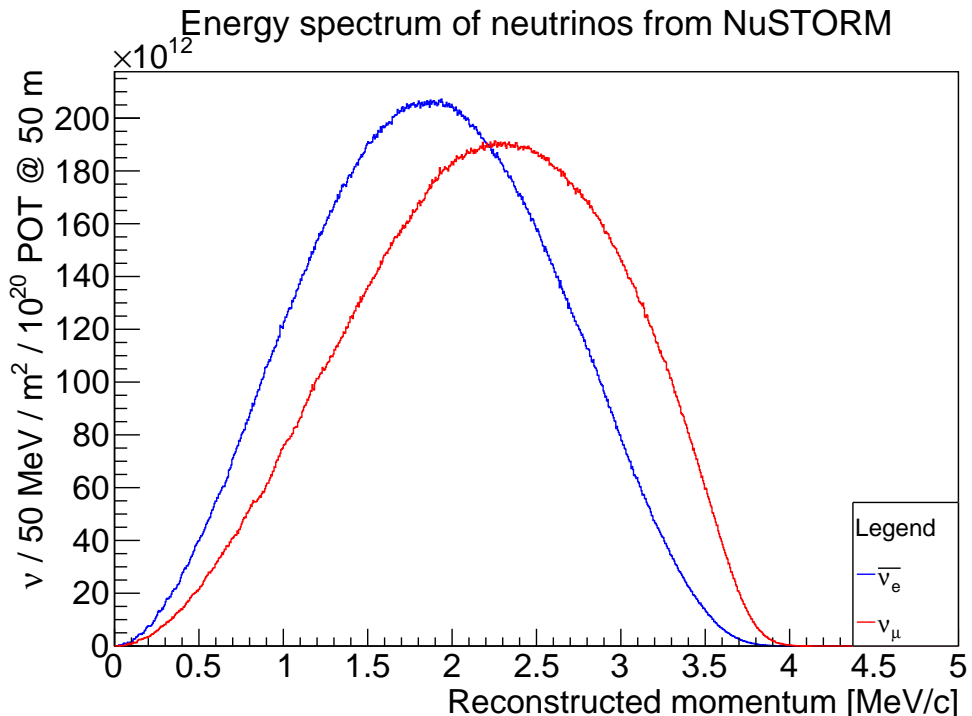


Figure 6.2: Energy spectrum of muon and anti-electron neutrinos produced at NuSTORM and recorded at 50 m from the storage ring.

During the construction of Baby MIND, it was proposed to potentially fully instrument the whole TASD, used during the first beam test, and use it as a fully active target to be combined with Baby MIND, illustrated in figure 6.3. This would become a setup for a NuSTORM detector.

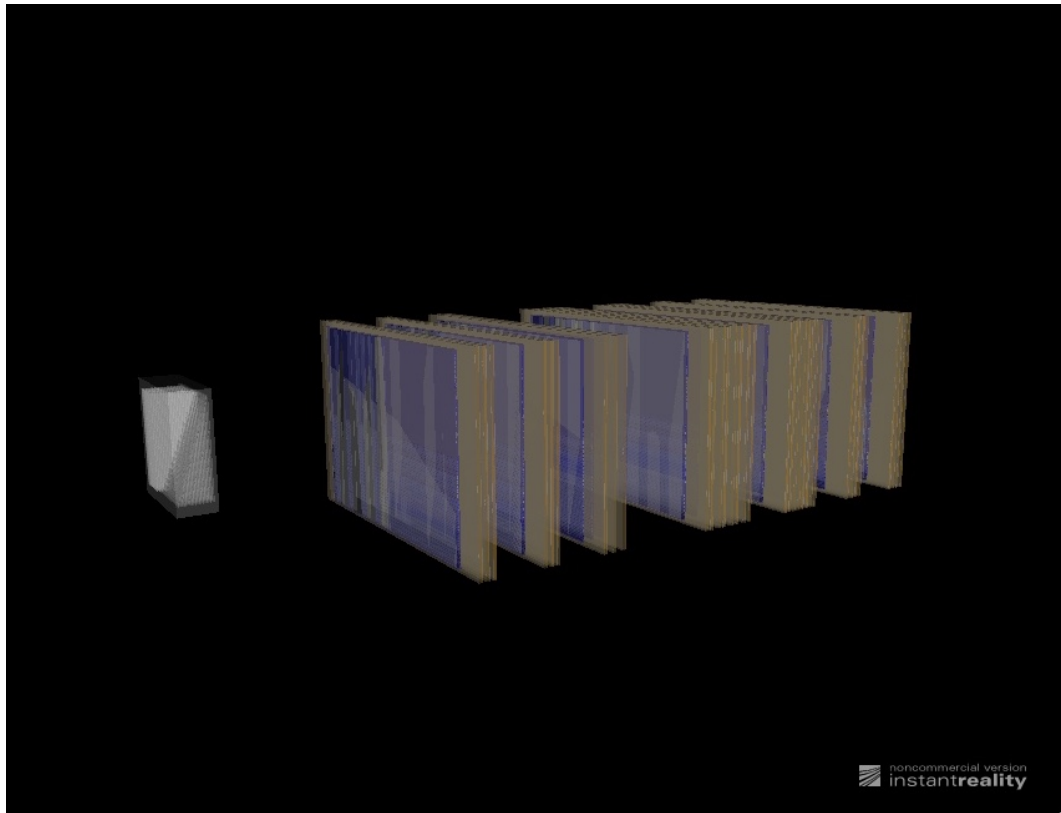


Figure 6.3: An illustrative sketch of the detector setup with the TASD detector in front of Baby MIND.

For the TMVA algorithm, similar variables to the muon, pion study for the test beam as to simplify the implementation.

The main variables used in the model are the following:

- Maximum distance between hits in an event / Naive track length
- Angle of the track compared to a straight line into the detector
- Number of total hits in the event
- Number of planes hit
- Average number of hits per plane

These variables can be seen in figure 6.4.

Based on these simulated signal and background samples, TMVA will provided a Signal efficiency curve based on the various build in models, seen in figure 6.5. In this plot is is clear that several models outperform others, however the multilayer perception with a Bayesian Neural Network (MLPBNN) was choose as the best performing model.

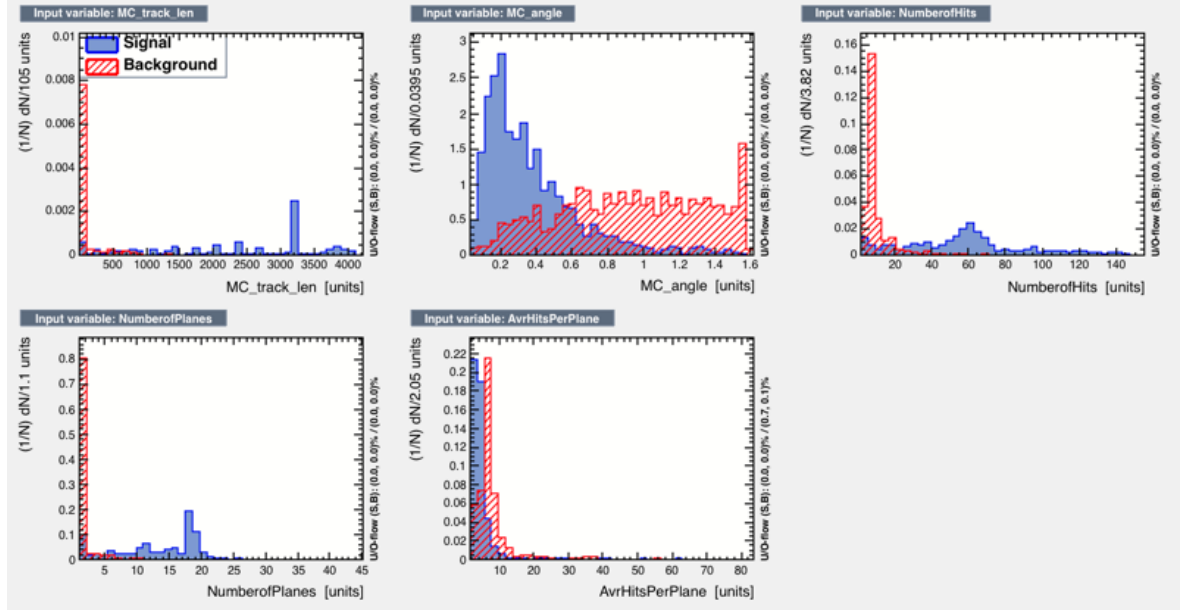


Figure 6.4: Input variables for both signal and background using simulated data

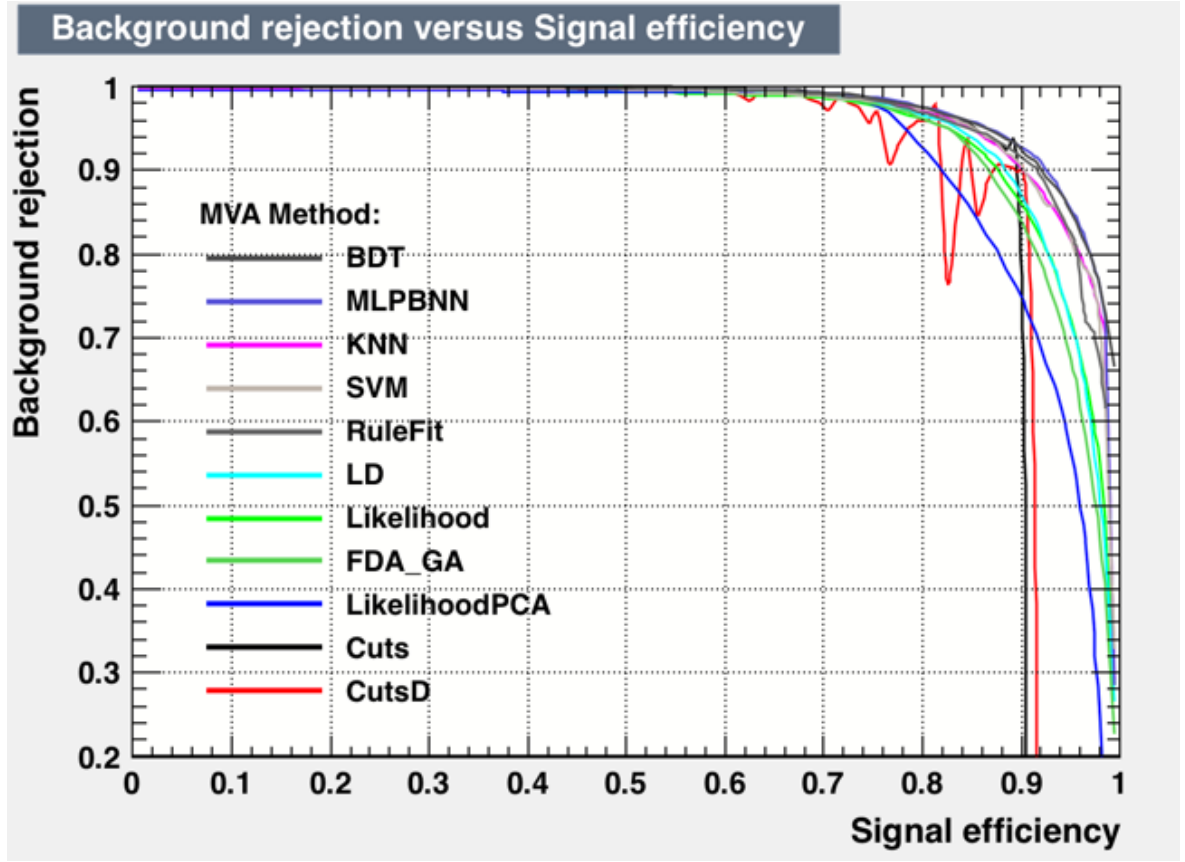


Figure 6.5: ROC curve for various machine learning algorithms.

With this trained algorithm the best possible cut value provides 91.3 % of the signal to pass through in a pure sample of signal events and only 0.08 % of background events in a pure background event sample. As with the previous study this is done independent of neutrino

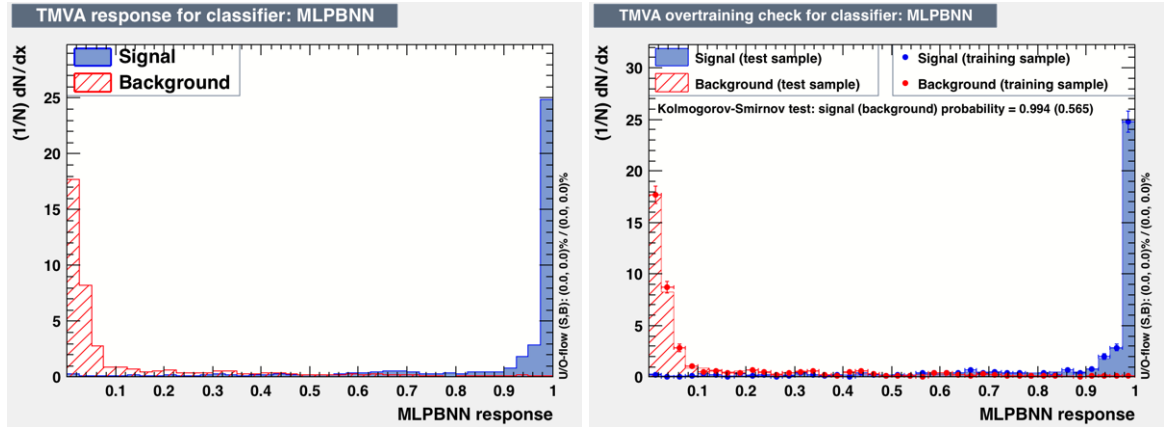


Figure 6.6: Response with and without over-training check

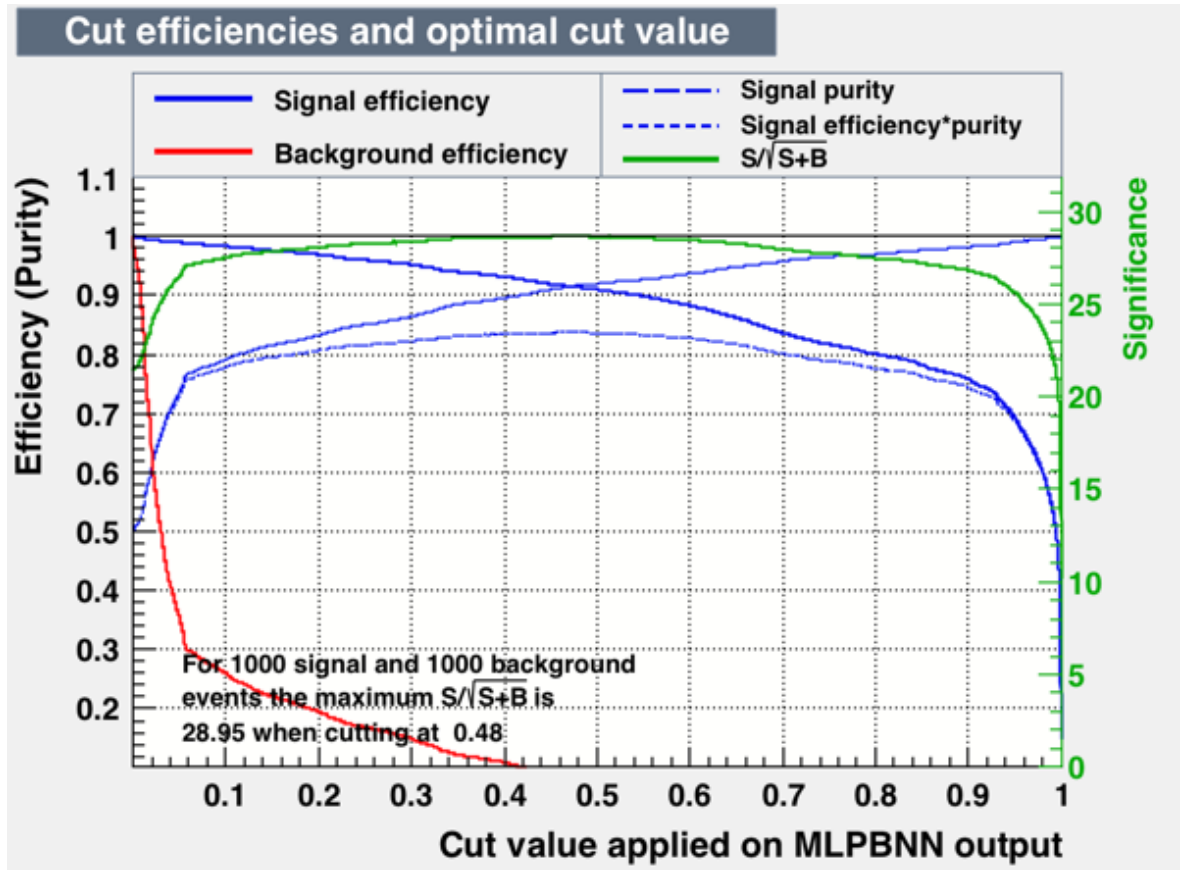


Figure 6.7: Cut efficiency plots.

energy values. This could be improved by looking at specific energy values and by looking at more variables to used such as perhaps energy deposited into the scintillating bars in the detector, however this would require a further study to determine better variable.

For all analysis the TASD is used as a CCQE identification and neutrino veto, expecting two tracks (neutrino) or atleast start of muon track. The dimentions are the same as mentioned under the test beam section, with a distance of 368mm between the two detectors. Neutrinos

are simulated using the T2K near detector spectrum in reverse horn current mode (RHC), seen in figure 6.8 in the SAURON framework.

In the framework several figures of merit are produced, the muon energy spectrum, reconstructed muon energy spectrum, reconstructability of tracks vs energy and charge reconstruction vs energy. All of these figures of merit are shown in figure 6.9 and figure 6.10.

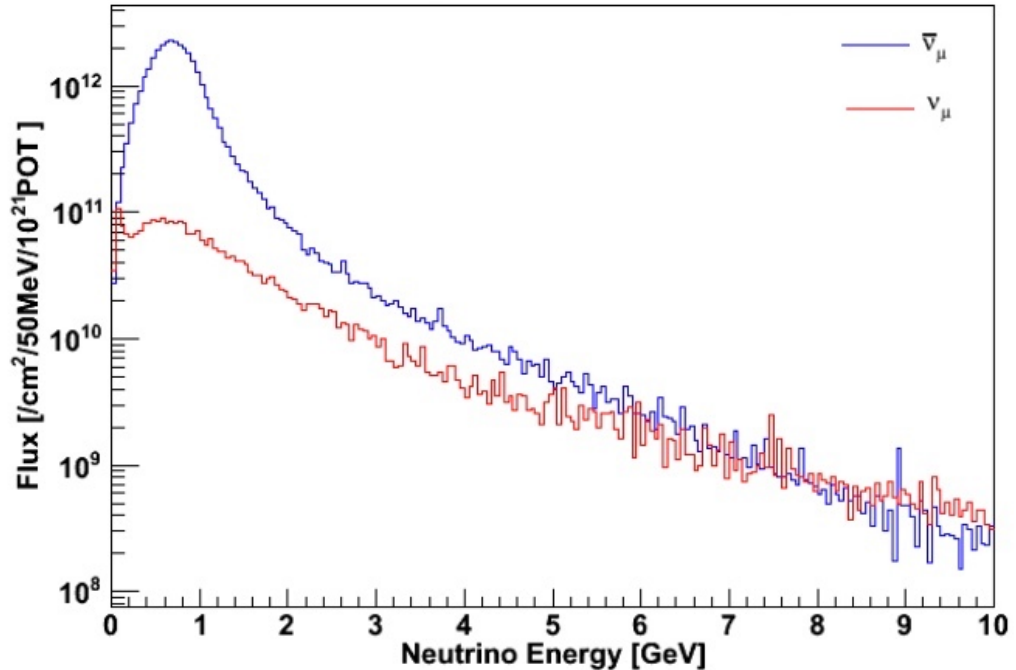


Figure 6.8: The energy spectrum for muon neutrinos and muon anti-neutrinos in the T2K near detector RHC beam.

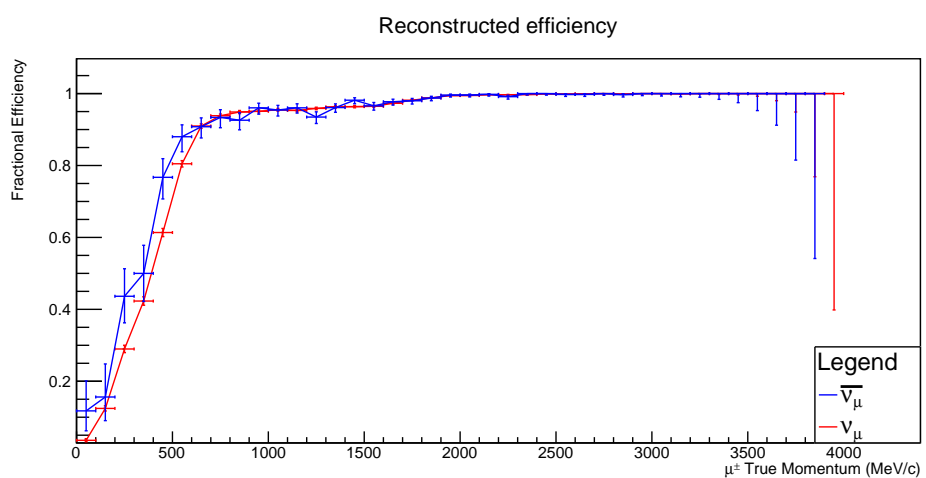


Figure 6.9: The efficiency plot of how well the algorithm can reconstruct neutrino tracks vs muon momenta for simulated tracks interacting in the TASD.

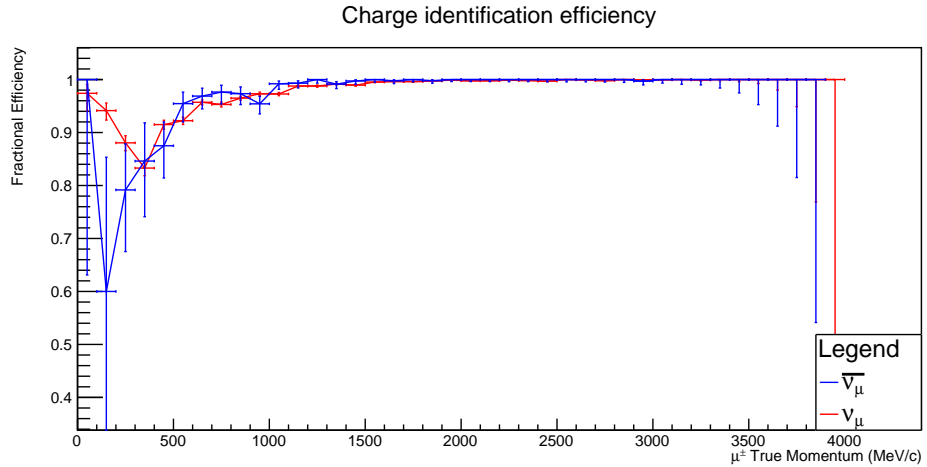


Figure 6.10: The efficiency plot of how well the algorithm can reconstruct muon charge vs muon momenta for tracks fitted in the algorithm.

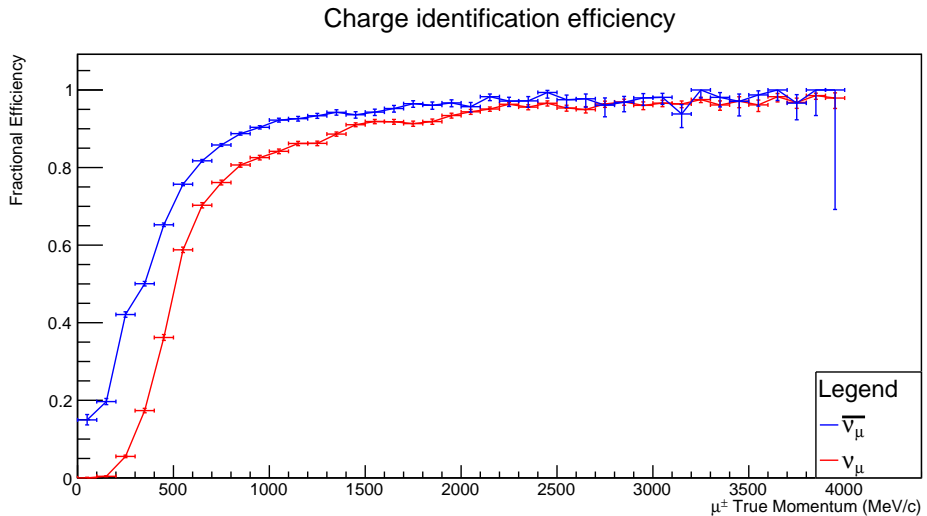


Figure 6.11: The efficiency plot of how well the algorithm can reconstruct muon charge vs muon momenta for simulated tracks. Combination of the previous two figures.

Similarly to the simulated muon beam, and data the charge reconstruction efficiency is very good for the reconstructable tracks. The difference comes from the fact that the neutrinos are produced at angles instead of straight on the center of the detector (with some beam size). Muons from neutrinos are produced at all angles depending on the kinematics of the neutrino interaction and neutrino energy.

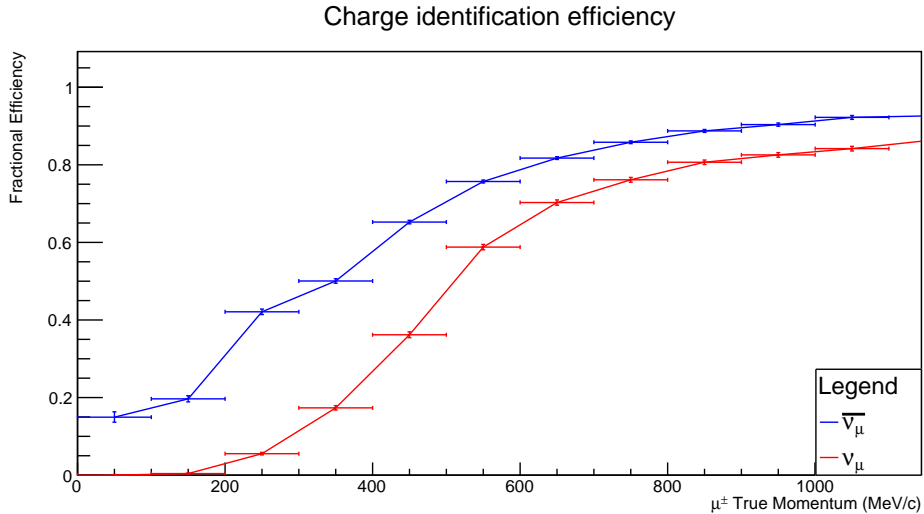


Figure 6.12: The efficiency plot of how well the algorithm can reconstruct muon charge vs muon momenta for simulated tracks zoomed in at the low momentum range.

6.1.2 Neutrino interactions in Iron in Baby MIND

Lead into expected momentum reconstruction? Potential for tracks to be miss constructed given angle etc etc. Even with cuts on no hit in first plate and hits after iron possible for sand muons to pass through. Tracks leaving would affect reconstruction. Angle and leaving, other than that is should be ok. Few events in total... Number of events sent to Paul, seems resonable.

Simulations for a T2K like beam, explain the details and event selection, (None for simulation but easy enough with data). Use the specific fiducial volume. Set up at J-PARC, all the details with that.

To compare simulations with data taken for the commissioning run interactions had to be simulated in the iron of the Baby MIND due to the fact that the WAGASCI data taking can as of yet not be joined with the Baby MIND data. The fiducial volume is chosen to be in the first iron module seen in figure 6.13 as a1-3 as well as selecting part of the iron plate, as seen with further details in figure 6.14.

In the framework several figures of merit are produced, the muon energy spectrum, reconstructed muon energy spectrum, reconstructability of tracks vs energy and charge reconstruction vs energy. All of these figures of merit are shown in figure 6.15 and figure 6.16.

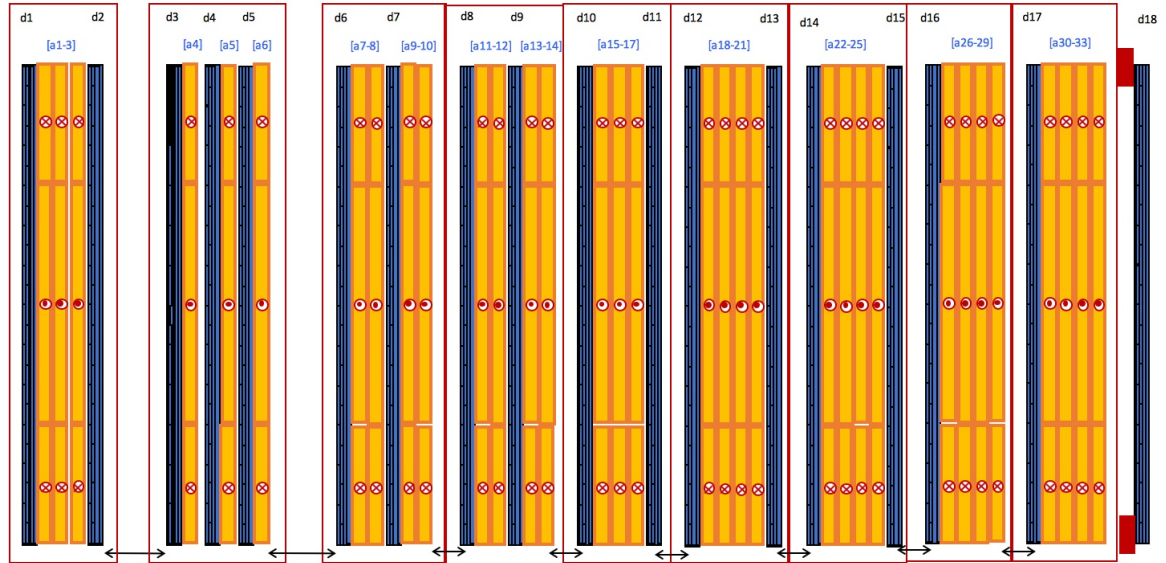


Figure 6.13: The layout of the MIND for the commissioning neutrino run.

Event Selection

1. Fiducial Volume (FV) is defined as the central region of first three iron modules (FV cut)
2. No hit in the first module (Veto for muons from outside)
3. More than 1 hit in from 2nd to 4th scintillator modules
(Compare with Simulation)

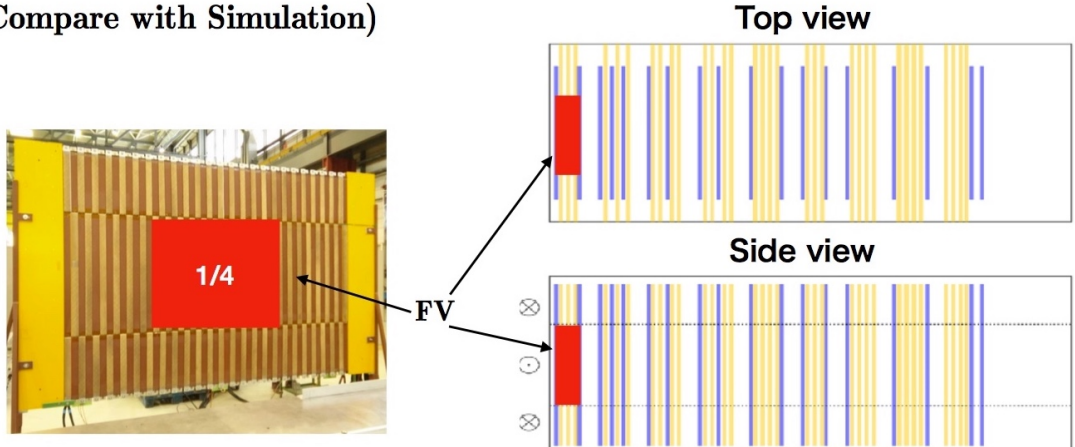


Figure 6.14: Details of the fiducial volume for the neutrino events to compare simulations with data.

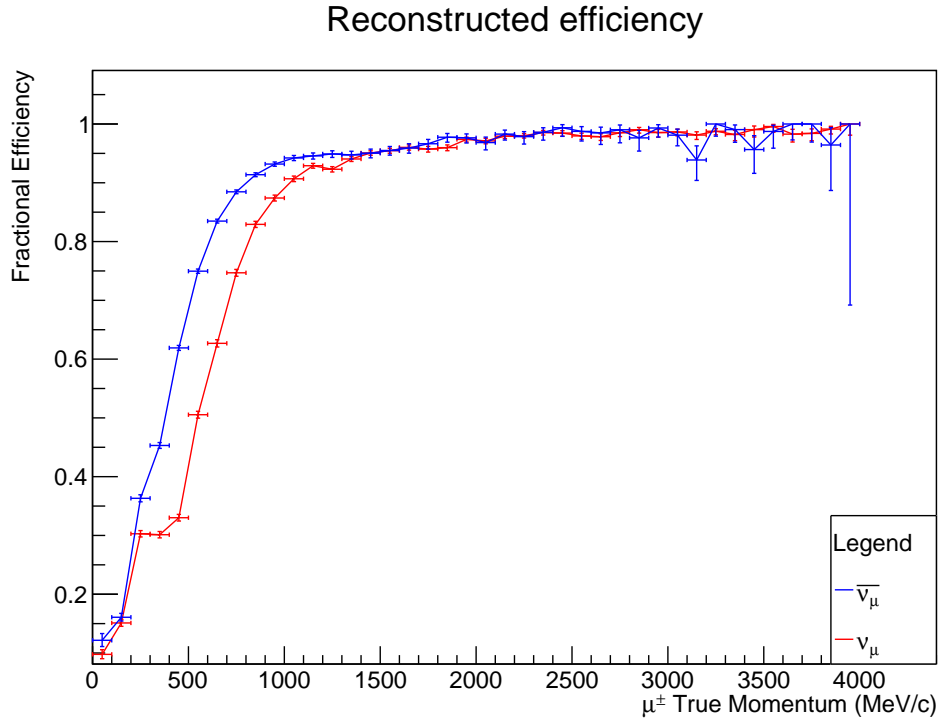


Figure 6.15: The efficiency plot of how well the algorithm can reconstruct neutrino tracks vs muon momenta for simulated tracks interacting in the Iron.

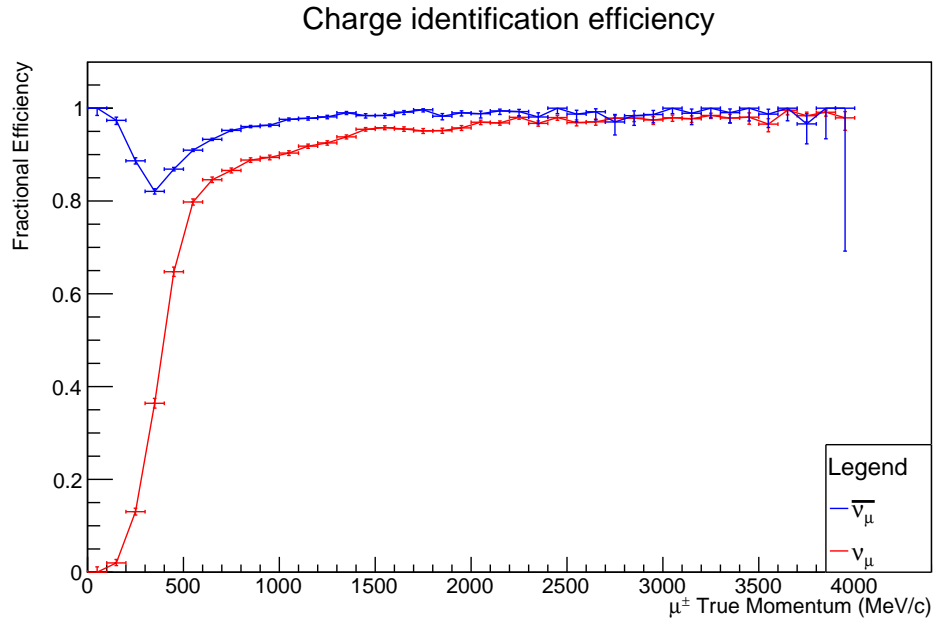


Figure 6.16: The efficiency plot of how well the algorithm can reconstruct muon charge vs muon momenta for tracks fitted in the algorithm.

6.1.2.1 Simulations vs data

Show same as the idea for nuFact, explain in detail what was done. Show the data, neutrino energy reconstruction.

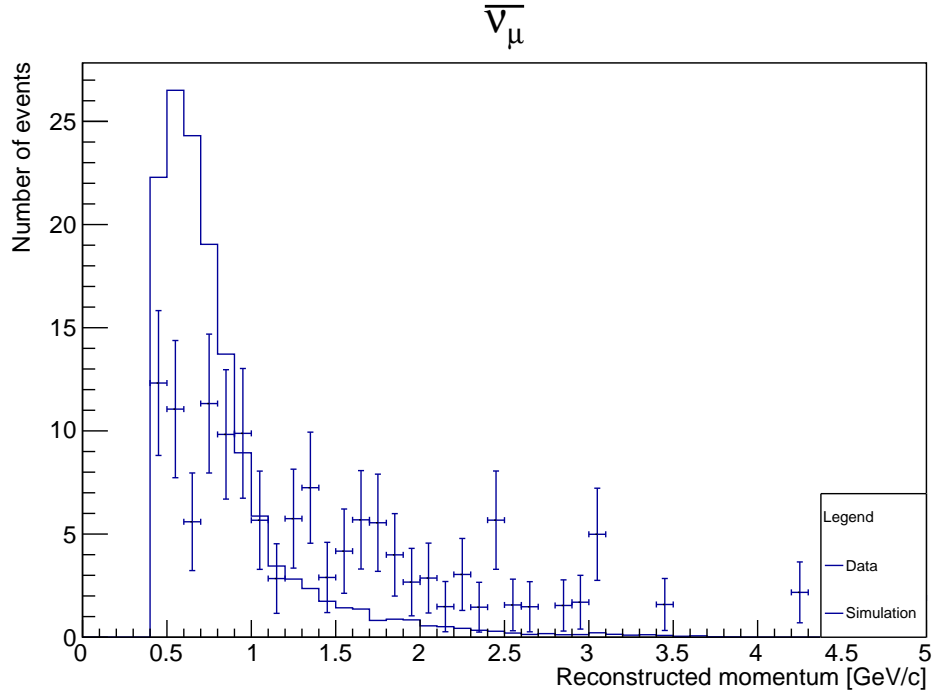


Figure 6.17: Energy spectrum of the reconstructed events with simulation in contour and data as error bars for $\bar{\nu}_\mu$ events.

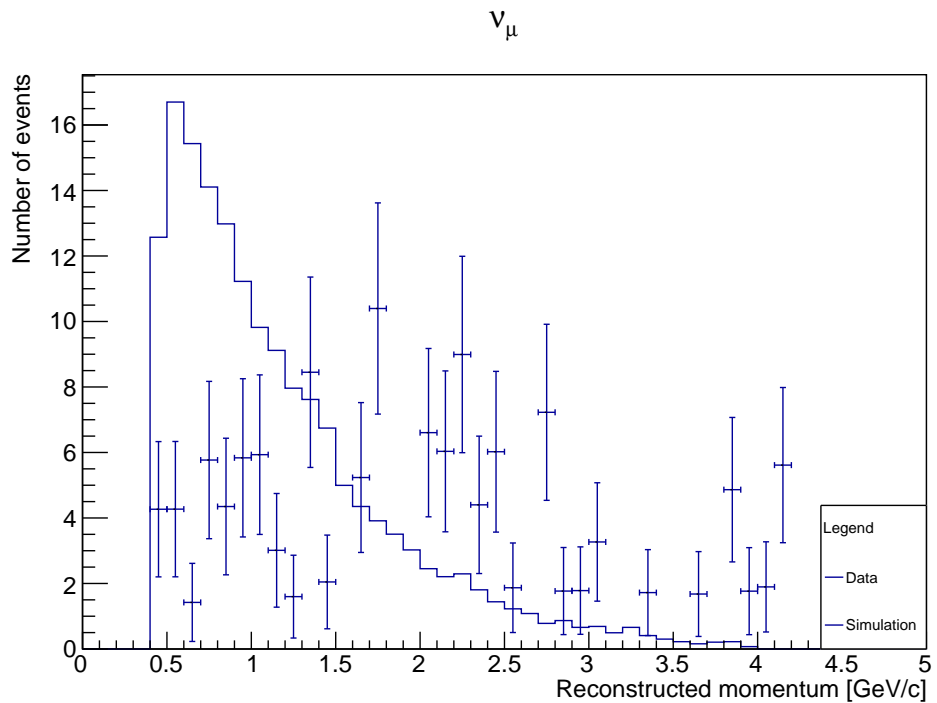


Figure 6.18: Energy spectrum of the reconstructed events with simulation in contour and data as error bars for ν_μ events.

6.2 Future studies

6.2.1 Neutrino interactions in WAGASCI + Baby MIND

Using WAGASCI as a CCQE identification,

6.2.1.1 Interactions in the full WAGASCI

Discuss future data taking, interactions everywhere etc etc.

6.3 Summary

Something here.

Chapter 7

Conclusions and Outlook

7.1 Baby MIND

7.2 WAGASCI

7.3 Software

7.4 Machine learning in physics

7.5 Neutrino physics

Bibliography

- [1] Wolfgang Pauly. May 2016. URL: https://www.library.ethz.ch/exhibit/pauli/neutrino_e.html (cit. on p. 1).
- [2] Fred L. Wilson. “Fermi Theory of Beta Decay”. In: *American Journal of Physics* 36.12 (1968), pp. 1150–1160. DOI: <http://dx.doi.org/10.1119/1.1974382>. URL: <http://scitation.aip.org/content/aapt/journal/ajp/36/12/10.1119/1.1974382> (cit. on p. 1).
- [3] F. A. Scott. “Energy Spectrum of the Beta-Rays of Radium E”. In: *Phys. Rev.* 48 (5 1935), pp. 391–395. DOI: [10.1103/PhysRev.48.391](https://doi.org/10.1103/PhysRev.48.391). URL: <https://link.aps.org/doi/10.1103/PhysRev.48.391> (cit. on p. 2).
- [4] FREDERICK REINES and CLYDE L. COWAN. “The Neutrino”. In: *Nature* 178.4531 (Sept. 1956), pp. 446–449. URL: <http://dx.doi.org/10.1038/178446a0> (cit. on pp. 1, 22).
- [5] G. Danby et al. “Observation of High-Energy Neutrino Reactions and the Existence of Two Kinds of Neutrinos”. In: *Phys. Rev. Lett.* 9 (1 1962), pp. 36–44. DOI: [10.1103/PhysRevLett.9.36](https://doi.org/10.1103/PhysRevLett.9.36). URL: <https://link.aps.org/doi/10.1103/PhysRevLett.9.36> (cit. on p. 2).
- [6] M. L. Perl et al. “Evidence for Anomalous Lepton Production in $e^+ - e^-$ Annihilation”. In: *Phys. Rev. Lett.* 35 (22 1975), pp. 1489–1492. DOI: [10.1103/PhysRevLett.35.1489](https://doi.org/10.1103/PhysRevLett.35.1489). URL: <https://link.aps.org/doi/10.1103/PhysRevLett.35.1489> (cit. on p. 2).
- [7] K. Kodama et al. “Observation of tau neutrino interactions”. In: *Phys. Lett.* B504 (2001), pp. 218–224. DOI: [10.1016/S0370-2693\(01\)00307-0](https://doi.org/10.1016/S0370-2693(01)00307-0). arXiv: [hep-ex/0012035 \[hep-ex\]](https://arxiv.org/abs/hep-ex/0012035) (cit. on p. 2).
- [8] M. Goldhaber, L. Grodzins, and A. W. Sunyar. “Helicity of Neutrinos”. In: *Phys. Rev.* 109 (3 1958), pp. 1015–1017. DOI: [10.1103/PhysRev.109.1015](https://doi.org/10.1103/PhysRev.109.1015). URL: <https://link.aps.org/doi/10.1103/PhysRev.109.1015> (cit. on p. 5).

- [9] “The standard model and the neutrino”. In: *Massive Neutrinos in Physics and Astrophysics*. 3rd. WORLD SCIENTIFIC, 2012, pp. 21–41. DOI: 10.1142/9789812562203_0002. eprint: http://www.worldscientific.com/doi/pdf/10.1142/9789812562203_0002. URL: http://www.worldscientific.com/doi/abs/10.1142/9789812562203_0002 (cit. on pp. 5, 15, 16).
- [10] F. Englert and R. Brout. “Broken Symmetry and the Mass of Gauge Vector Mesons”. In: *Phys. Rev. Lett.* 13 (9 1964), pp. 321–323. DOI: 10.1103/PhysRevLett.13.321. URL: <http://link.aps.org/doi/10.1103/PhysRevLett.13.321> (cit. on pp. 5, 6, 8).
- [11] Jeffrey Goldstone, Abdus Salam, and Steven Weinberg. “Broken Symmetries”. In: *Phys. Rev.* 127 (3 1962), pp. 965–970. DOI: 10.1103/PhysRev.127.965. URL: <https://link.aps.org/doi/10.1103/PhysRev.127.965> (cit. on p. 6).
- [12] K. A. Olive et al. “Review of Particle Physics”. In: *Chin. Phys. C*38 (2014), p. 090001. DOI: 10.1088/1674-1137/38/9/090001 (cit. on pp. 8, 12, 15, 17, 74, 101).
- [13] W. E. Burcham and M. Jobes. *Nuclear and Particle Physics*. Second. Pearson education, 1995 (cit. on p. 8).
- [14] D. Griffiths. *Introduction to Elementary Particles*. Physics textbook. Wiley, 2008. ISBN: 9783527406012. URL: <https://books.google.ch/books?id=w9Dz56myXm8C> (cit. on p. 8).
- [15] Wikipedia. 2017. URL: http://en.wikipedia.org/wiki/File:Standard_Model_of_Elementary_Particles.svg (cit. on p. 9).
- [16] Michael E Peskin and Daniel V Schroeder. *An Introduction to Quantum Field Theory; 1995 ed.* Boulder, CO: Westview, 1995. URL: <https://cds.cern.ch/record/257493> (cit. on pp. 9, 10, 18).
- [17] Sven-Patrik Hallsjö. “Search for Dark Matter in the Upgraded High Luminosity LHC at CERN : Sensitivity of ATLAS phase II upgrade to dark matter production”. MA thesis. Linkping University, Department of Physics, Chemistry and Biology, 2014, p. 79 (cit. on p. 9).
- [18] C. D. Froggatt et al. *Neutrinos in particle physics, astrophysics and cosmology*. Vol. Scottish graduate series. CRC Press, 2009 (cit. on pp. 11, 12).
- [19] J.N. Bahcall. *Neutrino Astrophysics*. Cambridge University Press, 1989. ISBN: 978052137975. URL: <https://books.google.co.uk/books?id=8GIP7uNMhlC> (cit. on pp. 13, 14).

- [20] R. Jr. Davis, J. C. Evans, and B. T. Cleveland. *Solar Neutrino Problem*. 1978. URL: <http://www.osti.gov/accomplishments/documents/fullText/ACC0068.pdf> (cit. on pp. 13, 28).
- [21] Nick Jelley, Arthur B. McDonald, and R.G. Hamish Robertson. “The Sudbury Neutrino Observatory”. In: *Annual Review of Nuclear and Particle Science* 59.1 (2009), pp. 431–465. DOI: [10.1146/annurev.nucl.55.090704.151550](https://doi.org/10.1146/annurev.nucl.55.090704.151550). eprint: <http://dx.doi.org/10.1146/annurev.nucl.55.090704.151550>. URL: <http://dx.doi.org/10.1146/annurev.nucl.55.090704.151550> (cit. on pp. 14, 28, 29).
- [22] K. S. Hirata et al. “Observation in the Kamiokande-II detector of the neutrino burst from supernova SN1987A”. In: *Phys. Rev. D* 38 (2 1988), pp. 448–458. DOI: [10.1103/PhysRevD.38.448](https://doi.org/10.1103/PhysRevD.38.448). URL: <https://link.aps.org/doi/10.1103/PhysRevD.38.448> (cit. on p. 14).
- [23] Y. Fukuda et al. “Evidence for Oscillation of Atmospheric Neutrinos”. In: *Phys. Rev. Lett.* 81 (8 1998), pp. 1562–1567. DOI: [10.1103/PhysRevLett.81.1562](https://doi.org/10.1103/PhysRevLett.81.1562). URL: <https://link.aps.org/doi/10.1103/PhysRevLett.81.1562> (cit. on pp. 14, 26, 27).
- [24] B. Pontecorvo. “Neutrino Experiments and the Problem of Conservation of Leptonic Charge”. In: *Soviet Journal of Experimental and Theoretical Physics* 26 (May 1968), p. 984 (cit. on pp. 14, 15).
- [25] Ziro Maki, Masami Nakagawa, and Shoichi Sakata. “Remarks on the Unified Model of Elementary Particles”. In: *Progress of Theoretical Physics* 28.5 (1962), pp. 870–880. DOI: [10.1143/PTP.28.870](https://doi.org/10.1143/PTP.28.870). eprint: <http://ptp.oxfordjournals.org/content/28/5/870.full.pdf+html>. URL: <http://ptp.oxfordjournals.org/content/28/5/870.abstract> (cit. on p. 15).
- [26] K. Abe et al. “Combined Analysis of Neutrino and Antineutrino Oscillations at T2K”. In: *Phys. Rev. Lett.* 118.15 (2017), p. 151801. DOI: [10.1103/PhysRevLett.118.151801](https://doi.org/10.1103/PhysRevLett.118.151801). arXiv: [1701.00432 \[hep-ex\]](https://arxiv.org/abs/1701.00432) (cit. on p. 17).
- [27] Michael Victor Berry. *Principles of cosmology and gravitation*. Bristol: IOP, 1989. URL: <https://cds.cern.ch/record/206659> (cit. on p. 18).
- [28] M. Aguilar et al. “The Alpha Magnetic Spectrometer (AMS) on the International Space Station: Part I results from the test flight on the space shuttle”. In: *Physics Reports* 366.6 (2002), pp. 331 –405. ISSN: 0370-1573. DOI: [http://dx.doi.org/10.1016/S0370-1573\(02\)00013-3](https://doi.org/10.1016/S0370-1573(02)00013-3). URL: <http://www.sciencedirect.com/science/article/pii/S0370157302000133> (cit. on p. 18).

- [29] L. Accardo et al. “High Statistics Measurement of the Positron Fraction in Primary Cosmic Rays of 0.5~500 GeV with the Alpha Magnetic Spectrometer on the International Space Station”. In: *Phys. Rev. Lett.* 113 (12 2014), p. 121101. DOI: 10.1103/PhysRevLett.113.121101. URL: <http://link.aps.org/doi/10.1103/PhysRevLett.113.121101> (cit. on p. 18).
- [30] Laurent Canetti, Marco Drewes, and Mikhail Shaposhnikov. “Matter and Antimatter in the Universe”. In: *New J. Phys.* 14 (2012), p. 095012. DOI: 10.1088/1367-2630/14/9/095012. arXiv: 1204.4186 [hep-ph] (cit. on p. 18).
- [31] M. C. Gonzalez-Garcia et al. “Global fit to three neutrino mixing: critical look at present precision”. In: *JHEP* 12 (2012), p. 123. DOI: 10.1007/JHEP12(2012)123. arXiv: 1209.3023 [hep-ph] (cit. on p. 18).
- [32] Andrei D Sakharov. “Violation of CP invariance, C asymmetry, and baryon asymmetry of the universe”. In: *Soviet Physics Uspekhi* 34.5 (1991), p. 392. URL: <http://stacks.iop.org/0038-5670/34/i=5/a=A08> (cit. on p. 18).
- [33] “Contents”. In: *Neutrinos in Particle Physics, Astrophysics and Cosmology*. CRC Press, 2008. ISBN: 978-1-4200-8239-5. DOI: doi:10.1201/9781420082401.fmatt. URL: <http://dx.doi.org/10.1201/9781420082401.fmatt> (cit. on p. 19).
- [34] Scott Dodelson and Lawrence M. Widrow. “Sterile-neutrinos as dark matter”. In: *Phys. Rev. Lett.* 72 (1994), pp. 17–20. DOI: 10.1103/PhysRevLett.72.17. arXiv: hep-ph/9303287 [hep-ph] (cit. on p. 20).
- [35] Gerard Jungman, Marc Kamionkowski, and Kim Griest. “Supersymmetric dark matter”. In: *Phys. Rept.* 267 (1996), pp. 195–373. DOI: 10.1016/0370-1573(95)00058-5. arXiv: hep-ph/9506380 [hep-ph] (cit. on p. 20).
- [36] J. D. Vergados, H. Ejiri, and F. Simkovic. “Theory of Neutrinoless Double Beta Decay”. In: *Rept. Prog. Phys.* 75 (2012), p. 106301. DOI: 10.1088/0034-4885/75/10/106301. arXiv: 1205.0649 [hep-ph] (cit. on p. 21).
- [37] V. S. Narasimham. “Perspectives of Experimental Neutrino Physics in India”. In: *Proceedings, Neutrino 2001 Meeting: Chennai, India, February, 2001*. Vol. A70. 1. 2004, pp. 11–25. URL: <http://www.ino.tifr.res.in/ino//OpenReports/Insa/naras.pdf> (cit. on p. 24).
- [38] G. Battistoni et al. “The NUSEX detector”. In: *Nuclear Instruments and Methods in Physics Research Section A: Accelerators, Spectrometers, Detectors and Associated Equipment* 245.2 (1986), pp. 277 –290. ISSN: 0168-9002. DOI: [https://doi.org/10.1016/0168-9002\(86\)91261-1](https://doi.org/10.1016/0168-9002(86)91261-1). URL: <http://www>.

sciencedirect.com/science/article/pii/0168900286912611 (cit. on p. 24).

- [39] S. Ragazzi et al. “A study of the atmospheric neutrino flux in NUSEX”. In: *Tests of fundamental laws in physics. Proceedings, 9th Moriond Workshop, 24th Rencontres de Moriond, Les Arcs, France, January 21-28, 1989.* 1989, pp. 237–241. URL: http://inspirehep.net/record/292419/files/C89-01-21_237-241.pdf (cit. on pp. 24, 25).
- [40] K. Arisaka et al. “KAMIOKA Nucleon Decay Experiments; status and performance”. In: *AIP Conf. Proc.* 114 (1984), pp. 54–76. DOI: 10.1063/1.34507 (cit. on p. 25).
- [41] M. Koshiba. “KAMIOKA NUCLEON DECAY EXPERIMENT”. In: *Nuovo Cim.* C9 (1986), pp. 141–158. DOI: 10.1007/BF02514837 (cit. on p. 26).
- [42] R. Clark. “The atmospheric neutrino muon-like fraction above 1-GeV”. In: *AIP Conf. Proc.* 412.1 (1997), pp. 958–961. DOI: 10.1063/1.54393 (cit. on p. 26).
- [43] K. Abe et al. “Search for Differences in Oscillation Parameters for Atmospheric Neutrinos and Antineutrinos at Super-Kamiokande”. In: *Phys. Rev. Lett.* 107 (24 2011), p. 241801. DOI: 10.1103/PhysRevLett.107.241801. URL: <http://link.aps.org/doi/10.1103/PhysRevLett.107.241801> (cit. on p. 26).
- [44] MACRO Collaboration et al. “Measurement of the atmospheric neutrino-induced upgoing muon flux using MACRO”. In: *Physics Letters B* 434 (Aug. 1998), pp. 451–457. DOI: 10.1016/S0370-2693(98)00885-5. eprint: [hep-ex/9807005](https://arxiv.org/abs/hep-ex/9807005) (cit. on p. 27).
- [45] M. Ambrosio et al. “The MACRO detector at Gran Sasso”. In: *Nucl. Instrum. Meth.* A486 (2002), pp. 663–707. DOI: 10.1016/S0168-9002(01)02169-6 (cit. on p. 28).
- [46] J. P. Cravens et al. “Solar neutrino measurements in Super-Kamiokande-II”. In: *prd* 78.3, 032002 (Aug. 2008), p. 032002. DOI: 10.1103/PhysRevD.78.032002. arXiv: 0803.4312 [hep-ex] (cit. on p. 28).
- [47] H. M. O’Keeffe, E. O’Sullivan, and M. C. Chen. “Scintillation decay time and pulse shape discrimination in oxygenated and deoxygenated solutions of linear alkylbenzene for the SNO+ experiment”. In: *Nucl. Instrum. Meth.* A640 (2011), pp. 119–122. DOI: 10.1016/j.nima.2011.03.027. arXiv: 1102.0797 [physics.ins-det] (cit. on p. 29).

- [48] G Ranucci et al. “Overview and accomplishments of the Borexino experiment”. In: *Journal of Physics: Conference Series* 675.1 (2016), p. 012036. URL: <http://stacks.iop.org/1742-6596/675/i=1/a=012036> (cit. on p. 30).
- [49] F. Dydak et al. “A search for oscillations in the m₂ range 0.390 eV²”. In: *Physics Letters B* 134.3 (1984), pp. 281 –286. ISSN: 0370-2693. DOI: [http://dx.doi.org/10.1016/0370-2693\(84\)90688-9](http://dx.doi.org/10.1016/0370-2693(84)90688-9). URL: <http://www.sciencedirect.com/science/article/pii/0370269384906889> (cit. on pp. 31, 46).
- [50] J. Dorenbosch et al. “Calibration of the charm fine-grained calorimeter”. In: *Nuclear Instruments and Methods in Physics Research Section A: Accelerators, Spectrometers, Detectors and Associated Equipment* 253.2 (1987), pp. 203 –221. ISSN: 0168-9002. DOI: [https://doi.org/10.1016/0168-9002\(87\)90708-X](https://doi.org/10.1016/0168-9002(87)90708-X). URL: <http://www.sciencedirect.com/science/article/pii/016890028790708X> (cit. on p. 32).
- [51] P. Spentzouris. “Precision electroweak results from neutrino nucleon scattering at CCFR/NuTeV”. In: *Nucl. Phys. Proc. Suppl.* 66 (1998). [,112(1998)], pp. 112–115. DOI: [10.1016/S0920-5632\(98\)00022-X](https://doi.org/10.1016/S0920-5632(98)00022-X) (cit. on p. 32).
- [52] J. Altegoer et al. “The NOMAD experiment at the CERN SPS”. In: *Nuclear Instruments and Methods in Physics Research Section A: Accelerators, Spectrometers, Detectors and Associated Equipment* 404.1 (1998), pp. 96 –128. ISSN: 0168-9002. DOI: [https://doi.org/10.1016/S0168-9002\(97\)01079-6](https://doi.org/10.1016/S0168-9002(97)01079-6). URL: <http://www.sciencedirect.com/science/article/pii/S0168900297010796> (cit. on p. 32).
- [53] F Vannucci. “The NOMAD Experiment at CERN”. In: *Adv. High Energy Phys.* 2014 (2014), p. 129694. URL: <http://cds.cern.ch/record/1666456> (cit. on p. 32).
- [54] M. H. Ahn et al. “Measurement of Neutrino Oscillation by the K2K Experiment”. In: *Phys. Rev. D* 74 (2006), p. 072003. DOI: [10.1103/PhysRevD.74.072003](https://doi.org/10.1103/PhysRevD.74.072003). arXiv: [hep-ex/0606032](https://arxiv.org/abs/hep-ex/0606032) [hep-ex] (cit. on p. 33).
- [55] J. Zalipska. “Neutrino oscillation in the K2K experiment”. In: *Acta Phys. Polon.* B37 (2006), pp. 1935–1945 (cit. on p. 33).
- [56] A. Habig and E. W. Grashorn. “The MINOS detectors”. In: *29th International Cosmic Ray Conference (ICRC 2005) Pune, India, August 3-11, 2005*. [9,319(2005)]. 2005, p. 319. arXiv: [hep-ex/0507018](https://arxiv.org/abs/hep-ex/0507018) [hep-ex]. URL: http://lss.fnal.gov/cgi-bin/find_paper.pl?conf-05-264-E (cit. on pp. 33, 42, 46).

- [57] P. Adamson et al. “The NuMI Neutrino Beam”. In: *Nucl. Instrum. Meth.* A806 (2016), pp. 279–306. DOI: 10.1016/j.nima.2015.08.063. arXiv: 1507.06690 [physics.acc-ph] (cit. on p. 34).
- [58] P. Adamson et al. “First measurement of electron neutrino appearance in NOvA”. In: *Phys. Rev. Lett.* 116.15 (2016), p. 151806. DOI: 10.1103/PhysRevLett.116.151806. arXiv: 1601.05022 [hep-ex] (cit. on p. 34).
- [59] L. Aliaga et al. “Design, Calibration, and Performance of the MINERvA Detector”. In: *Nucl. Instrum. Meth.* A743 (2014), pp. 130–159. DOI: 10.1016/j.nima.2013.12.053. arXiv: 1305.5199 [physics.ins-det] (cit. on p. 34).
- [60] E. Church et al. “A proposal for an experiment to measure muon-neutrino— $\bar{\nu}$ electron-neutrino oscillations and muon-neutrino disappearance at the Fermilab Booster: BooNE”. In: (1997) (cit. on p. 34).
- [61] K. Abe et al. “Measurements of neutrino oscillation in appearance and disappearance channels by the T2K experiment with 6.6×10^{20} protons on target”. In: *Phys. Rev.* D91.7 (2015), p. 072010. DOI: 10.1103/PhysRevD.91.072010. arXiv: 1502.01550 [hep-ex] (cit. on pp. 34, 35, 42, 48, 55, 57).
- [62] L. Haegel. “The latest T2K neutrino oscillation results”. In: *2017 European Physical Society Conference on High Energy Physics (EPS-HEP 2017) Venice, Italy, July 5-12, 2017*. 2017. arXiv: 1709.04180 [hep-ex]. URL: <https://inspirehep.net/record/1623206/files/arXiv:1709.04180.pdf> (cit. on p. 36).
- [63] K. Abe et al. “Neutrino oscillation physics potential of the T2K experiment”. In: *PTEP* 2015.4 (2015), p. 043C01. DOI: 10.1093/ptep/ptv031. arXiv: 1409.7469 [hep-ex] (cit. on p. 35).
- [64] Carlo Bemporad, Giorgio Gratta, and Petr Vogel. “Reactor based neutrino oscillation experiments”. In: *Rev. Mod. Phys.* 74 (2002), p. 297. DOI: 10.1103/RevModPhys.74.297. arXiv: hep-ph/0107277 [hep-ph] (cit. on p. 37).
- [65] K. Eguchi et al. “First results from KamLAND: Evidence for reactor anti-neutrino disappearance”. In: *Phys. Rev. Lett.* 90 (2003), p. 021802. DOI: 10.1103/PhysRevLett.90.021802. arXiv: hep-ex/0212021 [hep-ex] (cit. on p. 38).
- [66] F. Ardellier et al. “Double Chooz: A Search for the neutrino mixing angle theta(13)”. In: (2006). arXiv: hep-ex/0606025 [hep-ex] (cit. on pp. 38, 39).
- [67] N. S. Bowden. “Reactor monitoring and safeguards using antineutrino detectors”. In: *J. Phys. Conf. Ser.* 136 (2008), p. 022008. DOI: 10.1088/1742-6596/136/2/022008. arXiv: 0809.2128 [nucl-ex] (cit. on p. 38).

- [68] J. I. Crespo-Anadon. “Double Chooz: Latest results”. In: *Nucl. Part. Phys. Proc.* 265–266 (2015), pp. 99–104. DOI: 10.1016/j.nuclphysbps.2015.06.025. arXiv: 1412.3698 [hep-ex] (cit. on p. 39).
- [69] Soo-Bong Kim. “Results from Reno”. In: *PoS NEUTEL2017* (2018), p. 007 (cit. on p. 39).
- [70] Xinheng Guo et al. “A Precision measurement of the neutrino mixing angle θ_{13} using reactor antineutrinos at Daya-Bay”. In: (2007). arXiv: hep-ex / 0701029 [hep-ex] (cit. on p. 40).
- [71] Vit Vorobel. “Latest results from Daya Bay”. In: *J. Phys. Conf. Ser.* 873.1 (2017), p. 012031. DOI: 10.1088/1742-6596/873/1/012031 (cit. on p. 40).
- [72] C. Jollet. “The JUNO experiment”. In: *Nuovo Cim.* C39.4 (2017), p. 318. DOI: 10.1393/ncc/i2016-16318-6 (cit. on p. 41).
- [73] R. Acciarri et al. “Long-Baseline Neutrino Facility (LBNF) and Deep Underground Neutrino Experiment (DUNE) Conceptual Design Report Volume 1: The LBNF and DUNE Projects”. In: (2016). arXiv: 1601.05471 [physics.ins-det] (cit. on p. 42).
- [74] R. Acciarri et al. “Long-Baseline Neutrino Facility (LBNF) and Deep Underground Neutrino Experiment (DUNE)”. In: (2015). arXiv: 1512.06148 [physics.ins-det] (cit. on p. 42).
- [75] K. Abe et al. “Letter of Intent: The Hyper-Kamiokande Experiment — Detector Design and Physics Potential —”. In: (2011). arXiv: 1109.3262 [hep-ex] (cit. on pp. 42, 43, 55).
- [76] F. J. P. Soler. “Neutrino factories”. In: *AIP Conference Proceedings* 1666, 130002 (2015). DOI: http://dx.doi.org/10.1063/1.4915580. URL: http://scitation.aip.org/content/aip/proceeding/aipcp/10.1063/1.4915580 (cit. on pp. 43, 44, 45).
- [77] P Gruber et al. “The Study of a European Neutrino Factory Complex”. In: CERN-PS-2002-080-PP. CERN-NEUTRINO-FACTORY-NOTE-122. CERN-NUFACT-NOTE-122 (2002), 73 p. URL: http://cds.cern.ch/record/610249 (cit. on pp. 43, 44, 47).
- [78] M. Dracos and E. n. S. project. “The ESS neutrino facility for CP violation discovery”. In: *Proceedings of the 38th International Conference on High Energy Physics (ICHEP2016). 3-10 August 2016. Chicago, USA. Online at ;A href=“http://pos.sissa.it/cgi-bin/reader/conf.cgi?confid=282”;http://pos.sissa.it/cgi-bin/reader/conf.cgi?confid=282;A; id.460.* 2016, p. 460 (cit. on p. 44).

- [79] S. Geer. “Muon colliders and neutrino factories”. In: *Proceedings, 25th International Linear Accelerator Conference, LINAC2010: Tsukuba, Japan, September 12-17, 2010.* 2011, FR202. arXiv: 1202.2140 [physics.acc-ph]. URL: http://lss.fnal.gov/cgi-bin/find_paper.pl?conf-10-370 (cit. on p. 44).
- [80] D. Adey et al. “Overview of the Neutrinos from Stored Muons Facility - nuSTORM”. In: *JINST* 12.07 (2017), P07020. DOI: 10.1088/1748-0221/12/07/P07020 (cit. on p. 45).
- [81] S. Choubey et al. “International Design Study for the Neutrino Factory, Interim Design Report”. In: (2011). arXiv: 1112.2853 [hep-ex] (cit. on p. 45).
- [82] The ISS Detector Working Group et al. “International Scoping Study (ISS) for a future neutrino factory and Super-Beam facility. Detectors and flux instrumentation for future neutrino facilities”. In: *Journal of Instrumentation* 4.05 (2009), T05001. URL: <http://stacks.iop.org/1748-0221/4/i=05/a=T05001> (cit. on p. 46).
- [83] A. Bross et al. “Toroidal magnetized iron neutrino detector for a neutrino factory”. In: *Phys. Rev. ST Accel. Beams* 16.8 (2013), p. 081002. DOI: 10.1103/PhysRevSTAB.16.081002. arXiv: 1306.5327 [physics.ins-det] (cit. on pp. 46, 62).
- [84] E Noah. *Proposal for characterization of muon spectrometers for neutrino beam lines with the Baby MIND*. Tech. rep. CERN-SPSC-2015-031. SPSC-P-353. Geneva: CERN, 2015. URL: <http://cds.cern.ch/record/2057587> (cit. on p. 47).
- [85] May 2016. URL: <https://cenf-baby-mind.web.cern.ch> (cit. on p. 47).
- [86] S. Agostinelli et al. “Geant4a simulation toolkit”. In: *Nuclear Instruments and Methods in Physics Research Section A: Accelerators, Spectrometers, Detectors and Associated Equipment* 506.3 (2003), pp. 250 –303. ISSN: 0168-9002. DOI: [http://dx.doi.org/10.1016/S0168-9002\(03\)01368-8](http://dx.doi.org/10.1016/S0168-9002(03)01368-8). URL: <http://www.sciencedirect.com/science/article/pii/S0168900203013688> (cit. on pp. 47, 62).
- [87] G. Rolando et al. “New and Optimized Magnetization Scheme for the Baby Magnetized Iron Neutrino Detector at J-PARC”. In: *IEEE Transactions on Magnetics* 53.5 (2017), pp. 1–6. ISSN: 0018-9464. DOI: 10.1109/TMAG.2017.2664053 (cit. on p. 49).
- [88] M. Antonova et al. “Baby MIND Experiment Construction Status”. In: *Proceedings, Prospects in Neutrino Physics (NuPhys2016): London, UK, December 12-14, 2016.* 2017. arXiv: 1704.08917 [physics.ins-det]. URL: <https://cenf-baby-mind.web.cern.ch>

- inspirehep.net/record/1597343/files/arXiv:1704.08917.pdf (cit. on p. 49).
- [89] Stphane Callier et al. “EASIROC, an Easy & Versatile ReadOut Device for SiPM”. In: *Physics Procedia* 37 (2012). Proceedings of the 2nd International Conference on Technology and Instrumentation in Particle Physics (TIPP 2011), pp. 1569 –1576. ISSN: 1875-3892. DOI: <https://doi.org/10.1016/j.phpro.2012.02.486>. URL: <http://www.sciencedirect.com/science/article/pii/S1875389212018688> (cit. on p. 51).
- [90] M. Antonova et al. “Synchronization of the distributed readout frontend electronics of the Baby MIND detector”. In: *2017 XXVI International Scientific Conference Electronics (ET)*. 2017, pp. 1–4. DOI: [10.1109/ET.2017.8124369](https://doi.org/10.1109/ET.2017.8124369) (cit. on pp. 53, 54, 84).
- [91] T Ovsiannikova et al. “The new experiment WAGASCI for water to hydrocarbon neutrino cross section measurement using the J-PARC beam”. In: *Journal of Physics: Conference Series* 675.1 (2016), p. 012030. URL: <http://stacks.iop.org/1742-6596/675/i=1/a=012030> (cit. on pp. 55, 56).
- [92] K. Abe et al. “Measurements of the T2K neutrino beam properties using the INGRID on-axis near detector”. In: *Nuclear Instruments and Methods in Physics Research A* 694 (Dec. 2012), pp. 211–223. DOI: [10.1016/j.nima.2012.03.023](https://doi.org/10.1016/j.nima.2012.03.023). arXiv: [1111.3119 \[physics.ins-det\]](https://arxiv.org/abs/1111.3119) (cit. on p. 57).
- [93] A.Laing. “Optimisation of detectors for the golden channel at a neutrino factory”. PhD thesis. University of Glasgow, 2010. URL: <http://theses.gla.ac.uk/id/eprint/2216> (cit. on p. 62).
- [94] M. Antonova et al. “Baby MIND: A Magnetised Spectrometer for the WAGASCI Experiment”. In: *Proceedings, Prospects in Neutrino Physics (NuPhys2016): London, UK, December 12-14, 2016*. 2017. arXiv: [1704.08079 \[physics.ins-det\]](https://arxiv.org/abs/1704.08079). URL: <http://lss.fnal.gov/archive/2017/conf/fermilab-conf-17-270-apc.pdf> (cit. on p. 62).
- [95] C. Andreopoulos et al. “The GENIE Neutrino Monte Carlo Generator”. In: *Nucl. Instrum. Meth.* A614 (2010), pp. 87–104. DOI: [10.1016/j.nima.2009.12.009](https://doi.org/10.1016/j.nima.2009.12.009). arXiv: [0905.2517 \[hep-ph\]](https://arxiv.org/abs/0905.2517) (cit. on p. 62).
- [96] A. Cervera-Villanueva, J. J. Gómez-Cadenas, and J. A. Hernando. “RecPack, a general reconstruction toolkit”. In: *Astroparticle, Particle, Space Physics and Detectors For Physics Applications - Proceedings of the 13th ICATPP Conference. Edited by Giani Simone et al. Published by World Scientific Publishing Co. Pte. Ltd., 2012*.

- ISBN #9789814405072, pp. 954-960.* Ed. by S. Giani and et al. Aug. 2012, pp. 954–960. DOI: 10.1142/9789814405072_0146 (cit. on pp. 62, 69).
- [97] Rene Brun and Fons Rademakers. “ROOT - An Object Oriented Data Analysis Framework”. In: *Sep. 1996, Nucl. Inst. & Meth. in Phys. Res. A 389 (1997) 81-86.* See also <http://root.cern.ch/>. (Cit. on p. 62).
- [98] R. Chytracek et al. “Geometry Description Markup Language for Physics Simulation and Analysis Applications”. In: *IEEE Transactions on Nuclear Science 53.5* (2006), pp. 2892–2896. ISSN: 0018-9499. DOI: 10.1109/TNS.2006.881062 (cit. on p. 65).
- [99] A. Hoecker et al. “TMVA - Toolkit for Multivariate Data Analysis”. In: *ArXiv Physics e-prints* (Mar. 2007). eprint: [physics/0703039](https://arxiv.org/abs/physics/0703039) (cit. on pp. 77, 94).
- [100] J.R.R. Tolkien. *The Lord of the Rings: One Volume*. The Lord of the Rings. Houghton Mifflin Harcourt, 2012. ISBN: 9780547951942. URL: <https://books.google.co.uk/books?id=y14dILkcqm4C> (cit. on p. 78).
- [101] Johannes Rauch and Tobias Schlter. “GENFIT a Generic Track-Fitting Toolkit”. In: *Journal of Physics: Conference Series 608.1* (2015), p. 012042. URL: <http://stacks.iop.org/1742-6596/608/i=1/a=012042> (cit. on p. 78).
- [102] Alexander Radovic et al. “Machine learning at the energy and intensity frontiers of particle physics”. In: *Nature 560.7716* (2018), pp. 41–48. ISSN: 1476-4687. DOI: 10.1038/s41586-018-0361-2. URL: <https://doi.org/10.1038/s41586-018-0361-2> (cit. on pp. 80, 101).
- [103] C. Adams et al. “A Deep Neural Network for Pixel-Level Electromagnetic Particle Identification in the MicroBooNE Liquid Argon Time Projection Chamber”. In: (2018). arXiv: 1808.07269 [physics.ins-det] (cit. on pp. 80, 101).
- [104] M. Antonova et al. “Baby MIND: A Magnetised Spectrometer for the WAGASCI Experiment”. In: *PoS NuFact2017* (2018), p. 078. DOI: 10.22323/1.295.0078. arXiv: 1704.08079 [physics.ins-det] (cit. on p. 90).
- [105] Kevin Scott McFarland. “Neutrino Interactions”. In: *Neutrinos in particle physics, astrophysics and cosmology. Proceedings, 61st Scottish Universities Summer School in Physics, SUSSP61, St. Andrews, UK, August 8-23, 2006.* 2008, pp. 65–90. arXiv: 0804.3899 [hep-ex]. URL: <http://inspirehep.net/record/784224/files/arXiv:0804.3899.pdf> (cit. on p. 101).